SPH/N-BODY SIMULATIONS OF GALAXY FORMATION

Dissertation

zur

Erlangung der naturwissenschaftlichen Doktorwürde
(Dr. sc. nat.)

vorgelegt der

Mathematisch-naturwissenschaftlichen Fakultät

der

Universität Zürich

von

Tobias Kaufmann

von

Gränichen AG

Promotionskomitee:

Prof. Dr. Ben Moore (Vorsitz)
Prof. Dr. Daniel Wyler
Dr. Lucio Mayer

Zürich, 2006

Dem Zürcher Steuerzahler

Contents

Zusammenfassung **iii**

Summary **v**

1 Introduction **1**
- 1.1 The current picture of disk galaxy formation 1
- 1.2 The standard cosmological model 3
- 1.3 Numerical techniques 6
  - 1.3.1 N-body methods 6
    - 1.3.1.1 N-body models 8
  - 1.3.2 Hydrodynamics 9
    - 1.3.2.1 Smoothed Particle Hydrodynamics 10
- 1.4 From gas to stars 11
  - 1.4.1 Cooling 11
  - 1.4.2 Star formation and feedback 13

2 Angular momentum transport in SPH **15**
- 2.1 Abstract 15
- 2.2 Introduction 16
- 2.3 Initial Conditions 17
- 2.4 Results of the simulations 22
  - 2.4.1 Convergence in mass and angular momentum 22
  - 2.4.2 Torques and losses from smoothing and artificial viscosity 26
  - 2.4.3 Disk scale-lengths and bar formation 30
- 2.5 Stellar versus gaseous disk formation 31
- 2.6 Dependence on the Initial Conditions 35
  - 2.6.1 Influence of the temperature floor on the gravitational stability . . . 35
  - 2.6.2 Generating initial conditions using a merger 37
  - 2.6.3 Different Initial Angular Momentum Profiles 40
- 2.7 Summary and Discussion 41

3 Cooling flows within galactic haloes **45**
- 3.1 Abstract 45
- 3.2 Introduction 45
- 3.3 Initial Conditions and Methods 47
- 3.4 The assembly of the disk 49
  - 3.4.1 Gas infall and extra planar gas 50

3.5 Disk formation via accretion of a clumpy medium 53
  3.5.1 Formation of pressure confined clouds 53
  3.5.2 Evolution and dissolution of the clouds 64
    3.5.2.1 Kelvin-Helmholtz Instability 64
    3.5.2.2 Conduction 64
    3.5.2.3 Cooling below 10^4 K? 64
3.6 Conclusions 65

4 Tilting and warping 69
4.1 Abstract 69
4.2 Introduction 69
4.3 Numerical methods 71
  4.3.1 Initial Conditions 71
  4.3.2 Briggs diagrams 72
4.4 Smooth gas accretion 73
4.5 Intergalactic accretion flows 77
4.6 Summary and Discussion 82

5 The spin of the Milky Way 87
5.1 Abstract 87
5.2 Introduction 87
5.3 Initial Conditions 88
5.4 Stream simulations 89
5.5 Cloud simulations 90
5.6 Summary and Discussion 94

6 Concluding remarks and outlook 97

Bibliography 101

Acknowledgements 107

Curriculum Vitae 109

Research status 111

Zusammenfassung

Gegenstand der vorliegenden Doktorarbeit sind verschiedene Prozesse, die einen wesentlichen Einfluss auf die Entstehung von Scheibengalaxien haben. Die paradigmatische Basis der Arbeit bildet die Theorie der hierarchischen Galaxienentstehung.

Die Entstehung einer Galaxie ist ein komplexer, nicht-linearer Vorgang, in dem gravitative und hydrodynamische Prozesse wirken. In der vorliegenden Arbeit untersuchen wir mit Hilfe von SPH/N-Körper-Simulationen die Entstehung und Entwicklung von Scheibengalaxien in einem ΛCDM Universum, dessen Materienkomponente von kalter dunkler Materie (CDM) dominiert wird.

Üblicherweise wurde die Entstehung von Galaxien mit Hilfe kosmologischer Simulationen erforscht. Verglichen mit den beobachteten Galaxien waren die dabei entstehenden Scheiben jedoch zu klein, und die Konzentration ihres Zentrums fiel zu hoch aus. Die Reproduktion der beobachteten Scheibengalaxien durch Simulationen gilt als eine der grössten verbleibenden Herausforderungen auf dem Gebiet der CDM. Es ist dabei nicht klar, ob das Unvermögen, eine Scheibengalaxie mit der korrekten Skalenlänge zu simulieren, auf eine unzureichende numerische Auflösung zurückzuführen ist, ob ihm eine grundlegende Schwäche des ΛCDM-Modells zu Grunde liegt oder ob bei den kosmologischen Simulationen entscheidende physikalische Prozesse nicht berücksichtigt wurden. Um diese Fragen zu beantworten, haben wir die Entstehung und Entwicklung von Scheibengalaxien mit Simulationen isolierter Systeme untersucht, die eine bisher unübertroffene numerische Auflösung aufweisen und daher eine ideale Ergänzung zu kosmologischen Simulationen darstellen.

Mit kontrollierten SPH/N-Körper-Simulationen untersuchen wir die Entstehung von Scheibengalaxien, die aus sich abkühlenden, rotierenden Gasdistributionen im Innern von sphärischen oder triaxialen Halos aus dunkler Materie entstehen. Dabei zeigt sich, dass Morphologie und radiale Dichteprofile stark von der Massen- und Kraftauflösung abhängen. Wir finden eine bedeutende, numerisch begründete Abnahme des Drehimpulses für Simulationen, welche die gleiche Auflösung wie typische kosmologischen Simulationen aufweisen. Dieser Verlust ist vor allem auf künstliche hydrodynamische Drehmomente zurückzuführen, die dem heissen Gashalo Drehimpuls zuführen. Erst bei Millionen von Gasteilchen reduziert sich die Abnahme des Drehimpulses auf 10 bis 20%. Grund dafür ist dann ein physikalischer Transport von Drehimpuls aufgrund der Spiralarme und des Balken im Zentrum der Galaxie.

Die Art und Weise, wie sich das Gas während seiner spiralförmigen Bewegung zum Zentrum abkühlt, zeigt eine ähnliche Abhängigkeit von der numerischen Auflösung. Wir simulieren die Entstehung der M33 Galaxie aus der Lokalen Gruppe mit einer Massenauflösung von einigen Hundert Sonnenmassen pro Teilchen und können damit die thermische Instabilität im heissen Halo auflösen. Dies führt zur Bildung zahlreicher warmer Wolken, die durch den Druck des heissen Gashalos zusammen gehalten werden. Diese Wolken fallen dann langsam auf die Scheibe, diese nimmt aber gleichzeitig auch Gas aus

dem heissen Halo auf. Die Rotationsgeschwindigkeit der einfallenden Wolken nimmt dabei als Funktion der Höhe über der Scheibe ab – ein ähnliches Phänomen wie jenes, das bei extraplanarem Gas der Spiralgalaxie NGC 891 beobachtet wurde.

Diese beiden Befunde zeigen, dass das Unvermögen der kosmologischen Simulationen, eine Scheibengalaxie realistisch nachzubilden, mindestens teilweise auf eine zu geringe numerische Auflösung zurückzuführen ist. Die Bildung von Scheibengalaxien stellt daher für das CDM-Modell vermutlich kein grundlegendes Problem dar.

Die Einfallrichtung des Gases kann sich mit der Zeit ändern. Wir untersuchen daher, was geschieht, wenn das aufgenommene Gas einen anderen Drehimpuls aufweist als die Scheibe, die sich schon früher gebildet hat. Dazu führen wir Simulationen durch, bei denen Satellitengalaxien auf den ursprünglichen Halo einfallen. Dieser Einfall ruft S- und U-förmige und sogar einseitige "Warps" hervor - diese einseitigen Warps sind erstmals in SPH-Simulationen beobachtet worden. Interessanterweise ruft ein gleich schwerer Satellit, der nur aus dunkler Materie besteht, keinen einseitigen Warps hervor. Dunkle Satelliten können daher nicht die Hauptursache für einseitige Warps sein. Solche Warps werden aber relativ häufig beobachtet.

Derzeit fällt die Grosse Magellansche Wolke (LMC) auf unsere Milchstrasse ein. Der LMC wird dabei wegen des Staudrucks Gas entzogen, während sie sich spiralförmig auf die Milchstrasse zu bewegt. Dieses Gas bildet den Magellanschen Strom hinter der LMC. Der Strom wird durch den heissen Gashalo, der die Milchstrasse umgibt, abgelenkt. Die Ablenkung hängt davon ab, wie gross der Spin des Gashalos ist. Wir führen für diese Untersuchung eine Serie von Simulationen mit Halos durch, die verschiedene Spins aufweisen. Wir zeigen dabei, dass der Spin des heissen Halos der Milchstrasse maximal bei 0.05 liegen kann. Das weist darauf hin, dass die Milchstrasse eine Galaxie mit einem durchschnittlichen Spin ist.

Summary

This thesis presents a study on a variety of mechanisms governing the formation of disk galaxies within the current paradigm of hierarchical galaxy formation. Galaxy formation is a complex, non-linear problem including gravitational and hydro-dynamical processes. We examine with N-Body/Smoothed Particles Hydrodynamics (SPH) simulations the formation and evolution of disk galaxies within an ΛCDM universe filled with cold dark matter (CDM). Conventionally, galaxy formation is followed using cosmological simulations, however, up to now, those simulations produce disks that were found to be too small and too centrally concentrated compared to those of observed disk galaxies. Reproducing these galaxies is one of the biggest remaining challenges for the CDM paradigm. It is not clear if the inability to simulate a pure disk galaxy with the correct scale length is due to a fundamental flaw in the CDM model, or due to missing ingredients in the cosmological simulations, or due to numerical effects such as resolution. To address these questions we have investigated the formation and evolution of disk galaxies by performing simulations of isolated systems, reaching currently unmatched resolution and complementing studies of disk formation within cosmological simulations.

We use controlled N-Body/SPH simulations of disk galaxy formation by cooling a rotating gaseous mass distribution inside equilibrium cuspy spherical and triaxial dark matter haloes. We find, that the disk morphology and radial profiles depend sensitively on force and mass resolution. We see significant numerical angular momentum loss at resolutions used in current cosmological simulations, primarily due to spurious hydrodynamical torques transferring angular momentum to the hot phase. With millions of gas particles we are left with physical angular momentum transport due to spiral patterns and bars and a residual loss of 10–20%.

The cooling flow of gas within galactic haloes seems to depend on resolution in a similar fashion: We simulate the formation of the Local Group spiral galaxy M33 resolving mass scales of several hundreds solar masses in the gas component and follow the thermal instabilities in the hot gas halo. This results in the formation of numerous warm clouds that are pressure confined by the hot ambient halo gas. The clouds fall slowly onto the disk, but the disk is also accreting gas directly from the halo. The rotational velocity of the infalling cold gas decreases as a function of height above the disk, closely resembling that of the extra-planar gas recently observed around the spiral galaxy NGC 891.

Those two findings reveal that the problem of simulating realistic galactic disks in cosmological simulations is a least partially connected to effects due to insufficient numerical resolution and might not be a fundamental problem for CDM.

The direction of gas-infall may change with time. We then investigate the role of accreting gas having different angular momentum compared to the disk which has formed early-on. We use simulations, where satellite galaxies accrete to the host halo, to show how infalling material can excite S-, U- and even lopsided warps. Those lopsided warps are the first seen in SPH simulations. Interestingly, a low-concentrated dark satellite with

the same orbital parameters as for the two-component system does not produce asymmetric warps as are frequently observed, excluding infall of such dark satellites as the primary reason for lopsided warped galaxies.

Our Galaxy is currently accreting satellites, e.g., the Large Magellanic Cloud (LMC). Ram pressure stripping removes gas from the satellite while it is spiraling in towards the Galaxy and the Magellanic Stream forms behind the LMC. The stream is expected to be deflected by the hot gaseous halo of the Milky Way, depending on the spin of the latter. Using a series of simulations with different spinning gaseous haloes we constrain the spin parameter of the hot halo of the Milky Way to be < 0.05. This indicates that the Milky Way is a spiral galaxy with a spin close to the average value.

Chapter 1

Introduction

In this chapter I provide first an overview to the broad field of galaxy formation. Then I will briefly review the framework within galaxies form, namely the standard cosmological model. The last part of this chapter is devoted to the numerical methods which have been used.

1.1 The current picture of disk galaxy formation

Galaxy formation is one of the most complicated phenomena within the field of cosmology. It involves a multitude of diverse physical processes operating on different scales and it is an inherently non-linear, three dimensional process. Currently, the most popular scenario for structure formation in the Universe is based on the inflationary cold dark matter (CDM) theory (Blumenthal et al. 1984), according to which cosmic structures arise from small Gaussian density fluctuations composed of non-relativistic collisionless particles. The dark matter aggregates into larger and larger clumps as gravity amplifies the weak density perturbations, produced at early times in the universe. Gas cools and condenses within these dark haloes, eventually forming the galaxies we see today (White & Rees 1978). This hierarchical picture of structure formation is an elegant and well defined theory that naturally explains the growth of large-scale structures from density fluctuations as small as those detected in the Cosmic Microwave Background to present-day galaxies. The CDM model however also has problems that might at the end lead to a deeper understanding of the nature and origin of cold dark matter and its interaction with baryonic matter (D'Onghia et al. 2006).

Although the gross picture seems to be understood quite well, there are a lot of remaining challenges. Most of the important processes for galaxy formation are only poorly understood, even when they are examined isolated, and often their importance to the problem of galaxy formation is not yet determined completely. It seems clear however, that all of the processes in the following list are relevant to some degree: (1) Evolution of the background cosmology. (2) Nonlinear gravitational collapse. (3) Infall and shock heating of gas. (4) Radiative cooling and heating processes. (5) Star formation. (6) "Feedback" by supernova explosions and stellar winds. (7) Galaxy interactions and mergers. (8) Chemical enrichment and stellar evolution. (9) Galactic winds. (10) Radiation transfer.

Almost all of the stars and the gas in disk galaxies are moving on circular orbits. Therefore angular momentum must govern the structure of such galaxies. In the standard picture of galaxy formation, the angular momentum of a dark matter fluctuation grows by tidal torques from nearby structures (Peebles 1969; White 1984), until the protogalaxy decouples from the Hubble flow and collapses further. It has been argued that gas and dark matter is initially well mixed (Fall & Efstathiou 1980) and therefore it is expected that the specific angular momentum distribution of the gas is equal to that of the dark halo. During the collapse of the protogalaxy the gas component dissipates its kinetic energy and decouples from the collisionless, violently relaxing dark matter component. The gas is then settling into an flattened, fast rotating disk where then stars will be formed. If the specific angular momentum would be conserved during the collapse to the equatorial plane, then the scale length of the galactic disk is directly related to the specific angular momentum of the halo. It has been shown (Fall & Efstathiou 1980 and later on Mo, Mao & White 1998) that in this case the expected disk scale lengths are in reasonable agreement with the observations (e.g. Courteau 1997).

In contrast to these analytical estimates, cosmological simulations have suffered on a a few major problems within this scenario. One generic difficulty of these studies has been that the radiative cooling of gas appears to be too efficient, such that a substantial luminosity excess of the simulated galaxies compared to the real universe results, the "overcooling" problem (e.g. White & Rees 1978; Navarro & Steinmetz 1997). A related problem concerns the angular momentum of gaseous disks assembled in this scenario. Simulations produce disks that were found to be too small and too centrally concentrated compared to those of observed galaxies. This is the so called angular momentum catastrophe of the gas (Navarro & Benz 1991; Navarro, Frenk & White 1995). It has been suggested the build-up of the galaxy is dominated by cold, dense lumps that transfer too much angular momentum to the dark halo by dynamical friction (Navarro & Steinmetz 2000). However this process has not been quantified and investigated in details.

Those two shortcomings have as well an impact on the spatial distribution of material within the disk: Up to now, no cosmological simulation produced a disk where the surface density profile is well fit by an exponential from the inner to the outer parts of the disk. Surface density profiles of those kind are observed quite often. Reproducing these galaxies is one of the biggest remaining challenges for the CDM paradigm. It is not clear if the inability to simulate a pure disk galaxy with the correct scale length is due to a fundamental flaw in the CDM model, or due to missing ingredients in the cosmological simulations, or perhaps due to numerical effects such as insufficient resolution. One of the missing physical mechanisms in many of the older simulations are heating processes, but Navarro & Steinmetz (1997) have shown that the ultraviolet background cannot alleviate the overcooling problem. It is believed that this might be resolved once feedback processes like supernova explosions or stellar winds are properly taken into account (see also section 1.4).

Another challenge for simulations of disk formation is matching the (empirically derived) Tully-Fisher (TF) relation. The TF relation links the characteristic rotation velocity V of a galaxy with its total absolute magnitude L (Giovanelli et al. 1997), usually given as $L \propto V^4$. This relation implies that the total disk mass and its radial distribution are closely connected with the total mass of the halo. Cosmological simulations (e.g. Governato et al. 2004) have shown a consistent offset from the TF relation with galaxies being too centrally compared compared to real ones. Most probably this offset is tightly connected to the already mentioned overcooling and angular momentum problem.

The question, how does gas get to the center of a dark matter halo, has probably more than one answer: In the classical picture, gas falling into a dark matter potential well is shock heated to approximately the halo virial temperature ($T_{vir} \approx 10^6$ for a Milky Way sized halo) putting it in quasi-hydrostatic equilibrium with the dark matter. Gas in the dense, inner regions of this shock-heated halo radiates its thermal energy, loses its pressure support , settles into a centrifugally supported disk and forms stars. Recently, Kereš et al. (2005) have shown using Smoothed Particle Hydrodynamics (SPH) simulation, that only about half of the gas follows the track expected in that conventional picture. The other half of the gas radiates its acquired gravitational energy at much lower temperatures, typically $T \approx 10^5$ and the histogram of maximum gas temperatures is clearly bimodal. Cold accretion is often directed along filaments, allowing galaxies to efficiently draw gas from large distances, while hot accretion is quasi-spherical. For low-mass galaxies the cold gas accretion dominates, while the conventional hot mode dominates the growth of of high-mass systems ($M_{halo} \gtrsim 10^{11.4}\ M_\odot$). This transition at $M_{halo} \sim 10^{11.4}\ M_\odot$ is similar to that found by Birnboim & Dekel (2003) using analytic arguments and one-dimensional simulations.

But the hot gaseous halo in high-mass haloes has not to be necessarily smooth, recent measurements of OVI and OVII absorption in the UV and X-ray part of the spectrum (Sembach et al. 2003) lend support to the idea that a lumpy gaseous Galactic halo exists and that such emission comes from the interface between warm clouds and the hotter diffuse medium. Maller & Bullock (2004) (in a similar way as already earlier Mo & Miralda-Escude 1996) suggested that the gas supply to galaxies is mostly in the form of discrete warm clouds. Small density and temperature fluctuations are enhanced by the cooling process resulting in a runaway instability and the formation of a fragmented distribution of cooled material, in the form of warm ($\sim 10^4$K) clouds, pressure-supported within the hot gaseous background. This model may explain the properties of high velocity clouds (HVCs) around the Milky Way (Blitz et al. 1999), for example their radial velocity distribution and angular sizes. If this picture is correct, then the HVCs of the Milky Way are tracers of the fundamental fuel supply that governs formation in the Universe. Very recent cosmological simulations (Governato et al. 2006, Sommer-Larsen 2006) have observed as well warm clouds around forming galaxies, the origin for the thermal instability in the hot halo is believed to be seeded by early cold accretion along filaments (Sommer-Larsen 2006).

In our own Galaxy one can still witness the ongoing processes of galaxy formation (for a sketch of those processes see Figure 1.1). The Milky Way is currently accreting e.g. the Magellanic Clouds, and numerous HVCs as well as the hot gas halo have been detected. In addition the Milky Way will merge in future with the Andromeda Galaxy, the nearest major spiral galaxy.

1.2 The standard cosmological model

The currently favoured theories of structure formation in the Universe assume that the structure (like galaxies, galaxy clusters and super-clusters) grows out of the primordial density fluctuations. Starting from almost homogeneous initial conditions, the fluctuations of the energy density of the order $\delta \sim 10^{-5}$, grow subsequently by gravitational instability. This picture represents nowaday the standard cosmological model and is supported by a large variety of observations. A detailed description of physical cosmology can be found

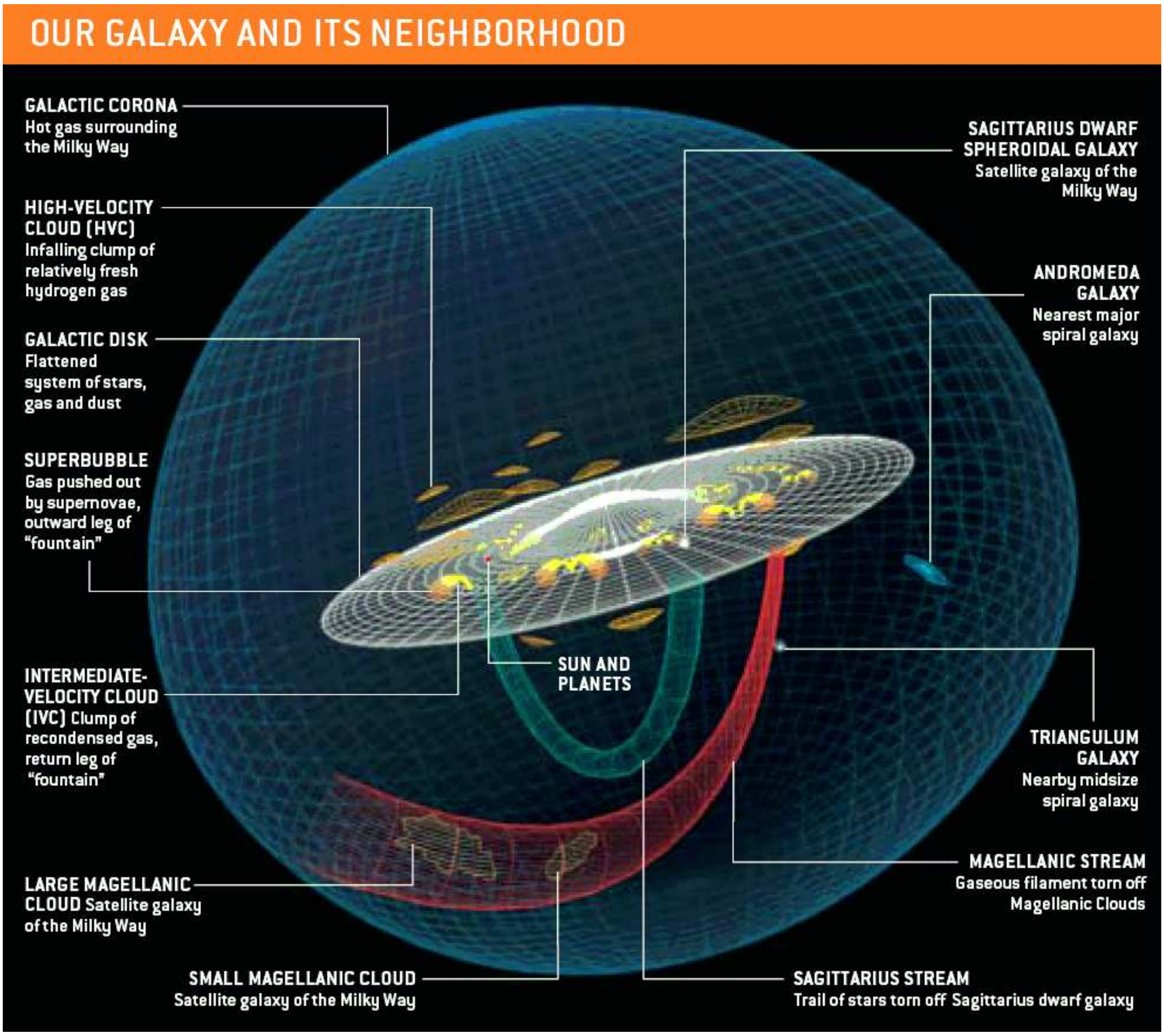

Figure 1.1: A sketch of the Milky Way and its neighbourhood. The Milky Way is currently accreting smaller galaxies and will merge with the Andromeda galaxy. Gas is accreted to the Galactic disk due to the warm clouds and from the hot halo (courtesy of Wakker & Richter, SciAm 2004).

in Peacock (1999).

For a global description, the Universe is usually taken to be a perturbed Friedmann-Robertson-Walker space-time with the dynamics governed by the Einstein equations:

$$G_{\mu\nu} = 8\pi G T_{\mu\nu} + \Lambda g_{\mu\nu}, \tag{1.1}$$

where G is the gravitational constant, $T_{\mu\nu}$ is the energy-momentum tensor, Λ the Cosmological Constant and $G_{\mu\nu}$ is the Einstein tensor. The line element for the metric $g_{\mu\nu}$ can be written as:

$$ds^2 = a^2 \left(\frac{dr^2}{1-kr^2} + r^2 d\Omega^2 \right), \tag{1.2}$$

where $k = +1, 0, -1$ describes the curvature of space, corresponding to an open, flat or closed Universe (spherical, flat or hyperbolic geometry).
The scale factor[1] a defines, for a given value of k, a one-parameter family of similar spaces. Its time dependence, leading to the Hubble constant $H(t)$, is found from the Einstein's (0-0) equation, the Friedmann equation:

$$H^2(t) \equiv \left(\frac{\dot{a}}{a}\right)^2 = \frac{8\pi G}{3}\rho - \frac{k}{a^2} + \frac{\Lambda}{3}, \tag{1.3}$$

where ρ is the density. The present value of the Hubble parameter is usually written as $H(t_0) = 100\,h\ \mathrm{km\,s^{-1}\,Mpc^{-1}}$ to parameterise uncertainties in the determination of the distance-scale of the Universe. The combined results of the WMAP satellite study of Cosmic Microwave Background anisotropies, large-scale structure, and Type Ia supernovae observations (Bennet et al. 2003) yield an best fit value of the Hubble constant of

$$H(t_0) = 71 \pm^4_3 \mathrm{km\,s^{-1}\,Mpc^{-1}}. \tag{1.4}$$

The Friedmann equation is usually rewritten by defining the critical density $\rho_c(t)$ corresponding to $k = \Lambda = 0$:

$$\rho_c(t) \equiv \frac{3H^2(t)}{8\pi G}, \tag{1.5}$$

(such that density values ρ above, below or equal to ρ_c refer to closed, open or flat universes) and by defining the ratios of different matter components i (including vacuum energy and curvature) as ratios of the critical density:

$$\Omega_i \equiv \frac{\rho_i}{\rho_c}, \qquad \Omega_\Lambda \equiv \frac{\Lambda}{3H^2}, \qquad \Omega_k \equiv -\frac{k}{a^2H^2}. \tag{1.6}$$

The Friedmann equation can thus be written:

$$\sum_i \Omega_i + \Omega_\Lambda + \Omega_k = 1. \tag{1.7}$$

By measuring the present values of all the density parameters (one can be eliminated using eq.(1.7)) and the present Hubble constant, we can track the history of the Universe back in time at least to an epoch where interchanges between the densities of different

---

[1] The redshift z is defined with the scale factor: $1 + z \equiv \frac{a_0}{a}$, where a_0 denotes the present value.

species occur. This is believed to be the case at neutrino decoupling shortly before nucleosynthesis.

One way to generate the observed perturbations is the inflationary scenario (see e.g. Peacock 1999). Inflation generates perturbations through the amplification of quantum fluctuations, which are stretched to observable astrophysical scales by a rapid exponential expansion. Several inflationary models have been invoked. The simplest ones generate two types of perturbations: Scalar field fluctuations which lead to density perturbations with a corresponding metric fluctuation and tensor metric fluctuations which can produce gravitational waves (see e.g. Koch 2003). Whereas the former will experience gravitational instabilities, leading to structure formation and observable objects, the latter can influence the Cosmic Microwave Background (CMB) anisotropies.

One of the fundamental consequences of the standard cosmological model is the prediction that the Universe has undergone in the past a hot phase, during which the cosmic temperature took a much higher value than that, $T_o \sim 2.7K$, which is today observed for the cosmic microwave background. The resulting cosmological framework of the hot Big Bang in a spatially homogeneous and isotropic Universe is widely accepted. Several indications point in favour of this model and the most striking and direct supports can be summarised as follows:

- The observed proportionality between the recessional velocity of galaxies and their distance (Hubble law), which is a natural consequence of assuming the Friedmann-Robertson-Walker metric.
- The detection and the high degree of isotropy of the cosmic microwave background radiation, which is the evidence of a primordial hot stage of the Universe, which has become colder due to the redshift, characterised by a high degree of homogeneity.
- The observed light element abundances, which match remarkably well the predictions of primordial nucleosynthesis, that represents an unavoidable step in the evolution of the hot Universe.

1.3 Numerical techniques

1.3.1 N-body methods

Obviously gravity is the driving forces for the evolution of the primordial density fluctuations. But also for variety of other astrophysical systems, namely formation of galaxies, gravity plays a key role. With assumptions of axisymmetry or perturbative approaches an impressive amount of progress has been made with analytical methods, particularly in the areas of solar system dynamics, stability of disks, stellar dynamics and quasi-linear aspects of the growth of large scale structure in the universe. In many systems of interest, however, non-linear interactions play a vital role. This ultimately requires the use of self-gravitating N-body simulations (for the following, see e.g. Wadsley et al. 2004).

Fundamentally, solving gravity means solving Poisson's equation for the gravitational potential, Φ, given a mass density, ρ:

$$\Delta\Phi = 4\pi G\rho, \tag{1.8}$$

where G is the Newtonian gravitational constant. In a simulation with discrete bodies it is common to start from the explicit expression for the acceleration **a** on a given body in terms of the sum of the influence of all other bodies,

$$\mathbf{a}_i = \sum_{i \neq j} \frac{GM_j(\mathbf{r}_i - \mathbf{r}_j)}{|\mathbf{r}_i - \mathbf{r}_j|^3}, \tag{1.9}$$

where the $\mathbf{r}_j$ and M_j are the position and masses of the bodies, respectively. When attempting to model collisionless systems, these same equations model the characteristics of the collisionless Boltzmann equation, and the bodies can be thought of as samples of the distribution function. In practical work it is essential to soften the gravitational force on some scale $r < \epsilon$, to avoid problems with the integration and to minimise two-body effects in cases where the bodies represent a collisionless system.

There are different methods used in literature to implement these ideas. One can classify those methods in three categories, which essentially differ in their prescriptions for evaluating the gravitational force between particles.

- Early N-body work such as studies of relatively small stellar systems were approached using a direct summation of the forces on each body due to every other body in the system (Aarseth & Lecar, 1975). This direct approach $\mathcal{O}(N^2)$ is impractical for large numbers of bodies, N, but has enjoyed a revival due to incredible throughput of special purpose hardware such as GRAPE (Hut and Makino, 1999). The GRAPE hardware performs the mutual force calculation for sets of bodies entirely in hardware and remains competitive with other methods on more standard floating point hardware up to $\sim 100,000$.

- A popular scheme for larger N is the particle-mesh (PM) method which has long been used in electrostatics and plasma physics. The adoption of PM was strongly related to the realisation of the existence of the Image fast Fourier transform (FFT) in the 1960s. The FFT is used to solve for the gravitational potential from the density distribution interpolated onto a regular mesh. In astrophysics sub-mesh resolution is often desired, in which case the force can be corrected on sub-mesh scales with local direct sums as in the particle-particle particle-mesh ($\mathrm{P}^3\mathrm{M}$) method. PM is popular in stellar disk dynamics, and $\mathrm{P}^3\mathrm{M}$ has been widely adopted in cosmology (e.g. Efstathiou et al. 1985). The particles masses must be interpolated onto a mesh, the Poisson equation is solved on the mesh, and the forces are interpolated back to the particles. Working in Fourier space also allows efficient force error control through optimization of the Green's function and smoothing. Fourier methods are widely recognised as ideal for large, fairly homogeneous, periodic gravitating simulations.

- The code employed in this work, PKDGRAV/GASOLINE (Stadel 2001, Wadsley et al. 2004) uses tree algorithms which are inherently $\mathcal{O}(N \log N)$. This approach recognises that details of the remote mass distribution become less important for accurate gravity with increasing distance. Thus the remote mass distribution can be expanded in multipoles on the different size scales set by a tree-node hierarchy. The tree approach can adapt to any topology, and thus the speed of the method is somewhat insensitive to the degree of clustering. Once a tree is built it can also be re-used as an efficient search method for other physics such as particle-based hydrodynamics. A particularly useful property of tree codes is the ability to efficiently calculate forces for a subset of the bodies. This is critical if there is a large range of time-scales in a simulation and multiple independent time-steps are employed. At the cost of force calculations no longer being synchronised among the particles substantial gains in time-to-solution may be realised. Multiple time-steps are particularly important for current astrophysical applications where the interest and thus resolution tends to be focused on small regions such as individual galaxies, stars or planets within large simulated environments. Dynamical times can become very short for small numbers of particles. Adaptive $\mathrm{P}^3\mathrm{M}$ codes are faster for full force calculations but are difficult to adapt to calculate a subset of the forces. The tree approach has the nice property of explicitly conserving momentum (as do PM and $\mathrm{P}^3\mathrm{M}$ codes).

1.3.1.1 N-body models

One aim of this work was to separate physical and numerical influences in galaxy formation. For that reason, it is more appropriate to use a well-understood, isolated, equilibrium halo model instead of using a full cosmological simulation. We describe in the following the dark matter N-body realisation we used, based on Kazantzidis et al. (2004). After having build an N-body halo, we used then analogous haloes to model the gas, we will give the details at the beginning of chapter 2.

There are two steps in constructing an isolated, equilibrium halo model: (1) find the phase-space distribution function (DF) of the desired model, and then (2) use Monte Carlo sampling of this DF to generate the N-body realisation. The first step constitutes the most difficult part. Simple, analytical DFs are known for only a handful of models, such as e.g. Plummer spheres (Plummer 1911), but none of the models known can provide a plausible description of the density profile $\rho(r)$ of a cold dark matter cosmological halo. In order to generate more realistic models one has to find numerically a steady state DF that reproduces the desired density and internal velocity anisotropy profiles.

Quite often the *local Maxwellian approximation* is used, where the self-consistent velocity distribution at a given point in space is approximated by a multivariate Gaussian whose mean velocity and velocity dispersion tensor are given by the solution of the Jeans equations at this point (for a description of this technique see e.g. Hernquist 1993). If one uses the local Maxwellian approximation to construct an N-body realisation of such a model, the center of the resulting N-body system will be far from equilibrium.

According to the Jeans theorem (Lynden-Bell 1962; Binney & Tremaine 1987, hereafter BT87), the most general DF of an equilibrium spherical system can depend on the phase-space coordinates $(\mathbf{r}, \mathbf{v})$ only through the isolating integrals of motion: the binding energy per unit mass, $\mathcal{E}$, and angular momentum vector per unit mass, $\mathbf{L}$. Obviously there are many DFs of the form $f(\mathcal{E}, \mathbf{L})$ that can produce any given density profile $\rho(r)$. We restrict our attention to a special class of non-rotating models with DFs of the form $f = f(Q)$, where

$$Q \equiv \mathcal{E} - \frac{\mathbf{L}^2}{2r_a^2} \tag{1.10}$$

(Osipkov 1979), with the additional constraint that $f(Q) = 0$ for $Q \leq 0$. In these models, the radial velocity dispersion $\sigma_r(r)$ is related to the tangential dispersions $\sigma_\theta(r) = \sigma_\phi(r)$

through

$$\beta(r) \equiv 1 - \frac{\sigma_\theta^2}{\sigma_r^2} = \frac{r^2}{r^2 + r_{\mathrm{a}}^2}. \tag{1.11}$$

Here r_{a} is the anisotropy radius, which controls the degree of global anisotropy in the velocity distribution. Inside r_{a} the velocity distribution is nearly isotropic, while outside r_{a} it becomes increasingly more radially anisotropic. In the limit $r_{\mathrm{a}} \to \infty$ the models reduce to isotropic models with Q corresponding to the total binding energy $\mathcal{E}$. The density profile of such a model is

$$\rho(r) \equiv \int f(\mathcal{E}, L)\, \mathrm{d}^3\mathbf{v}. \tag{1.12}$$

The inversion of the above integral equation gives the DF (Eddington 1916; BT87),

$$f(Q) = \frac{1}{\sqrt{8}\pi^2} \left[\int_0^Q \frac{\mathrm{d}^2\rho_Q}{\mathrm{d}\psi^2} \frac{\mathrm{d}\psi}{\sqrt{Q-\psi}} + \frac{1}{\sqrt{Q}} \left(\frac{\mathrm{d}\rho_Q}{\mathrm{d}\psi} \right)_{\psi=0} \right], \tag{1.13}$$

where $\rho_Q(r) \equiv \rho(r)(1 + r^2/r_{\mathrm{a}}^2)$, and $\psi(r) = -\Phi(r)$ is the relative gravitational potential.

Once the density $\rho(r)$ has been specified and the cumulative mass distribution $M(r)$, gravitational potential $\psi(r)$, and DF $f(Q)$ have been calculated, one can start to randomly sample particles from the DF. The particle positions are initialised using the cumulative mass distribution $M(r)$. Having the particle's position, the acceptance-rejection technique (e.g. Kuijken & Dubinski 1994) has been used to find its velocity.

1.3.2 Hydrodynamics

In the currently favoured picture of the universe, the ΛCDM model, it is assumed that most of the mass of the Universe is in the form of cold dark matter, which interacts only gravitationally. However, there is a significant contribution to the matter density from baryonic material and the luminous stars are made of baryons, providing the essential link to observations. To investigate galaxy formation one needs therefore a suitable treatment of the gas physics on cosmological scales (for the following, see e.g. Wadsley et al. 2004).

Astrophysical systems are predominantly at very low physical densities and experience wide-ranging temperature variations. Most of the material is in a highly compressible gaseous phase. In general this means that a perfect adiabatic gas is an excellent approximation for the system. Microscopic physical processes such as shear viscosity and diffusion can usually be neglected. High-energy processes and the action of gravity tend to create large velocities so that flows are both turbulent and supersonic: strong shocks and very high Mach numbers are common. Radiative cooling processes can also be important (see section 1.4); however, the timescales can often be much longer or shorter than dynamical timescales. In the latter case isothermal gas is often assumed for simplicity. Radiative transfer is always present but may not significantly affect the energy and thus pressure of the gas during the simulation.

Fluid dynamics solvers can be broadly classified into Eulerian or Lagrangian methods. Eulerian methods use a fixed computational mesh through which the fluid flows via explicit advection terms. Lagrangian methods follow the evolution of fluid parcels via the full (comoving) derivatives. This requires a deforming mesh or a mesh-less method such as Smoothed Particle Hydrodynamics (Monaghan 1992). Data management is more complex in these methods; however, advection is handled implicitly and the simulation tends to naturally adapt to follow density contrasts. Large variations in physical length scales in astrophysics have limited the usefulness of Eulerian grid codes. Adaptive mesh refinement (AMR) (e.g. Bryan & Norman 1997) overcomes this at the cost of data management overheads and increased code complexity. A fundamental limit to AMR in computational cosmology is matching the AMR resolution to the underlying dark matter resolution. Particle methods are also well suited to rapidly rotating systems such as astrophysical disks where arbitrarily many rotation periods may have to be simulated (e.g. SPH explicitly conserves angular momentum). A key concern for all methods is correct angular momentum transport, which we will investigate further for SPH in chapter two.

1.3.2.1 Smoothed Particle Hydrodynamics

Smoothed Particle Hydrodynamics is an approach to hydrodynamical modeling developed by Lucy (1977) and Gingold & Monaghan (1977). It is a particle method that does not refer to grids for the calculation of hydrodynamical quantities: all forces and fluid properties are found on moving particles eliminating numerically diffusive advective terms. SPH is a natural partner for particle based gravity. SPH has been combined with $\mathrm{P}^3\mathrm{M}$ (Evrard 1988), Adaptive $\mathrm{P}^3\mathrm{M}$ (Couchman et al. 1995) GRAPE (Steinmetz 1996) and tree gravity (Hernquist & Katz 1989). Parallel codes using SPH include Hydra MPI, the GADGET tree code (Springel et al. 2001) and GASOLINE (Wadsley et al. 2004), the code used for the hydrodynamical simulations in this work.

The basis of the SPH method is the representation and evolution of smoothly varying fluid quantities whose value is only known at disordered discrete points in space occupied by particles. Particles are the fundamental resolution elements comparable to cells in a mesh. SPH functions through local summation operations over particles weighted with a smoothing kernel, W, that approximates a local integral. The smoothing operation provides a basis from which to obtain derivatives. Thus, estimates of density related physical quantities and gradients are generated. The summation aspect led to SPH being described as a Monte Carlo type method (with $\mathcal{O}(1/\sqrt{N})$ errors).

A general smoothed estimate for some quantity f at particle i given particles j at positions $\mathbf{r}_j$ takes the form:

$$f_{i,\mathrm{smoothed}} = \sum_{j=1}^{n} f_j W_{ij}(\mathbf{r}_i - \mathbf{r}_j, h_i, h_j), \tag{1.14}$$

where W_{ij} is a kernel function and h_j is a smoothing length indicative of the range of interaction of particle j. It is common to convert this particle-weighted sum to volume weighting using $f_j m_j/\rho_j$ in place of f_j, where the m_j and ρ_j are the particle masses and densities, respectively. For momentum and energy conservation in the force terms, a symmetric $W_{ij} = W_{ji}$ is required. GASOLINE uses the kernel-average first suggested by Hernquist & Katz (1989),

$$W_{ij} = \frac{1}{2}w(|\mathbf{r}_i - \mathbf{r}_j|/h_i) + \frac{1}{2}w(|\mathbf{r}_i - \mathbf{r}_j|/h_j) \tag{1.15}$$

GASOLINE employs a fairly standard implementation of the hydrodynamics equations of motion for SPH (Monaghan 1992). Density is calculated from a sum over particle masses

m_j,

$$\rho_i = \sum_{j=1}^{n} m_j W_{ij}. \tag{1.16}$$

The momentum equation is expressed

$$\frac{d\mathbf{v}_i}{dt} = -\sum_{j=1}^{n} m_j \left(\frac{P_i}{\rho_i^2} + \frac{P_j}{\rho_j^2} + \Pi_{ij} \right) \nabla_i W_{ij}, \tag{1.17}$$

where P_j is pressure, $\mathbf{v}_i$ velocity and the artificial viscosity term Π_{ij} is given by

$$\Pi_{ij} = \begin{cases} \frac{-\alpha\frac{1}{2}(c_i+c_j)\mu_{ij}+\beta\mu_{ij}^2}{\frac{1}{2}(\rho_i+\rho j)} & \text{for } \mathbf{v}_{ij}\cdot\mathbf{r}_{ij} < 0, \\ 0 & \text{otherwise,} \end{cases} \tag{1.18}$$

$$\text{where } \mu_{ij} = \frac{h(\mathbf{v}_{ij}\cdot\mathbf{r}_{ij})}{\mathbf{r}_{ij}^2 + 0.01(h_i+h_j)^2}, \tag{1.19}$$

where $\mathbf{r}_{ij} = \mathbf{r}_i - \mathbf{r}_j$, $\mathbf{v}_{ij} = \mathbf{v}_i - \mathbf{v}_j$ and c_j is the sound speed. $\alpha = 1$ and $\beta = 2$ are coefficients used for the terms representing shear and Von Neumann-Richtmeyer (high Mach number) viscosities respectively. When simulating strongly rotating systems the multiplicative Balsara (1995) switch $\frac{|\nabla\cdot\mathbf{v}|}{|\nabla\cdot\mathbf{v}|+|\nabla\times\mathbf{v}|}$ is used to suppress the viscosity in non-shocking, shearing environments.

The pressure averaged energy equation (analogous to equation 1.17) conserves energy exactly in the limit of infinitesimal time steps but may produce negative energies due to the P_j term if significant local variations in pressure occur. GASOLINE uses the following equation, which also conserves energy exactly in each pairwise exchange but is dependent only on the local particle pressure,

$$\frac{du_i}{dt} = \frac{P_i}{\rho_i^2} \sum_{j=1}^{n} m_j \mathbf{v}_{ij} \cdot \nabla_i W_{ij}, \tag{1.20}$$

where u_i is the internal energy of particle i, which is equal to $1/(\gamma-1)P_i/\rho_i$ for an ideal gas. In this formulation entropy is closely conserved making it similar to alternative entropy integration approaches such as that proposed by Springel & Hernquist (2002).

1.4 From gas to stars

1.4.1 Cooling

The primary cooling processes relevant to galaxy formation are collisional (see e.g. White 1994, Katz et al. 1996). At temperatures above 10^6 K primordial gas is almost entirely ionised, and above a few $\times 10^7$ K enriched gas is fully ionised also. The only significant radiative cooling is then bremsstrahlung (free-free emission) due to the acceleration of electrons as they encounter atomic nuclei. At lower temperatures other processes are important. Partially ionised atoms can be excited by collisions with an electron, thereafter decaying radiatively to the ground state or electrons can recombine with ions. In both

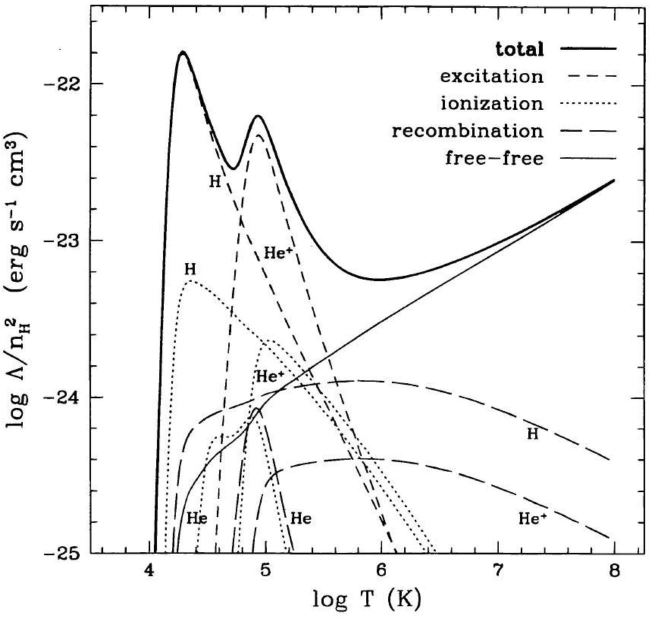

Figure 1.2: Cooling rates as a function of temperature for a primordial composition gas in collisional equilibrium. The cooling is dominated by collisional excitations at low temperatures and by bremsstrahlung (free-free emission) at high temperatures (plot taken from Katz et al. 1996).

cases the gas loses energy due to the radiated photon. Both processes depend strongly on the temperature T because of the temperature sensitivity of both the recombination coefficient and the ion abundance. For gas in ionisation equilibrium, the cooling rate per unit volume can be written as

$$\frac{du}{dt} = n_e n_H f(T), \tag{1.21}$$

depending on the temperature and the number densities of electrons and hydrogen, respectively. Cooling due to partially ionised atoms is the dominant case, for primordial gas it causes peaks in the cooling rate at 15,000 K (for H) and at 10^5 K (for He$^+$), see Figure 1.2 (where the cooling rate is normalised with the hydrogen density).

Gas with solar abundances has an enhanced cooling function, most pronounced at $\sim 10^6$ K. Other cooling processes in astrophysical situations are Compton cooling (photon - electron scattering) and collisional excitations of molecules (which becomes important below $\sim 10,000$ K). However, in most of the codes currently used in galaxy formation (including GASOLINE) cooling by molecules and metals is not implemented yet.

In GASOLINE a range of cases including adiabatic (no cooling), isothermal (instant cooling), and implicit energy integration are implemented. Hydrogen and Helium cooling processes have been incorporated as described before. Ionisation fractions are calculated assuming equilibrium for efficiency. GASOLINE optionally adds heating due to feedback from star formation, an uniform UV background or using user defined functions.

1.4.2 Star formation and feedback

The first steps of galaxy formation (dark matter forms virialised haloes, gas then falls into the potential wells provided by the dark matter and sinks to the center due to radiative cooling processes) seem to be understood conceptually reasonable well. However, there are two problems considering star formation: On one hand, important parts of several physical processes are not understood in detail, and on the other hand, galaxy formation simulations are far away from resolving individual stars or the fine structure of molecular clouds.

An overview to the physical processes which govern star formation draws the following picture: Condensation of gas leads to the formation of a complex multi-phase interstellar medium. Among the phases one also expects a population of giant molecular clouds. These complexes may fragment or collide with each other. Eventually, the cores of molecular clouds may undergo collapse down to stellar densities, with the subsequent onset of thermonuclear reactions. It is not well understood, what triggers the collapse, nor what the mass spectrum of the formed stellar population is going to be. When a new stellar association has formed, its UV radiation can ionise gas and significantly alter the thermodynamic properties of the interstellar and intergalactic medium. The stars may also affect the surrounding gas by powerful mass-loaded winds. Furthermore, most massive stars will only live a short time, and then explode as supernovae. The powerful shock waves of supernovae can blow holes in the interstellar medium, or they might blow it away entirely in small dwarf galaxies. All these processes associated with star formation deposit energy back to the into the gaseous medium, and are therefore refereed to as feedback. Unfortunately, the current understanding of the detailed mechanisms of feedback is probably even worse than that of star formation. However, feedback is thought to provide an important regulation mechanism for star formation (Springel 1999).

Given this difficulties, star formation cannot be treated from first principles at this point. Nevertheless, meaningful comparisons between observations and simulations of galaxies require that simulations include gas and stars. Gas and stars provide the photons that comprise observations. For the foreseeable future, galaxy simulations will not be able to resolve individual stars, their individual explosions as supernovae, or the fine structure of gas clouds in the context of a galaxy. Simulation strategies for star formation have usually adopted one of two approaches. In one approach, one focuses on a very small patch of the interstellar medium, e.g. a cold molecular cloud, and then tries to follow its evolution with very high numerical resolution. If one attempts to simulate the formation of whole galaxies, one has to use a heuristic recipe to model the subresolution physics of star formation and the feedback effect of supernovae explosions. However, up to now, a physically well motivated model of star formation and feedback processes, which reproduce the observational data closely, is still missing.

Chapter 2

Angular momentum transport and disk morphology in SPH simulations of galaxy formation[1]

2.1 Abstract

We perform controlled N-Body/SPH simulations of disk galaxy formation by cooling a rotating gaseous mass distribution inside equilibrium cuspy spherical and triaxial dark matter haloes. We systematically study the angular momentum transport and the disk morphology as we increase the number of dark matter and gas particles from 10^4 to 10^6, and decrease the gravitational softening from 2 kpc to 50 parsecs. The angular momentum transport, disk morphology and radial profiles depend sensitively on force and mass resolution. At low resolution, similar to that used in most current cosmological simulations, the cold gas component has lost half of its initial angular momentum via various numerical and physical mechanisms. The angular momentum is transferred primarily to the hot halo component, by resolution-dependent hydrodynamical and gravitational torques, the latter arising from asymmetries in the mass distribution. In addition, disk-particles can lose angular momentum while they are still in the hot phase by artificial viscosity. In the central disk, particles can transfer away over 99% of their initial angular momentum due to spiral structure and/or the presence of a central bar. The strength of this transport also depends on force and mass resolution - large softening will suppress the bar instability, low mass resolution enhances the spiral structure. This complex interplay between resolution and angular momentum transfer highlights the complexity of galaxy formation even in isolated haloes. With 10^6 gas and dark matter particles, disk particles lose only 10-20% of their original angular momentum, yet we are unable to produce pure exponential profiles due to the steep density peak of baryons within the central kpc. We speculate that the central luminosity excess observed in many Sc-Sd galaxies may be due to star-formation in gas that has been transported to the central regions by spiral patterns.

---

[1] This chapter (Kaufmann et al. 2006b, astro-ph/0601115) was submitted to MNRAS.

2.2 Introduction

Numerical simulations have become the most powerful tool to explore the complex problem of galaxy formation. Within the current paradigm of galaxy formation realistic rotationally supported disks can form if the gas retains the angular momentum gained from tidal torques as it cools within a cold dark matter (CDM) halo (White & Rees 1978; Mo, Mao & White 1998). However, up to now SPH simulations of galaxy formation in a cosmological context achieved limited success in supporting this scenario. The simulated disks were found to be too small and too centrally concentrated compared to those of observed galaxies, apparently because the build-up of the galaxy is dominated by cold, dense lumps that lose too much angular momentum by dynamical friction (Navarro & Benz 1991; Navarro & Steinmetz 1997). The mismatch in the disk size has been reduced from the order of magnitude difference of several years ago to a factor of order two in the most recent simulations thanks to both higher resolution and the inclusion of energetic feedback mechanisms which partially suppress the cold lumps (Governato et al. 2004; Sommer-Larsen, Götz & Portinari 2003; Thacker & Couchman 2000; Abadi et al. 2003; Robertson et al. 2004). Even in the latest simulations the internal structure of galaxies is still barely resolved (Abadi et al. 2003). Therefore it is unclear how robust these results are, especially since detailed convergence studies such as those existing in other areas of cosmology and astrophysics (e.g. Power et al. 2003 for dark matter haloes) are still lacking.

Observationally, many galaxies are single component disks with a nearly exponential surface density profile. Reproducing these galaxies is one of the biggest remaining challenges for the CDM paradigm. It is not clear if the inability to simulate a pure disk galaxy with the correct scale length is due to a fundamental flaw in the CDM model, or due to missing ingredients in the cosmological simulations, or perhaps due to numerical effects such as resolution. It is claimed that low resolution simulations ($N \sim 10^4$) suffer from excessive artificial viscosity that can cause spurious angular momentum losses (Thacker et al. 2000; Sommer-Larsen, Gelato & Vedel 1999). Moreover, for disks embedded in poorly resolved haloes two-body-effects will lead to a substantial angular momentum loss even during the late stages of disk formation (Mayer 2004), and would induce spurious heating of the gas component (Steinmetz & White 1997).

On the other hand central dense stellar nuclei have been seen in several late-type spiral galaxies, for example, in M33 (Regan & Vogel 1994), but also in other late-type spirals (Carollo et al. 1998, Carollo 1999), and the semi-analytical models of Van den Bosch (2001) produced disk galaxies with surface density profiles which slopes were steeper near the center than an exponential.

In this chapter we investigate various numerical effects that can potentially compromise the results of current simulations of galaxy formation. We will focus in particular on the evolution of the angular momentum of forming disks and on how that depends on mass and force resolution as well as on other parameters of a simulation, including how the initial conditions are set up. Our study considerably extends a similar one recently carried out by Okamoto et al. (2003).

For this investigation we will use N-Body+SPH simulations having between 10^4 and 10^6 dark matter and SPH particles. We will also explore the effects of force resolution at a fixed mass resolution. The simulations will follow the formation of a large galaxy with mass comparable to the Milky Way and of a smaller galaxy with dark and baryonic mass comparable to that of the Local Group spiral M33. The central disks form by the cooling of gas inside equilibrium dark matter haloes in which the gas is set to initially rotate in accordance with expectations from cosmological simulations, either by construction or set by mergers between equilibrium non-rotating haloes.

Cosmological simulations suggest that the large disks of spiral galaxies form mainly from the smooth accretion of gas after the last major merger (Sommer-Larsen, Götz & Portinari 2003; Abadi et al. 2003; Governato et al. 2004) and heating by cold dark matter substructure is not expected to affect disk properties dramatically (Font et al. 2001). Therefore, although our simulations do not follow the hierarchical growth of structure in a full cosmological context, they can model with unprecedented detail the gas accretion phase which characterises the main epoch of disk formation. The controlled experiments presented in this chapter are thus complimentary to cosmological simulations, allowing us to directly explore not only the consequences of varying the resolution, but also the effect of different recipes of star formation and different treatments of the gas thermodynamics.

The outline of the chapter is as follows. In section 2.2 we present the modeling of our initial conditions, and the treatment of cooling and star formation. In section 2.3 we give an overview of the results of the simulations and discuss the resolution dependence of our results, focusing in particular on the analysis of the angular momentum transport. We discuss the dependence of disk formation on star formation (section 2.4) and on different ways of setting up the initial conditions (section 2.5), we then summarise and conclude in section 2.6.

2.3 Initial Conditions

Our initial conditions comprise an equilibrium NFW galaxy-sized halo with an embedded spinning gaseous mass distribution in hydrostatic equilibrium, using models having from 250 dark matter & 30,000 gas particles up to 1 million dark matter & gas particles. We do not include any heating source such as the cosmic UV background or feedback from supernovae. In most of the simulations we enforce a lower limit for the temperature that the gas can reach via radiative cooling. This can be seen as a crude way to mimic the effect of the missing heating sources (see also section 2.6.1 and Barnes 2002).

The halo models are built as in Kazantzidis, Magorrian & Moore (2004), and hence they include a self-consistent description of the velocity distribution function. In order to initialize the dark halo we start by choosing the value of its circular velocity at the virial radius, v_{vir}, which, for an assumed cosmology (hereafter $\Omega_0 = 0.3, \lambda = 0.7, H_0 = 70$ kms^{-1} Mpc^{-1}) automatically determines the virial mass, M_{vir}, and virial radius, r_{vir}, of the halo (Mo, Mao & White 1998). For the main model used in this work we choose $v_{vir} = 140$ km/s, which corresponds to $r_{vir} = 200$ kpc and therefore and $M_{vir} = 9.14 \times 10^{11} M_{\odot}$. Haloes have NFW density profiles (Navarro, Frenk & White 1996) characterized by a halo concentration c, defined as $c = \frac{r_{vir}}{r_c}$, where r_c is the halo scale radius. For our main model we consider $c = 8$, which is typical for massive galaxy haloes (see Bullock et al. 2001a).

The gaseous halo of our fiducial model is constructed in the same way and contributes 9.09% of the total mass of the system. The temperature structure (see Figure 3.1) of the gaseous halo is calculated by solving the equation for the hydrostatic balance of an ideal gas inside a dark matter halo, as done in Mastropietro et al. (2005). Assuming an isotropic model, the halo temperature at a given radius r is determined by the cumulative mass distribution $M(r)$ of the dark and gaseous components beyond r and by the density profile $\rho_h(r)$ of the hot gas:

$$T(r) = \frac{\mu}{k_B} \frac{1}{\rho_h(r)} \int_r^\infty \rho_h(r) \frac{GM(r)}{r^2} \, dr \,, \tag{2.1}$$

where μ is the mean molecular weight, G and k_B are the gravitational and Boltzmann constants. The hot gas starts with a specific angular momentum distribution motivated by the results of cosmological simulations; the initial specific angular momentum profile is well fit by a power law following $j \propto r^{1.0}$, whereas the dark matter halo has no angular momentum (Bullock et al. 2001b proposed a power law with $j(r) \propto r^{\alpha}, \alpha = 1.1 \pm 0.3$.). In the Milky Way models we used $\lambda = 0.038$ for the spin parameter, defined as $\lambda = \frac{j_{gas}|E|^{0.5}}{GM^{1.5}}$, where j_{gas} is the average specific angular momentum of the gas, E is total energy of the halo and G is the gravitational constant. This definition matches the one commonly used (e.g. Mo, Mao & White 1998) under the assumption that there is no angular momentum transport between the spherical dark matter halo and the gas. This transport turned out to be small, see section 3.1.

The mass of dark matter particles varies between $3.44 \times 10^7 M_\odot$ in the low resolution runs and $1.66 \times 10^5 M_\odot$ in the high resolution runs. For the highest resolution models we used a dark matter halo with variable particle masses, with the resolution increasing towards the center of the system. These shell models comprise: $600,000$ particles distributed in the inner sphere with 20 kpc radius, $300,000$ particles in the next shell out to 100 kpc, while the rest of the halo is sampled with only $100,000$ particles. With a single-resolution model one would need about ten million particles to reach a comparable resolution in the central region. This allows us to resolve the central dark matter cusp to a scale of ~ 100 parsecs in the MW model. The reliability of these initial conditions is tested and reported in Zemp et al. (2006, in preparation). The mass of gas particles varies from $3.4 \times 10^6 M_\odot$ in the low resolution runs to $2.0 \times 10^5 M_\odot$ in the high resolution runs. For the gas we did not use a shell model because smoothing over particles of different masses in an SPH code can produce spurious results (Kitsionas & Withworth 2002). We provide an overview of the main simulations carried out in Table 2.1 and the initial density and temperature profiles of our models are shown in Figure 3.1. In section 2.6.2 we describe an alternative way of building the initial conditions that more closely resembles what happens in a full cosmological framework.

We also carry out a set of simulations with a less massive halo, comparable to that expected for the nearby spiral galaxy M33 (Corbelli 2003), such that $M_{vir} = 5.3 \times 10^{11} M_\odot$, concentration $c = 6.2$, spin parameter $\lambda = 0.105$. Since we want to use this model to produce a low mass spiral such as M33 we also adopt a lower baryon fraction, $f_b = 6\%$, which after 5 Gyr of cooling gives a similar cold baryonic component as observed within this galaxy. We consider two different initial specific angular momentum profiles for the gas, $J \propto r^{1.0}$ (M33A), as for the Milky Way model, and $J \propto r^{0.5}$ (M33B) (we keep the total angular momentum inside the virial radius fixed). In the "standard" M33 model the hot gaseous halo is resolved with 5×10^5 particles of mass $\sim 10^5 M_\odot$. We will also present some results from the "refined" simulation where we resolve the gas phase down to 3000 $M_\odot$ using a splitting of the SPH particles (see Kaufmann et al. 2006a and references therein). We adopt a force resolution of $\epsilon = 0.25$ and $\epsilon = 0.1$ kpc for the standard and hi-res run, respectively, see Table 2.2. In contrast to the Milky Way runs this model cools a lower fraction of baryons into the final disk, which allows us to run at a higher resolution

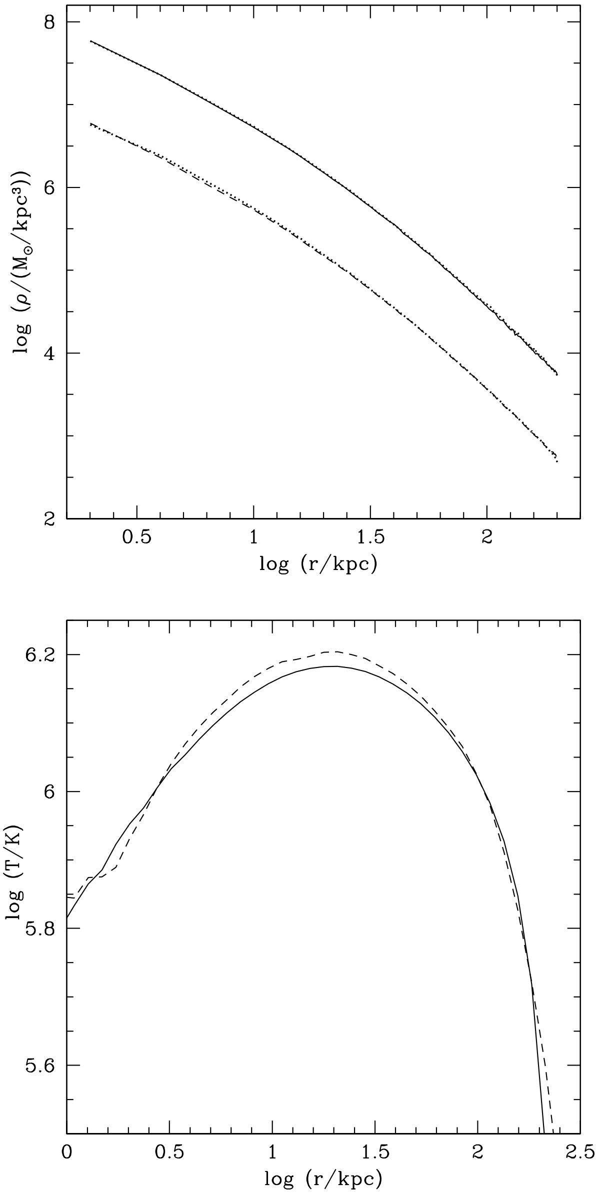

Figure 2.1: The upper panel shows the initial radial density profiles of gas (lower curve) and dark matter (upper curve). The gas and dark matter densities after 3 Gyr of evolution with an adiabatic equation of state are over-plotted and as expected the density profile changes only very little. The lower panels shows the initial temperature profile of the gas (solid) and after 5 Gyr of evolution with an adiabatic equation of state (dashed line) having only small deviations from the initial temperature.

since the central disk does not achieve such high densities thus relaxing the requirements on the time-step size.

Initial conditions similar to those employed here have been used in Robertson et al. (2004) and Okamoto et al. (2003), however we will compare simulations that have much higher force and mass resolutions. Finally, the semi-analytical work of van den Bosch (2001) also uses an initial setup that is quite similar in spirit, in which they follow in one dimension the collapse of shells of a rotating gas distribution inside an NFW halo. This makes an interesting comparison since it is naturally free of numerical effects.

To evolve the models we use the parallel TreeSPH code GASOLINE, which is described in Wadsley, Stadel & Quinn (2004). The code is an extension to the N-Body gravity code PKDGRAV developed by Stadel (2001). It uses an artificial viscosity which is the shear reduced version (Balsara 1995) of the standard Monaghan (1992) artificial viscosity. GASOLINE solves the energy equation using the asymmetric form and conserves entropy closely. It uses the standard spline form kernel with compact support for the softening of the gravitational and SPH quantities. The code includes radiative cooling for a primordial mixture of helium and (atomic) hydrogen. Because of the lack of molecular cooling and metals, the efficiency of our cooling functions drops rapidly below 10,000 K. Nearly all simulations adopt a temperature floor which is higher than this cut-off (see section 5.1) so as to crudely mimic the effect of heating sources such as supernovae explosions and radiation (e.g. ultraviolet) backgrounds. The star formation recipes are described in section 2.5.

Name	Resolution (dark /gas particles)	softening [kpc]	$T_{cut-off}$ [kKelvin]	art. viscosity	star formation
LR	3×10^4/ 3×10^4	2	30	standard	no
LRLS	3×10^4/ 3×10^4	0.5	30	standard	no
LRLD	2.5×10^2/ 3×10^4	5	30	standard	no
IR	9×10^4 / 9×10^4	2	30	standard	no
IRLS	9×10^4 / 9×10^4	0.5	30	standard	no
IRLSSF	9×10^4 / 9×10^4	0.5	30	standard	Katz 1992
IRLSSFHE	9×10^4 / 9×10^4	0.5	30	standard	Katz high efficiency
IRLSNL	9×10^4 / 9×10^4	0.5	30	no shear reduction	no
IRLSMD	9×10^5 / 9×10^4	0.5	30	standard	no
HR	1×10^6 / 5×10^5	2	30	standard	no
HRLS	1×10^6/ 5×10^5	0.5	30	standard	no
HRSFT	1×10^6/ 5×10^5	2	30	standard	Temperature criterion

Table 2.1: Overview of the numerical parameters of the main simulations of the Milky Way model. Here and in the following, LR, IR and HR indicate the resolution used, LS the use of small softening and SF the use of star formation.

Name	Resolution (dark /gas particles)	softening [kpc]	$T_{cut-off}$ [kKelvin]	art. viscosity	Angular momentum profile
M33A	1.1×10^6/ 5×10^5	0.25	30	standard	$\propto r^{1.0}$
M33B	1.1×10^6/ 5×10^5	0.25	30	standard	$\propto \sqrt{r}$
refined M33A	2.2×10^6/ 4×10^6	0.1	15	standard	$\propto r^{1.0}$

Table 2.2: Overview to the numerical parameters of the main simulations of the M33 model.

Name	central object	radius [kpc]
LRLD	blob plus 2 fragments	2
LR	thick disk	4
LRLS	thick disk	4
IR	disk	5.6
IRLS	barred disk	6.3
IRLSNL	barred disk	5.7
IRLSSF	barred disk	5.9-6.7
IRLSSFHE	barred disk	6.5-7
IRLSMD	barred disk	6
HR	disk, oval	5.3-6
HRLS	barred disk	6.9
HRSFT	disk	6.6

Table 2.3: The morphology and size of the central disk after 5 Gyr of evolution for the different simulations of the Milky Way model.

2.4 Results of the simulations

We first test the equilibrium of the combined gas and dark matter halo by evolving it using an adiabatic equation of state. We find that the mass inside the virial radius varies only by $\sim 0.5\%$ after 5 Gyr of evolution (e.g. for the IR simulation), see also Figure 3.1. The temperature and density profiles of the gas also undergo minimal variation (Figure 3.1). In the following we describe the results of the runs in which the spinning gas cools radiatively inside the halo and gradually settles into a centrifugally supported central object. We run all the simulations for at least five billion years. We give an overview of the different runs in table 2.3. We begin with discussing the numerical convergence of the basic properties such as the mass and the angular momentum of the central cold baryons. We then study the morphological evolution of the central disk and the dependence of results on the initial conditions.

2.4.1 Convergence in mass and angular momentum

The main simulations are done at three different resolutions: LR, IR, HR. Moreover, in order to compare with the results of Steinmetz & White (1997), we re-simulated the LR run with smaller number of dark particles, such that the mass of the dark particles exceeds the critical mass given in their work by a factor of 2 (run LRLD). Above this critical mass, two-body encounters are expected to produce spurious heating that overwhelms radiative cooling, thus suppressing the amount of accreted mass. We find comparable accretion of cold gas mass between the runs LR, IR and HR. However, we confirm qualitatively the results of Steinmetz & White (1997) with the LRLD run: in this case the cold gas mass is reduced by a factor of 1.6 compared to the other runs because of spurious heating see Figure 2.2. (Note that this is slightly lower than that found by those authors because we use a higher cut-off in the cooling function.)

We measured the specific angular momentum of the central cold particles with $T < 80,000$ K. We use this temperature threshold instead of $30,000$ K (the effective tempera-

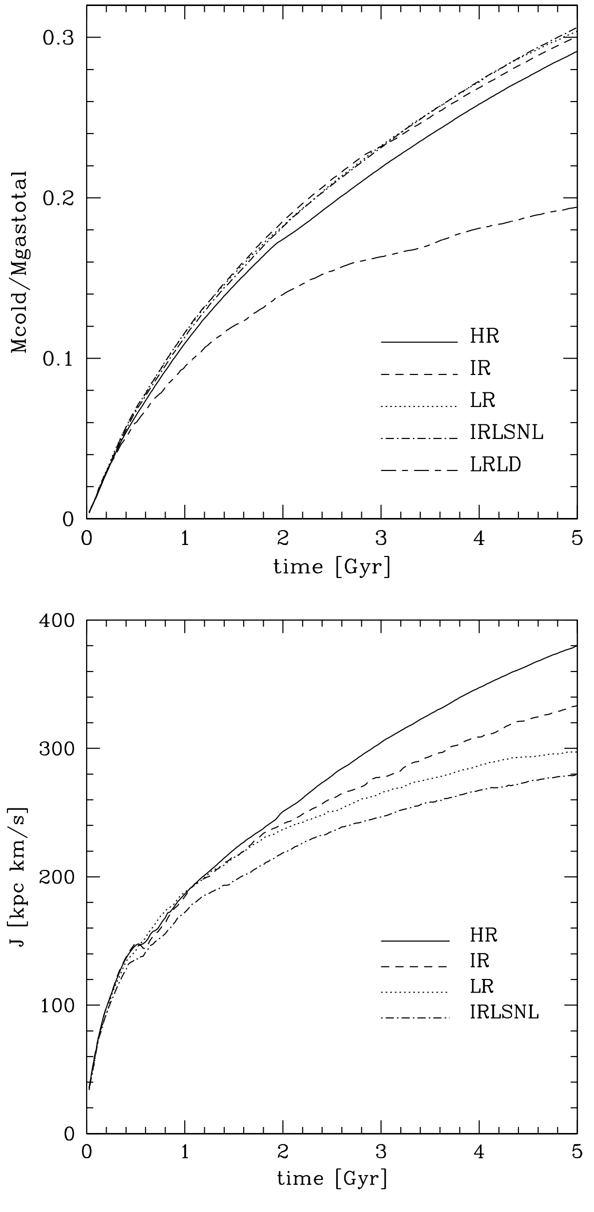

Figure 2.2: Upper panel: Growth of the cold mass fraction (equivalent to the disk mass fraction) for gas particles that were initially inside a sphere of radius 80 kpc. Lower panel: Accretion of specific angular momentum of the cold gas disk for particles within the same sphere. HR is plotted with solid, IR with dashed, LR with dotted, LRLD with long dashed - short dashed and IRLSNL with dashed-dotted lines. We find convergence in terms of of evolution of the cold mass fraction but not in terms of evolution of the angular momentum of the cold particles.

ture of the disk) to include also those particles that are near the edge of the disk and are about to be accreted. We checked that the results reported below are not strongly affected by the precise way in which we identify cold particles (e.g. $T < 50,000$ K or $T < 80,000$ K).

We find that even with more than 10^5 gas particles convergence in the final angular momentum is not reached. In fact the disk in the high resolution HR runs (with $500,000$ gas particles) accreted $\sim 30\%$ more specific angular momentum than LR and still $\sim 13\%$ more than the IR run, see Figure 2.2. Over the 5 Gyr of evolution, the simulations conserve total angular momentum better than one part in a hundred. The particles which are in the disk after 5 Gyr start with an initial specific angular momentum of ~ 500 kpc km/s in the hot phase and lose as they cool to the disk then 20%, 33% and 41% in the HR, IR and LR simulations, respectively. The hot component gains 30 (15)% and the dark halo gains 10 (5)%, in the LR and HR runs (the latter in parentheses). Correspondingly the size of the central disk also varies with resolution; within the LR runs it measures ~ 4 kpc whereas we find ~ 7 kpc for the HR run, see Table 2.3 and Figure 2.3. This exchange of angular momentum between hot and cold gas particles is also visible in a slightly different way in Figure 2.4, where we followed the angular momentum of either hot or all gas particles in a given shell at different resolutions. From thus we see that the hot phase ($T > 80,000$ K) gains whereas all the gas particles from that shell and therefore also the cold phase ($T < 80,000$ K) loses angular momentum, and that this depends sensitively on resolution.

Most of the angular momentum loss occurs in the central disk. Despite the quite modest overall loss of angular momentum of cold particles in the HR run, the particles which end up in a sphere of 1 kpc radius around the centre have lost $\sim 80\%$ of their specific angular momentum over 5 Gyr. This loss can be even larger for particles which end up in the central region of the galaxy in the runs of the M33 model (see section 2.6.3). We plot the initial specific angular momentum of every particle over the final (at time 4.8 Gyr) in Figure 2.5. The overall loss in the M33A run was 14%, whereas for this inner 1 kpc region 88% of the specific angular momentum was lost. Another way to look at this is to compare the angular momentum evolution of different rings in the disk around the centre, which is done in Figure 2.6.

In addition to the angular momentum loss in the central disk we found that a substantial fraction of the particles which end up in this inner region do lose angular momentum while they are still part of the hot halo. For those particles we measured the evolution of their angular momentum while they were in the hot phase. These particles lose 13 (6)% , in the LR and HR runs (the latter in parentheses) in the first Gyr. The reason for this transfer might be due to the hydrodynamical drag that particles and/or clumps of particles suffer as they move through the hot background. Gas particles will cool and form small clumps where there are fluctuations in density, and these fluctuations will be larger in low resolution simulations, perhaps explaining why the angular momentum loss is bigger than in the higher resolution simulations.

It is remarkable that we only find convergence in terms of the accreted cold mass but not in terms of angular momentum and disk sizes. In fact cold gas particles in LR runs end up with only 79% of the angular momentum attained in HR runs (the difference in disk sizes is at the 67% level).

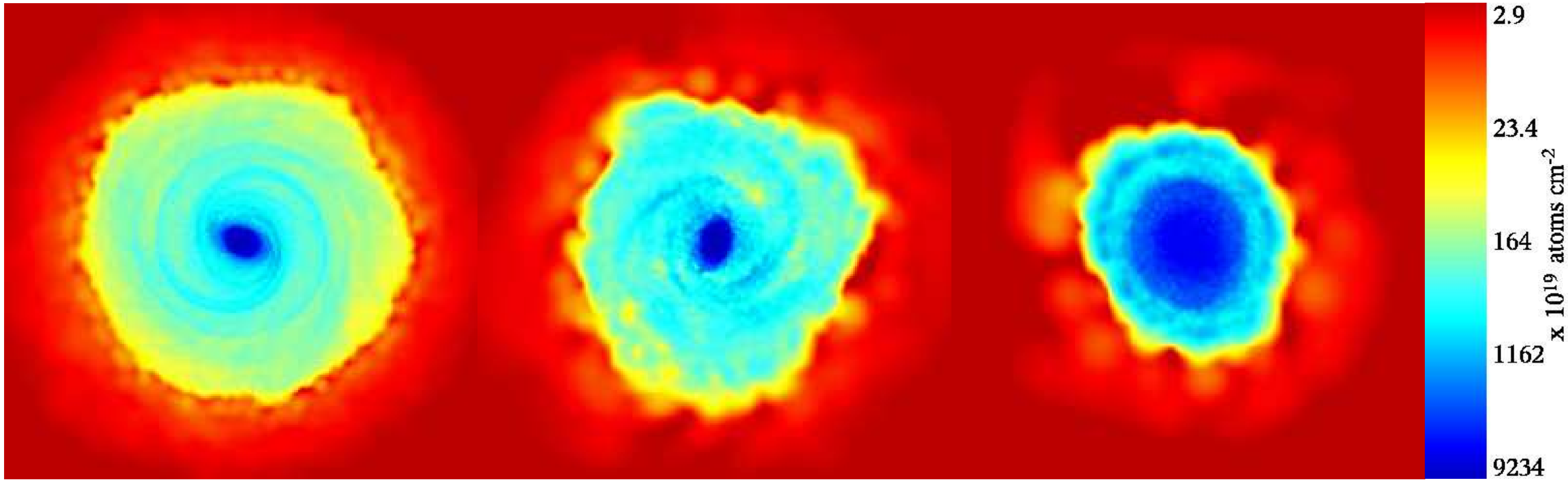

Figure 2.3: The three panels show density maps of gas in a slice through the centre of the Milky Way gas disk after 5 Gyr, from left to right: HRLS, IRLS, LRLS. Box side length 20 kpc for every panel - clearly the disk is larger for higher resolution and the bulge to disk ratio lower.

We also investigated the role that the artificial viscosity can have in the spurious dissipation of angular momentum. In all the runs we adopt the standard Monaghan form of the viscosity (Monaghan 1992), and in most of them we followed Balsara (1995), who proposed to include a term to reduce excessive dissipation of momentum in shear flows such as those present in differentially rotating disks. Without the Balsara term the angular momentum of the disk for the IR run grows less without it, see Figure 2.2. The difference between the two cases is comparable to the difference between low and intermediate resolution, implying that the Balsara term is still important as long as the number of gas particles is of order 10^5. Similar conclusions for lower resolution runs were found in previous works, for example Thacker et al. (2000).

2.4.2 Torques and losses from smoothing and artificial viscosity

Okamoto et al. (2003) have pointed out, that there is significant transfer of angular momentum from the cold gas disk to the ambient hot halo gas due to spurious pressure gradients across the interface between the two phases. These gradients arise because hot particles belonging to the diffuse halo but located near the edge of the much denser disk have their density overestimated via the SPH smoothing calculation. This problem has led some authors to explicitly decouple the cold and hot phase in the SPH smoothing (Pearce et al. 1999; Marri & White 2003).

We now examine the torques which may cause the transfer of angular momentum between the cold and the hot phase, including their resolution dependence. We measured separately the torques arising from, respectively, gravitational and hydrodynamical forces (including both pressure and artificial viscous forces) acting on disk particles after 5 Gyr of evolution. First of all one should notice that in the low resolution runs (e.g. LR) both the gravitational and hydrodynamical torques are always significantly larger than those in the high resolution runs (HR), as shown by the two upper plots of Figure 4.9. Gravitational and hydrodynamical torques are also comparable at a given resolution. The total hydrodynamical torques normalised by the angular momenta of the cold gas disk (T/J) are -0.13 and -0.02 Gyr^{-1} for the LR and HR run, respectively. These numbers are much smaller than the values (~ -0.9 Gyr^{-1}) found in the paper of Okamoto et al. (2003). This is not surprising since even the LR run has ≈ 5 times more gas particles in the disk than in the (cosmological) simulation of Okamoto et al. (2003).

We then compute separately SPH forces arising from the cold gas (i.e. from the disk itself) and those arising from the hot gas component. For high resolution (HR) the torques between the hot and the cold phase are quite small but together with the losses in the hot phase and during the bar instability, see section 4, are enough to explain the measured angular momentum loss (assuming the magnitude of these torques is typical for the entire 5 Gyr of evolution) whereas at low resolution (LR) the same torques are much bigger and there is a significant additional contribution from gravity torques (upper right plot of Figure 4.9). Indeed, the gravitational interaction between the cold phase and the dark halo also causes angular momentum transport in the LR simulation; the solid lines in the lower left plot of Figure 4.9 indicates that the torques from halo particles on disk particles are of the same order as the hydro torques. The disk did not grow exactly at the centre of mass of the dark halo (the misalignment was of order of the softening length) and this asymmetry (which was not observed in the HR run) appears to be the origin of this torque. In the lower right plot of Figure 4.9 we examine the hydro and gravitational torques acting

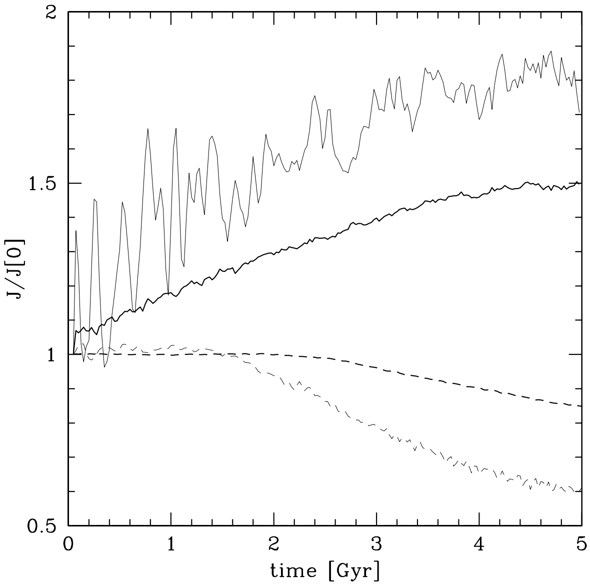

Figure 2.4: The time evolution of the specific angular momentum for gas particles which were initially in a shell from 30 kpc to 40 kpc around the centre. All gas particles from that shell of HRLS (dashed line), gas particles from the same shell which remain hot during the simulation (solid line). The equivalent for LRLS, is also plotted but with thinner lines. At lower resolution the loss of angular momentum in the cold phase is larger than for high resolution.

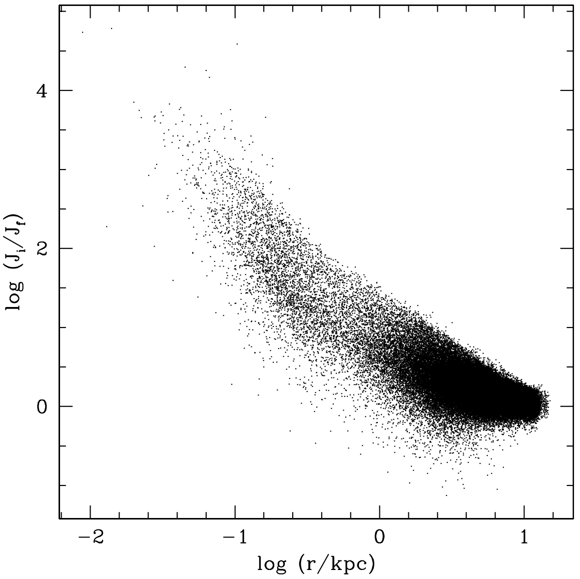

Figure 2.5: For the gaseous disk particles in the M33A model we plot the initial specific angular momentum over the final (measured at 4.8 Gyr) versus radius. The angular momentum loss in the centre can be very large.

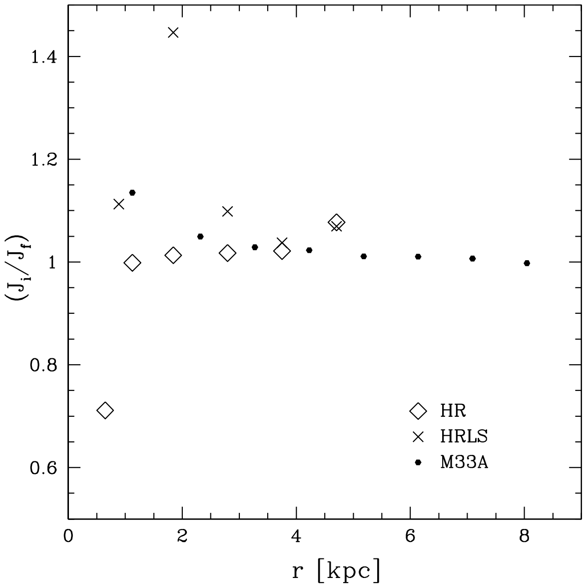

Figure 2.6: The ratio of the specific angular momentum of disk particles after 2.8 Gyr (J_i) and after 3.8 Gyr (J_f) is plotted versus radius. HR with open symbols, HRLS with crosses and M33A with filled symbols. The innermost point of the HR run has already lost most of its angular momentum before 2.8 Gyr during the bar instability phase at $\sim$ 1 Gyr, therefore the gain here is insignificant. In the HRLS run the spiral arms are redistributing angular momentum in the whole disk whereas for the M33A and HR run the angular momentum in the outer part of the disk is roughly conserved.

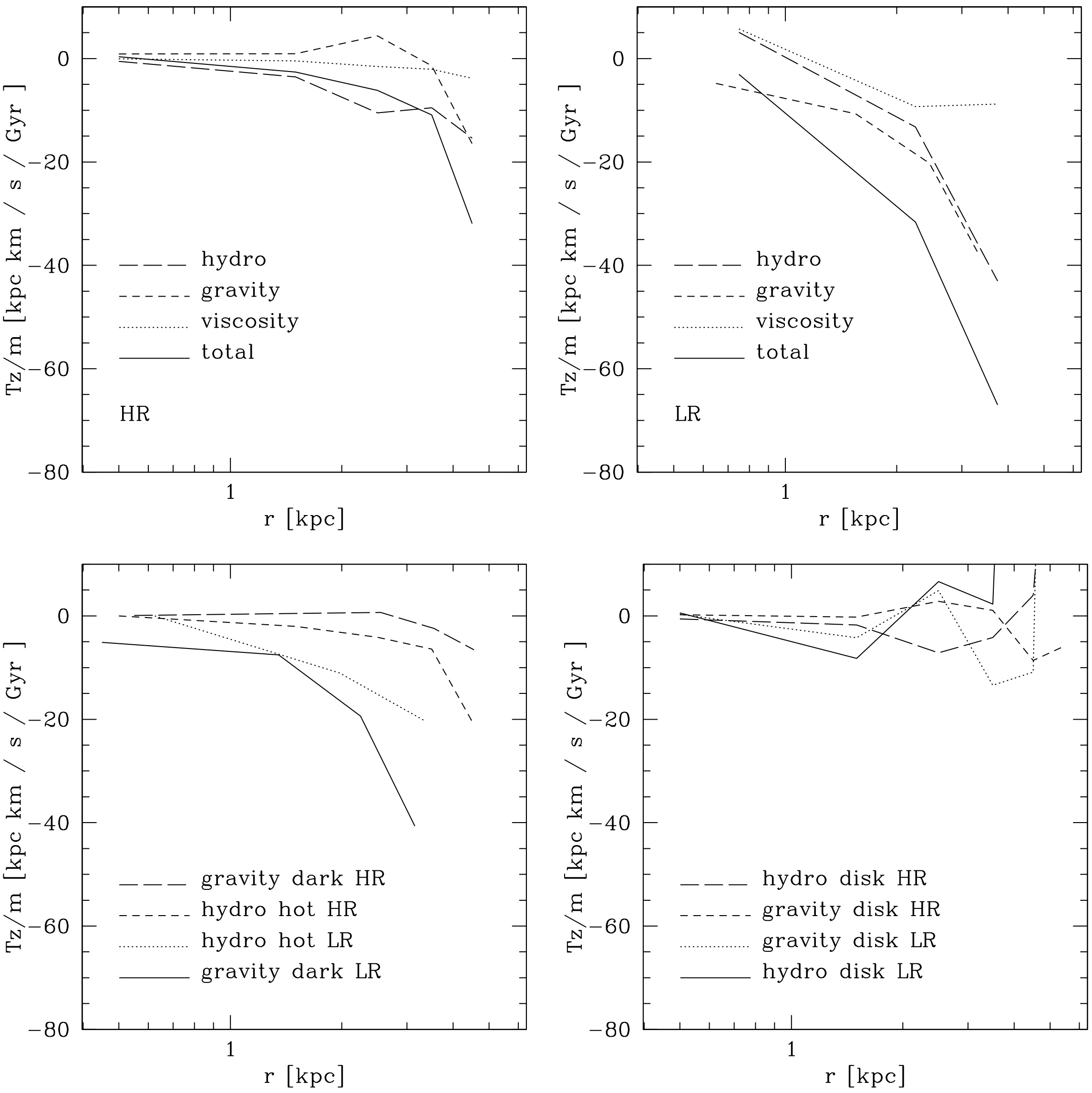

Figure 2.7: Azimuthally averaged specific torques (after 5 Gyr) parallel to the angular momentum of the disk are plotted as functions of radius in the upper panels: hydro torques (long dashed), gravitational torques (dashed), artificial viscosity torques (dotted) and total torques (solid). In the lower left panel we plot the hydro torques between the hot gaseous halo and the cold gas disk: HR (dashed) and LR (dotted). The solid and long-dashed lines show the gravitational torque from the dark halo for the LR and HR simulation, respectively. In the lower right panel we plot the torques from the disk particles acting on themselves: HR (dashed and long-dashed lines are the gravitational and hydro torques, respectively), LR (dotted and solid lines are the gravitational and hydro torques, respectively). In all the plots we find significantly lower torques for the high-res simulation. At high resolution, pressure torques are small but dominate over gravitational and viscous torques.

on disk particles and produced by disk particles themselves. Again at higher resolution the torques are smaller. This reflects also the more axisymmetric disk in the HR simulation. In any case the magnitude of these torques is always smaller than the torques from the halo (both gaseous and dark).

Finally, we also compared the torques coming from artificial viscous forces with the overall hydrodynamical torques. We find that viscous torques are a small fraction of the latter at high resolution, hence torques coming from Okamoto-type pressure gradients dominate. In the past, numerical tests done at lower resolution were finding that artificial viscosity was probably causing most of the angular momentum loss in disks (e.g. Thacker et al. 2000). Our results are not inconsistent, but rather they suggest that by increasing the resolution one progressively enters different regimes in which different numerical effects become dominant.

The results discussed in this section cannot be simply extrapolated to the case of cosmological simulations of galaxy formation because the formation history of a galactic system is more complicated than in the models employed in this chapter. However, the resolution effects that we described certainly do occur in cosmological runs and therefore one has to conclude that those runs are still plagued by numerical loss of angular momentum. This will be particularly severe in the progenitors of the final object, that have fewer particles.

2.4.3 Disk scale-lengths and bar formation

The gravitational softening sets the force resolution in the simulations and particles at scales smaller than the softening will have spurious dynamics. We considered the cases $\epsilon_1 = 0.5$ kpc and $\epsilon_2 = 2$ kpc - the latter typical of that used in cosmological simulations. We found that the choice of the softening heavily affects the morphology of the disk. A small softening allows the formation of a bar in the central object and, afterwards, of spiral structure, while with the larger softening ϵ_2 the disks remain axisymmetric and spiral structure is suppressed. While these differences are not surprising we point out that the bar forms on scales of about 2 kpc, and therefore this is also the characteristic wavelength of these non-axisymmetric modes. If the force resolution is smaller than this wavelength the modes will be damped, as it is the case for the large softening. For the intermediate and high resolution case with the larger softening ϵ_2 we notice that a bar-like feature first appears in the central region (2-3 kpc in size) about 1 Gyr after the beginning of the simulation but then disappears shortly afterwards, see Figure 2.8. We verified that the analytic criterion of disk stability against bar formation of Efstathiou, Lake, & Negroponte (1982) (see also Mayer & Wadsley 2004) is violated in all runs that form a bar. The bar strongly affects the evolution of the radial surface density profile (see Figure 2.9) because it triggers the transport of angular momentum from the inner to the outer part of the galaxy and hence an inflow of mass (see e.g. Mayer & Wadsley 2004 and Debattista et al. 2005). As in the runs with with larger softening we find that the LRLS run does not match the results of the higher resolution simulations, it also produces disks that are too small and have too much mass in the central regions, see Figure 2.9.

Assuming an exponential surface density profile for the cold disk-material Mo, Mao & White (1997) calculated the disk scale-length to be:

$$R_d = \frac{1}{\sqrt{2}} \left(\frac{j_d}{m_d}\right) \lambda r_{vir} f_c^{-0.5} f_R(\lambda, c, m_d, j_d), \tag{2.2}$$

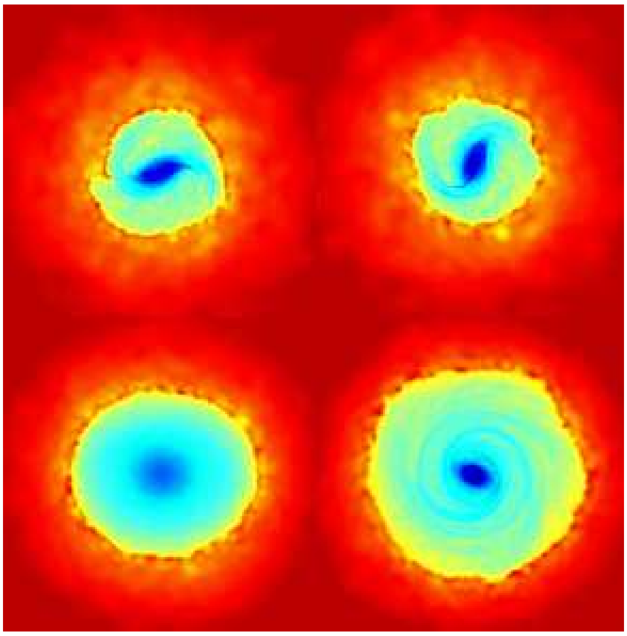

Figure 2.8: Density maps of gas in a slice through the centre of the Milky Way gas disk which show how bar formation can be suppressed by a large softening. On the left the HR run is shown, on the right the HRLS run. Upper panels show a snapshot after 1 Gyr, lower panel one after 5 Gyr. Boxes are 20 kpc on a side. The density is colour coded as in Figure 2.3.

where m_d, j_d are the fraction of the total mass and angular momentum in the disk, respectively, and the functions f_c and f_R take into account the differences to the derivation for an isothermal sphere, see Mo, Mao & White (1997), assuming conservation of angular momentum on all scales and that the gas starts from the same distribution and magnitude of specific angular momentum as the dark matter. The information on the initial angular momentum content is contained in the spin parameter λ. For our simulations we calculated the scale-length $R_d = 3.8$ kpc for $\lambda = 0.038$ (this being the value adopted in our MW model). From the simulations we find $R_d = 1.4$ kpc for the HR run, $R_d = 3.0$ kpc for the outer part of HRLS, and $R_d = 0.8$ kpc for the LR run. We find that the gas which settles into the disk after 5 Gyr is cooling inside a sphere with maximum"cooling radius" $r_c = 70$ kpc in, for example, run HR. Although one could associate r_{vir} with r_c, thereby matching the scale length for HR, the results of HRLS (here the central bar increases the scale-length of the outer part due to the transport of angular momentum) support the Mo, Mao & White formula. Clearly the measured disk scale lengths depend sensitively on the force and mass resolution and the comparison with analytical models remains difficult.

2.5 Stellar versus gaseous disk formation

In reality star formation will occur in a galactic disk as soon as it begins to assemble. In fact in absence of the heating provided by feedback from star formation the gas layer will rapidly become gravitationally unstable, dense molecular gas will form efficiently and will collapse into star clusters. We performed some additional runs with star formation.

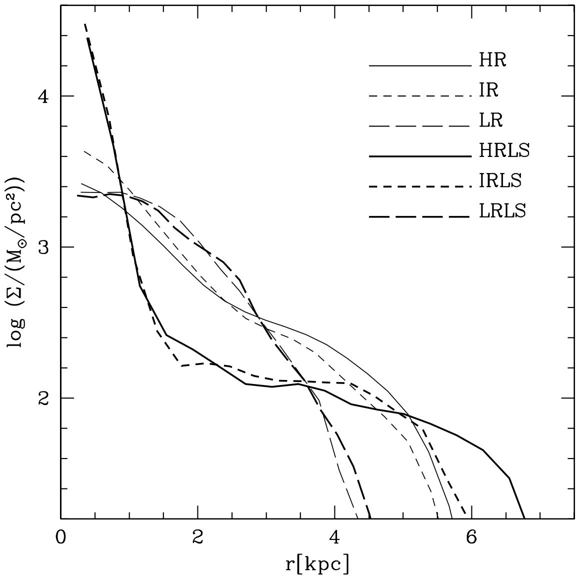

Figure 2.9: The surface density of the gas disks after 5 Gyr. For small softening the Milky Way model developed a bar which increases the central surface density, therefore an exponential profile can not fit these models.

These runs will also be used to isolate more clearly that component of spurious angular momentum loss and of other numerical artifacts that is related only to the SPH modeling of gas physics since if the gas in the disk is quickly turned into stars it will interact with the rest of the system only via gravity. Among the star formation prescriptions that we have adopted, some are not meant to be realistic but are just designed to test such numerical issues. Unless stated otherwise these tests have been run with the Milky Way model at intermediate resolution (IR). We began by using a star formation recipe similar to that described in Katz (1992); stars spawn from cold, Jeans unstable gas particles in regions of converging flows. The mass of gas particles decreases gradually as they spawn more star particles. After its mass has decreased below 10% of its initial value the gas particle is removed and its mass is re-allocated among the neighbouring gas particles. Up to six star particles are then created for each gas particle in the disk. Note that once a gas particle is eligible for spawning stars, it will do so based on a probability distribution function. The star formation rate is 4.5 $M_{\odot} yr^{-1}$ (time-averaged over 5 Gyr) in the run adopting this recipe and the resulting disk mass is very close to that of the disk in the corresponding run without star formation (see Figure 2.12). Moreover, similarly to the purely gas dynamical runs, a bar forms provided that the force resolution is high enough. Therefore the stability properties of the disk seem essentially independent to its collisionless or dissipational nature, probably because the disk is massive enough to make velocity dispersion or disk temperature factors of secondary importance (Mayer & Wadsley 2004). Also the stellar surface densities are close to those of the gas runs, as shown in Figure 2.10.

We then explored a second star formation recipe in which whenever a gas particle satisfies the relevant criteria (i.e it is in a convergent flow, the condition of local Jeans

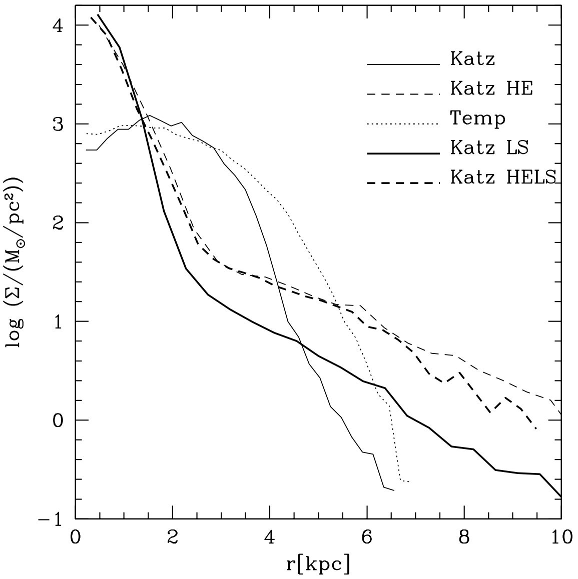

Figure 2.10: The surface density of the stellar disk after 5 Gyr for IR resolution (see table 2.1, LS is referring to 0.5 kpc softening, the other runs use 2 kpc). For small softening, the Milky Way model developed a bar which increases the central surface density. This bar is only resolved with small softening.

instability is satisfied and the temperature is lower than 30,000 K) is immediately turned into a single star particle of the same mass. In this way the efficiency of star formation is much higher than in the standard scheme. We refer to this model as Katz HE. The star formation rate is slightly higher here (5 $M_{\odot}yr^{-1}$) (time-averaged over 5 Gyr), but the initial star formation rate was much higher, 11.1 $M_{\odot}yr^{-1}$ time-averaged over the first 0.5 Gyr, compared to 4.0 $M_{\odot}yr^{-1}$ for the first model during the same time. The gaseous disk soon becomes mostly stellar ($M_{gasdisk}/M_{disk}$ ≈ 0.15 after 5 Gyr). The massive and dense stellar disk that forms so early produces a particularly strong and long bar that this time is not suppressed even with a softening of 2 kpc (see Fig. 2.11). Other than this, most of the properties of this simulation are similar to those of others, including the total accreted disk mass.

To separate the gravitational and hydrodynamical aspects of disk formation as cleanly as possible we used a third star formation recipe which is based only on a temperature criterion (this run is indicated as SFT and was carried out at HR resolution). As soon as a gas particle becomes colder than $30,000$ K it is immediately turned into a star particle. The resulting star formation rate is much higher than star formation rates in disk galaxies, and is essentially equal to the mass deposition rate in the cold phase, ($\sim$ 6.3 $M_{\odot}yr^{-1}$ is the time-averaged value over 5 Gyr). In this run there is never a cold gaseous disk, instead a purely stellar disk forms as soon as gas particles cool down. This means that, by construction, there are no torques between a hot and a cold phase. The disk has a bar when the softening is small (0.5 kpc). The disk of the high resolution run HRSFT accumulates $\sim$ 7% more angular momentum after 5 Gyr compared to the corresponding run with no star formation HR (see Figure 2.12). However, the two runs differ significantly

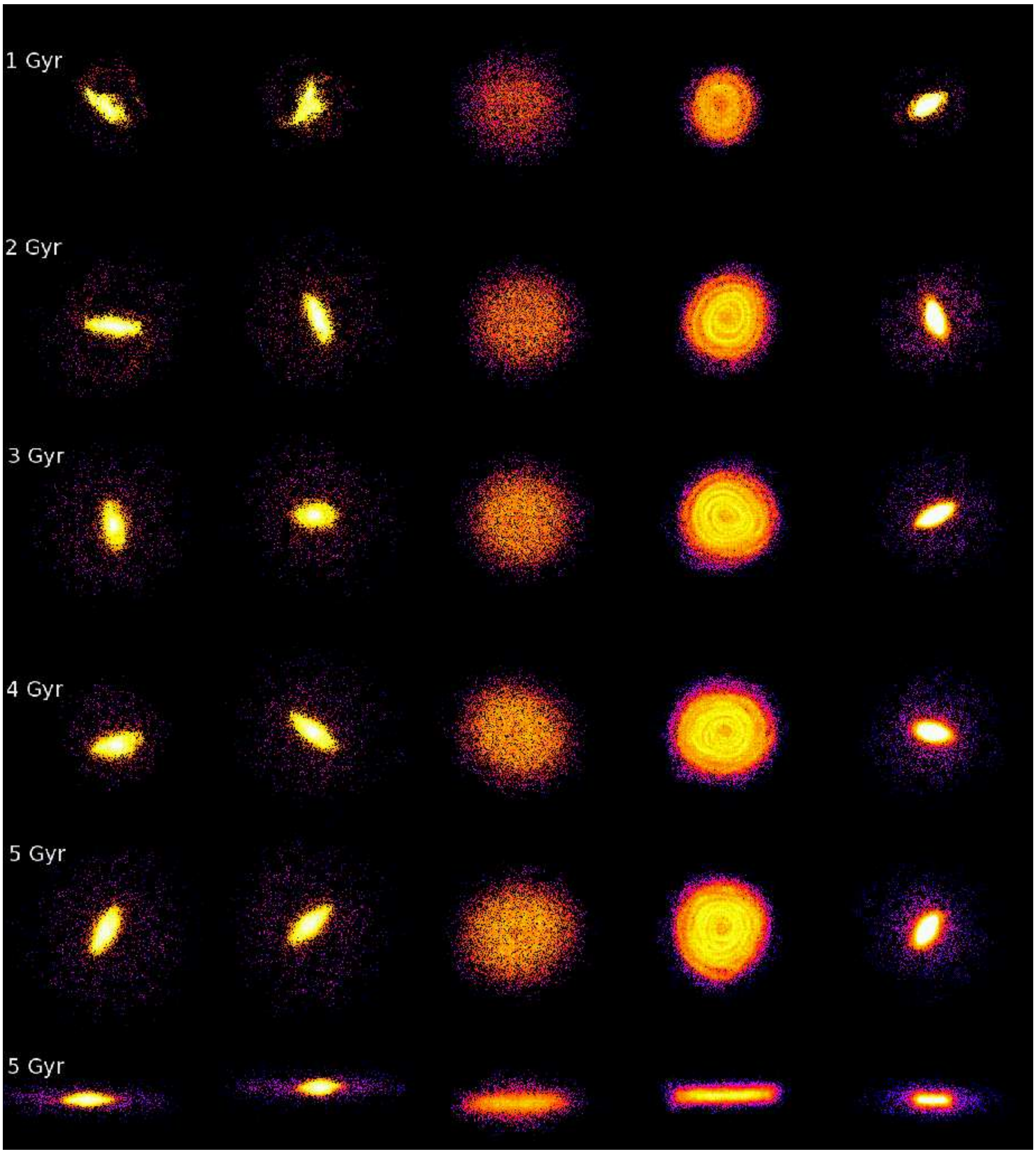

Figure 2.11: Colour coded density maps of the distribution of stars - each column is a different star formation recipe and/or softening. Column 1 and 2 show the runs with the high efficient, Katz-type star formation recipe (Katz HE, see Table 1 and 3), while column 4 and 5 use the standard Katz star formation recipe (see Table 1 and 3). In column 3 the star formation was based only on a temperature criterion (runs with extension "SFT" in Table 1 and 3). Boxes are 16 kpc on a side for each individual snapshot. In all the runs with small softening (second and last column) the bar-instability was resolved. The final row shows the end state seen edge on.

because the run with star formation never forms a bar (this recipe produces a relatively thick disk which has a higher Q parameter) while the HR run has a transient bar instability between 0.5 and 2 Gyr (both runs have large softening). Interestingly, the difference in the final angular momentum content of the disks seems to arise during the period in which run HR forms a transient bar (as shown by the inset plot in Figure 2.12) transferring angular momentum to the halo. Indeed if we compare the angular momentum evolution between the two runs after ≈ 2 Gyr, when also the HR run has formed a stable disk, they appear virtually identical. We argue that this shows that at high resolution the artificial hydro torques between the hot and cold phase are small, and hence any eventual loss of the disk is dominated by gravitational torques (torques from artificial viscosity are even less important as we have shown previously). These results support the analysis carried out in section 3.2.

2.6 Dependence on the Initial Conditions

2.6.1 Influence of the temperature floor on the gravitational stability

We adopted a standard cooling function for a gas of primordial composition (hydrogen and helium in atomic form) including radiative cooling which is very efficient above temperatures $10,000$ K (molecular cooling is not included). The central gas quickly cools down to either this limit or whatever temperature floor we impose. In all the models without a temperature floor in the cooling function the disk becomes gravitationally unstable after a couple of Gyr and widespread fragmentation into dense clumps occurs. A way to quantify the stability of a gas disk is the Toomre parameter (Toomre, 1964).

$$Q(r) = \frac{v_s \kappa}{\pi G \Sigma}, \tag{2.3}$$

where $\kappa^2(R) = R\frac{d\Omega^2}{dR} + 4\Omega^2$ is the local epicyclic frequency, v_s is the local sound-speed and Σ is the surface density of the gas. For a razor-thin gaseous disk, stability against all axisymmetric perturbations requires $Q > 1$. The disks fragment because Q drops to less than unity almost everywhere in the disk shortly after formation.

To prevent these instabilities we set a minimum temperature that the gas can reach by cooling. In reality heating from stellar feedback (stellar winds and supernovae explosions) will provide a way to maintain the effective temperature of the disk above $10,000$ K (between $15,000$ and $30,000$ K depending on the run). Evidence of this is the existence of a multi-phase structure in the interstellar medium, which includes a cold, a warm and a hot phase (McKee & Ostriker 1977), and the fact that even the coldest phase, i.e. molecular gas, has significant turbulent motions which creates an effective pressure that is higher than the thermal pressure. Because $v_s \propto \sqrt{T}$, the Toomre parameter increases when we enforce such a temperature floor, see Figure 4.8. As a result, in the run HR a fairly axisymmetric disk galaxy formed which did not fragment. Romeo (1994) has emphasized the role of a finite disk thickness in the context of stability; for a thick gas disk, the effective critical value of Q is lowered down from 1 to ≈ 0.6, ; the HR run and the HR run without a temperature floor, have typical values of Q that are below 1 but, respectively, above and below 0.6, thus explaining why one fragments and the other does not. However, also the softening parameter affects stability (Romeo 1994) unless the disk scale-height is significantly larger than the softening. When the softening is important for the stability

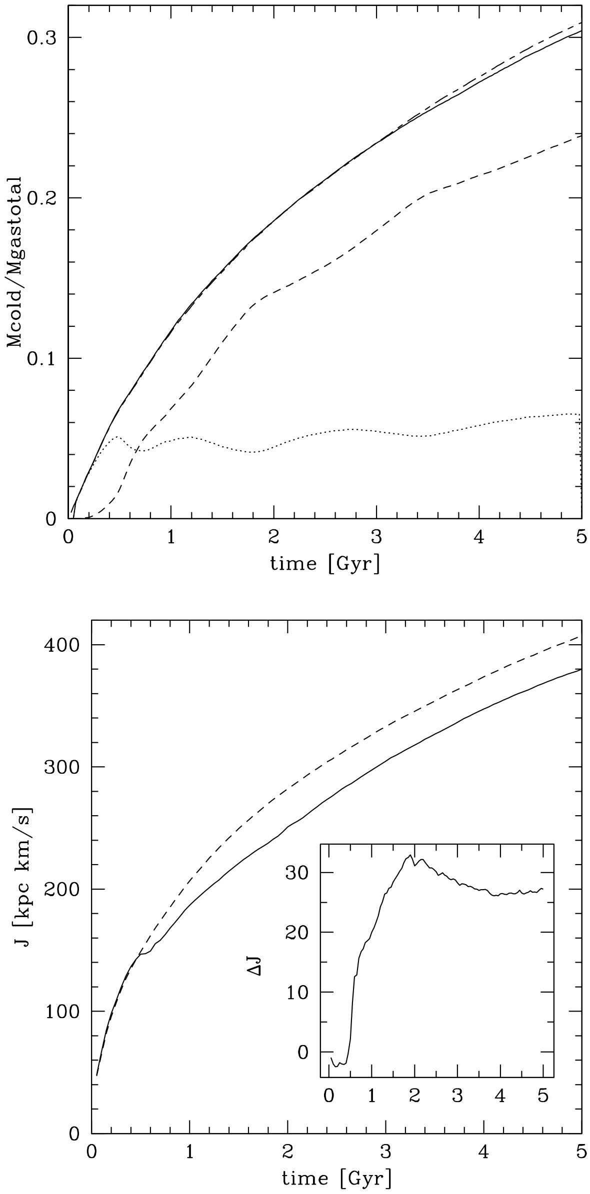

Figure 2.12: Angular momentum and mass accretion in the simulations including star formation and run with low softening: In the left panel we plot the mass accretion of the disk particles of the star formation run with the Katz recipe (dashed stars, solid baryons and dotted gas) and long-dashed-short-dashed the corresponding gas run IRLS: the accreted baryonic mass in the disk remained the same. The right panel shows the specific angular momentum evolution of the disk particles of the HRSFT star formation run (dashed) and the corresponding high-res gas run HR (solid line). In the inset the difference in angular momentum between these runs is plotted. The amount of angular momentum accreted by the disk in the star formation run was slightly larger compared to the purely gasdynamical run, but see text for the details.

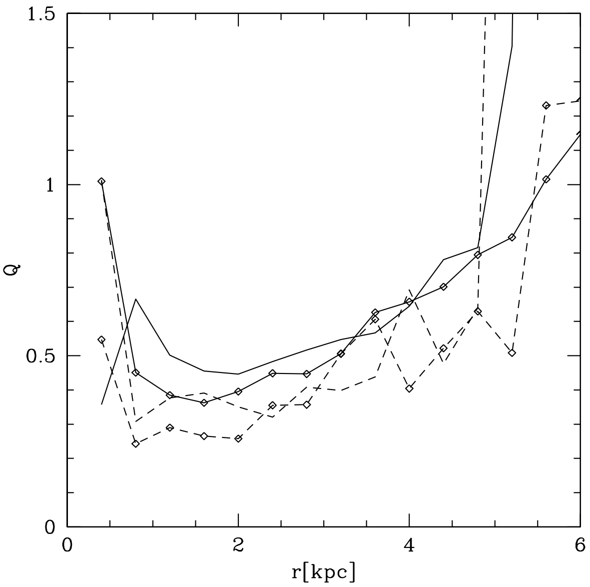

Figure 2.13: Plot of Toomre parameter Q for the high-res model with (HR, solid lines) and without (dashed lines) a temperature floor in the cooling function. The lines with open symbols are after 6 Gyr whereas the other lines are after 2 Gyr. As expected, Q increases if ones uses a temperature floor.

(which applies to our simulations) a cold stellar disk is stable as long as

$$s > s_{crit} = \frac{1}{e}\frac{2\pi G\Sigma}{\kappa^2}, \tag{2.4}$$

where s is the plummer softening (which is of the order twice the corresponding spline softening used in GASOLINE); this result was also generalised for a gaseous disk. Measuring s_{crit} in the simulations showed that only for LS runs ($\epsilon = 0.5$ kpc) the softening is clearly smaller than this critical value. Although Romeo's results were derived for only gravitational forces, this suggests nevertheless that the stability level of our cold gas disk is not simply controlled by the physical properties which determine $Q(r)$, but is also heavily influenced by the choice of the softening parameter. Fragmentation and instabilities are suppressed by the softening, which acts as an artificial pressure at small scales (Bate & Burkert 1997). This conclusion supports the strong dependence of the bar instability from the choice of the softening.

2.6.2 Generating initial conditions using a merger

In the ΛCDM model a galaxy like the Milky Way forms after a series of mergers. Typically one last major merger between two or more massive progenitors builds up most of the mass of the final system, including most of the gas that will later collapse and form a rotating disk (e.g. Governato et al. 2004; Sommer-Larsen et al. 2003). To bring a greater degree of realism to our initial conditions we construct an equilibrium triaxial halo in which the gas acquires its angular momentum through an equal mass merger (see Moore et al. 2004). We start with two spherical, non-rotating NFW haloes each with half of the mass of the

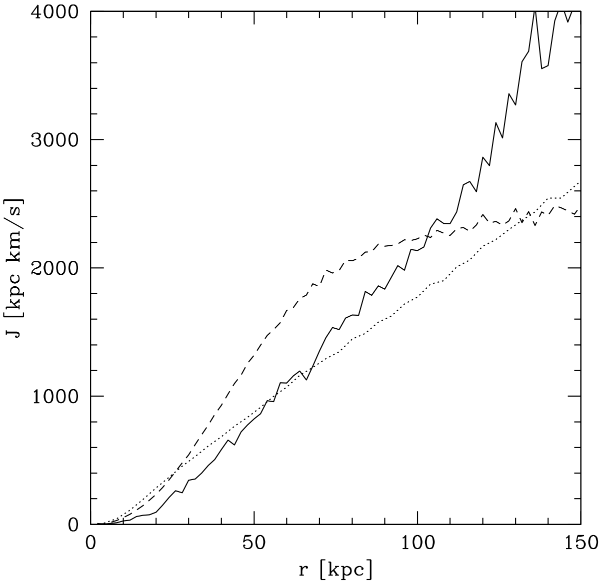

Figure 2.14: The specific angular momentum profile after the merger: dark matter (solid lines) and gas (dashed lines). The dotted line show the specific angular momentum profile of the gas from the spherical MW model used previously.

MW model considered previously. The two haloes are placed at a separation of twice their virial radius. One of them is given a transverse velocity of 35 km/s, and then the haloes are allowed to merge. This net velocity (determined using a trial-and-error procedure) results in a final gas distribution that has a similar spin parameter as used previously. The triaxial halo resulting after the merger, consisting of 9×10^5 dark matter and 10^5 gas particles, was first evolved for 20 Gyr with an adiabatic equation of state for the gas (softening parameter of 0.5 kpc). The final spin parameter inside the virial radius was $\lambda = 0.044$ and the resulting specific angular momentum profile had a slope that depends on radius, going from $J \propto r^{1.0}$ to $J \propto r^{0.5}$ (see Figure 4.1). The inner part of the dark halo was significantly oblate, $c/a \approx 0.57$, and the angular momentum was aligned along the short axis. This system was then evolved for 5 Gyr with radiative cooling. A disk with a bar formed, with the final cold gas mass being comparable to the other Milky Way models. However, owing to the shallower inner slope of the angular momentum profile (and the slightly higher spin parameter) the final disk angular momentum was $\approx 30\%$ higher than in the corresponding standard run at the same resolution (the IRLS run). The disk radius reached 8.4 kpc after 5 Gyr. The structure of the disk in this merger simulation is very similar to that of the disks in the standard simulations (see Figure 2.15). The model violated also the criterion of disk stability against bar formation of Efstathiou, Lake, & Negroponte, but the bar instability was delayed compared to the IRLS run; the bar appeared after about 2 Gyr instead of after just 1 Gyr, probably because the higher angular momentum near the center of the system slowed down the build up of a dense, unstable inner disk. After 2 Gyr the cooling of baryons made the halo rounder (see Kazantzidis et al. 2004); the bar formed at a time when c/a of the dark halo was already ≈ 0.8.

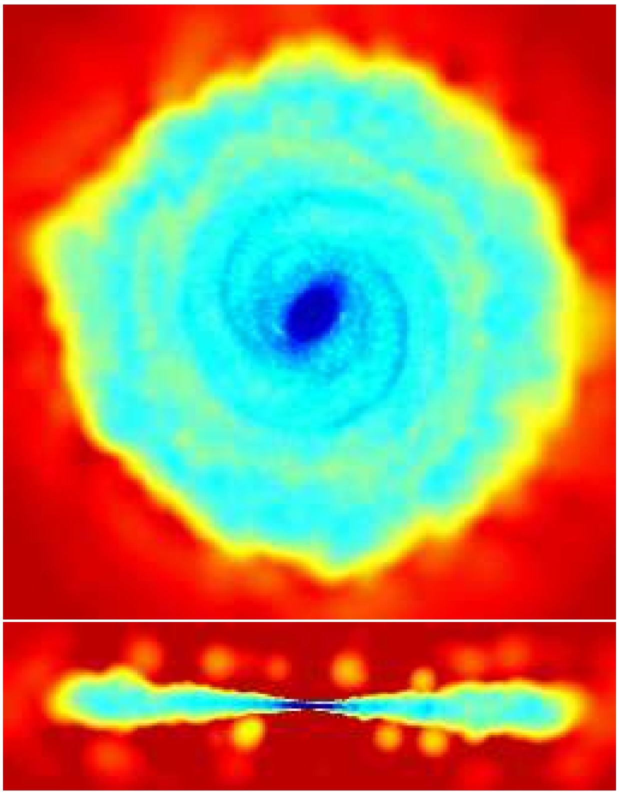

Figure 2.15: Density maps of gas resulting from the triaxial initial conditions in a slice through the centre of the gas disk after 5 Gyr, face-on and head-on. The main box is 20 kpc on a side. The density is colour coded as in Figure 2.3. The merger model produced a disk remarkable similar to that in the standard spherical halo models.

2.6.3 Different Initial Angular Momentum Profiles

As we have seen in the previous section, there are natural ways in which the initial gaseous angular momentum profile might differ from the simple power law as suggested by Bullock et al. (2001b). Therefore we decided to explore further the effect of changing the initial angular momentum profile. To this aim we ran an additional simulation with the M33 model. Here we compare runs using two different initial conditions, one with $J \propto r^{1.0}$ and one with $J \propto r^{0.5}$, named respectively, M33A and M33B. Let us first describe the results of the various runs performed at different resolutions with model model M33A. After 1 Gyr of evolution the surface density profiles of the standard resolution run and of the higher resolution, refined run with particle splitting (see Kaufmann et al. 2006a for the latter) look similar, except that the steepening of the slope towards the center is slightly more pronounced in the run with splitting, possibly as a result of a more intense mass inflow driven by spiral arms. After four Gyr the disk of M33A attains a near exponential surface density profile over a large fraction of its extent, except within a few hundred parsecs from the center, where a dense nucleus produces a central spike in the profile. Model M33B also shows a spike in the center, and the density in the outer region does not decrease monotonically but has a bump (see Figure 2.16). The density in the central part is one order of a magnitude smaller and the size of the cold gas disk is larger; its radius after 4.75 Gyr is 12.7 kpc for M33A and 19 kpc for M33B, see Figure 2.17. These differences are expected because there was initially more angular momentum in the inner part of the halo of model M33B, and this produced a more extended disk. The material in the central spike is accreted gradually over time and comes from a cylindrical region which extends above and below the disk. After 4.5 Gyr it has a mass of $\sim 10^8 M_\odot$, $\sim 1\%$ of the total disk mass for model M33A. The inner nuclear region is poorly resolved with our standard force resolution, therefore we repeated run M33A with a softening of 50 pc. The nucleus formed in a similar way, and its radius shrank slightly, becoming again comparable to the force resolution. This suggests the inflow will continue to even smaller scales (unless stopped by an opposing pressure force produced by some heating source) if we had higher resolution. Artificial loss of angular momentum driven by artificial viscosity is another aspect to consider. We tested its role by decreasing the coefficients of viscosity. We run again using $\alpha = 0.5$ and $\beta = 0$ (strong shocks are not expected in the disk) instead of the standard values $\alpha = 1$ and $\beta = 2$, and found that neither the nucleus nor the appearance and size of the disk is affected by lowering the artificial viscosity. In summary, in no simulation using the M33 model were we able to produce a pure exponential profile without a nuclear density enhancement.

The M33 model represents a more ideal case than the MW models to address the issue of disk profiles because there are no strong morphological changes induced by bar formation (which will transport angular momentum) as in the MW models. Van den Bosch (2001) assumed detailed angular momentum conservation to follow the collapse of spinning gas and the resulting formation of a disk inside an NFW halo with a semi-analytical code. His models did not produce disks with exponential profiles, contrary to the assumption of the Mo, Mao & White (1998) model. Instead power law profiles with steeper slopes near the center were the typical outcome; those steep inner slopes agree with our simulations. However, the reason behind the steeper central slope is not necessarily the same in that work and in our work, and so the agreement is likely coincidental.

While the lower angular momentum material collapsing rapidly and efficiently near

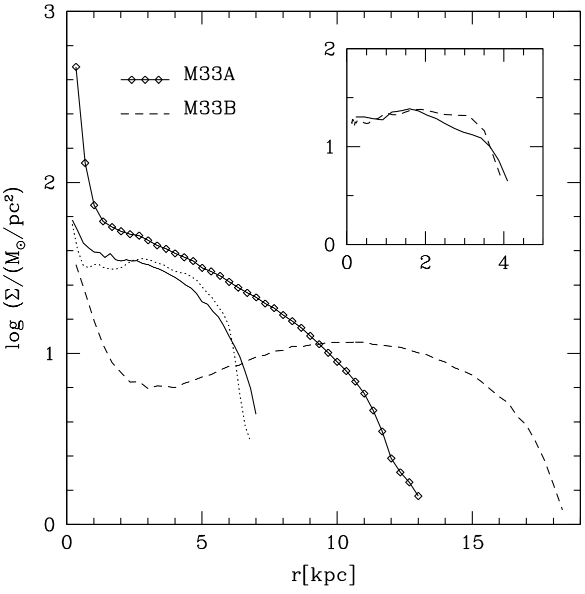

Figure 2.16: The logarithmic surface density of the M33 gas disk after four Gyr for different models: M33A (solid with open symbols), M33B (dashed line). The solid line shows M33A after one Gyr and the dotted line shows the refined model of M33A at the same time. Inset: logarithmic surface density of the standard and refined M33A (solid and dashed, respectively) run after 0.25 Gyr. All the M33 models showed at later stages a nucleus in the centre.

the center of a cuspy NFW halo was the only cause in Van den Bosch (2001), here it seems that angular momentum transport driven by spiral instabilities is associated with the appearance of the nucleus and the associated non-exponential profile (effects of self-gravity are of course not included in the semi-analytical models). Does this mean that an exponential profile would result in our simulations if the disk was perfectly axisymmetric and smooth? We defer this important question to a future paper which will focus on the origin of exponential profiles. For the moment we note that the angular momentum distribution in our simulations is not fixed in time as in Van den Bosch (2001) but changes continously due to a combination of numerical and physical processes depending on the force and mass resolution. This suggests that it would not be surprising if the resulting profiles would be different from those calculated analytically even in absence of spiral instabilities.

2.7 Summary and Discussion

We simulated the formation of galactic disks in cuspy dark matter haloes to explore numerical effects and physical processes that take place during the late stages of disk formation. We studied the effects of initial angular momentum distribution, force and mass resolution, halo triaxiality, star formation and artificial viscosity. Our results show that the large angular momentum losses reported in some early works, including cosmological simulations, were primarily due to insufficient mass resolution. While convergence in disk

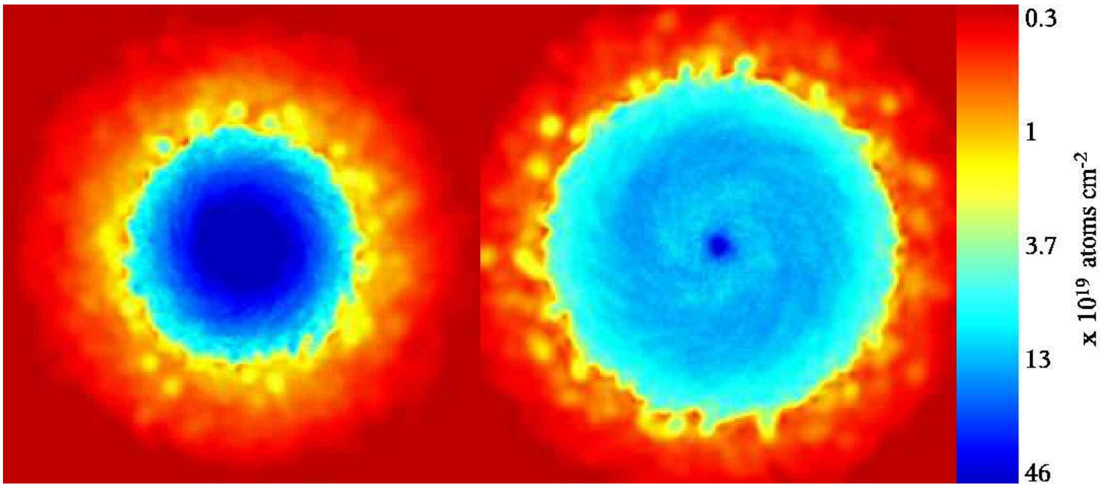

Figure 2.17: The panels show density maps of gas in a slice through the centre of the M33 gas disk after 4 Gyr, for M33A (left) and M33B (right). Boxes are 50 kpc on a side in both panels. The nucleus and the spiral arms are visible in both models.

mass is reached with $\sim 10^4$ particles, disk sizes and angular momentum of the disk do not converge even at the highest resolution used in this work ($\sim 10^6$ particles) We studied the different numerical and physical mechanisms by which disk particles can lose angular momentum. In summary we found the following results:

- Gas particles which will end up in the disk can lose angular momentum while falling to the disk in the hot phase. This effect depends on resolution: the low-res run loses twice as much as the hi-res via this mechanism.

- Cold particles belonging to the disk transfer angular momentum to the hot gaseous halo, via both hydrodynamical and gravitational torques. The magnitude of these torques is comparable but depends strongly on resolution (torques are reduced by about a factor of 4 for an increase in resolution of more than an order of magnitude).

- At high resolution ($N > 10^5$) the loss of angular momentum due to spurious hydrodynamical torques between the cold gas disk and the hot gas halo seems to play a secondary role. In fact hi-res runs in which the hydrodynamical interaction between the cold and hot phase is absent (where the cold gas particles are readily turned into collisionless stellar particles) show an angular momentum evolution similar to that of the corresponding runs without star formation. This suggests that at high resolution the angular momentum transport from the disk is mostly gravitational in origin and most of the hydrodynamical angular momentum transport is occurring before the particles reach the disk (the latter is not included in our measurement of the torques). Gravitational torques are probably caused by the fact that both the halo and disk have asymmetries in their mass distribution which are caused in part by the initial noise in the halo models and in part arise as a result of evolution. In fact we find that gravitational torques are particularly strong where the disk develops non-axisymmetric features like spiral arms.

- Small losses of angular momentum by artificial viscous torques certainly occur, but at high resolution they yield the smallest contribution to hydrodynamical torques, which are dominated by those produced by spurious pressure gradients. These pressure torques could be associated with small lumps in the cold disk being dragged by the hot background medium.

- Gas particles within the inner kpc transfer away nearly all of their initial angular momentum. This is a physical transport that depend on the strength of the spiral patterns and bar, which in turn depends on the gravitational force softening.

We found in our high-res runs that the gas particles which cool to the disk, lose overall $\sim 20\%$ of their specific angular momentum while cooling as a result of the combination of the various effects mentioned. The situation in cosmological simulations can only be worse since even fairly massive progenitors of a Milky Way-size object have resolutions comparable to the lowest used in our work. Therefore numerical loss of angular momentum in the early stages of galaxy formation will be severe (larger than 50% based on our results). This could explain the excess of low angular momentum material always present in simulated galaxies in the form of a slowly rotating, central bulge-like component; this forms typically only after a few billion years from the merging of two or more massive progenitors and is too concentrated and massive compared to bulges of late-type spirals (Governato et al. 2004). This behaviour stands in contrast to several semi-analytical models which suppose strict angular momentum conservation while gas particles cool.

One is tempted to conclude that in cosmological simulations a regime with negligible numerical loss will be hard to reach due to the nature of hierarchical structure formation. Even very well resolved objects at the present day will host some baryonic component that was assembled earlier in poorly resolved objects. Some help comes from the fact that baryons would not collapse in structures below $10^9 M_\odot$ or so due to the effect of reionisation – if these are the first objects that we need to resolve well enough to have negligible artificial angular momentum loss it means that the SPH particles mass has to be of order a few thousand solar masses, which implies $> 10^7$ SPH particles will be required inside a final Milky-Way sized system. Although such a number of SPH particles is still beyond current capabilities, improvement in both software and hardware will make this possible in the near future. It is interesting to note that a similarly high number of particles has been necessary in the past to completely control artifacts present in the dark matter component of simulations such as the overmerging of substructure (Ghigna et al. 2000).

In this work we also studied the morphology of the simulated galaxies. Bar formation should be a very common process for galaxies with masses comparable to the Milky Way: independent of the mass resolution and of the use of the Katz-type star formation recipe, all the disks went bar unstable as soon as the force resolution reached 0.5 kpc or $\sim 0.25\%$ of r_{vir}. Bars efficiently transport angular momentum towards the outer disk, which increases its scale length by up to a factor of 2. This is an important effect to take into account in order to explain observed galaxy sizes (see also Debattista et al. 2005). The formation of a strong bar in the runs with star formation is clearly correlated with how quickly the disk attains a high enough mass.

None of the runs, either Milky Way-like or M33-like, produced a purely exponential disk at high resolution. In the runs with the Milky Way model a bar forms and with that a bimodal profile with a nearly exponential outer disk and an inner bulge-like component with a much steeper profile. In the runs using an M33-like model a bar does not appear due to the low baryon fraction (and resulting much lighter disk) but a power law-type profile arises which strongly deviates from exponential in the central region. The steep central profile is associated with a dense nucleus. The nucleus is formed with particles that lose most of their angular momentum, we believe as a result of transport by spiral arms. Although the formation of the nucleus persisted even in a run where the mass resolution, thanks to particle splitting, was ten times better than the standard hi-res runs, we cannot exclude that it is produced by a numerical artifact.

The relationship between the non-exponential profiles seen in our work and the very similar power law profiles predicted by semi-analytical models of galaxy formation (e.g. Van den Bosch 2001) is still to be understood. The comparison between the semi-analytical models and the simulations is not straightforward, because the latter include self-gravity, and thus non-axisymmetric modes. Basic differences between the semi-analytic models and simulations still exist. For example the gas does not cool onto the disk in a spherical cooling flow, rather from a cylindrical region which extends above and below the disk.

It is tempting to associate the nucleus to the central dense stellar nuclei seen in several late-type spiral galaxies, i.e. in the limit of infinite resolution then some transport of angular momentum remains which causes gas to quickly reach the central dark matter cusp. Indeed the scale and corresponding overdensity of such a nucleus in the simulation is comparable to that seen, for example, in M33 (Regan & Vogel 1994). M33 is not unique in this sense since similar nuclear components with a range of sizes and luminosities are found in many late-type spirals (Carollo et al. 1998, Carollo 1999). We verified that the surface density profiles and stellar nucleus are essentially unchanged when we allow gas to be turned into stars. Our next step is to extend the cooling function to metals and molecules and include heating from supernovae winds and radiation backgrounds. One could imagine that feedback may cause a large fraction of the low angular momentum material of the inner nucleus to be removed, helping to produce a disk with exponential profile.

Acknowledgments

We would like to thank Stelios Kazantzidis for providing a code to generate isolated dark matter haloes. We acknowledge useful and stimulating discussions with Chiara Mastropietro, Frank van den Bosch, Aaron Dutton, Tom Quinn, Victor Debattista, Steen Hansen & Fabio Governato. The numerical simulations were performed on the zBox (http://krone.physik.unizh.ch/∼stadel/zBox) supercomputer at the University of Zürich.

Chapter 3

Cooling flows within galactic haloes: the kinematics and properties of infalling multi-phase gas [2]

3.1 Abstract

We study the formation of disks via the cooling flow of gas within galactic haloes using smoothed particle hydrodynamics simulations. These simulations resolve mass scales of a few thousand solar masses in the gas component for the first time. Thermal instabilities result in the formation of numerous warm clouds that are pressure confined by the hot ambient halo gas. The clouds fall slowly onto the disk through non-spherical accretion from material flowing preferentially down the angular momentum axis. The rotational velocity of the infalling cold gas decreases as a function of height above the disk, closely resembling that of the extra-planar gas recently observed around the spiral galaxy NGC 891.

3.2 Introduction

Galaxy formation is a complex process involving the simultaneous action of many physical mechanisms. Even though we have a well defined cosmological framework, ΛCDM, within which to study galaxy formation, numerical simulations have achieved limited success as far as reproducing the structural properties of observed galaxies. Such simulations give rise to disks that are smaller and denser than their observed counterparts (e.g. Navarro & Benz 1991, Katz et al. 1992, Navarro & Steinmetz 2000). A further problem is the difficulty in producing disk dominated systems, even when haloes with quiet merger histories are selected. These problems may be due to the lack of a correct treatment of the physics of the multiphase interstellar medium, in particular of the balance between radiative cooling and heating from various forms of feedback arising from star formation (White & Frenk 1991, Navarro & Benz 1991, Katz et al. 1992, Robertson et al. 2004). However, limitations

---

[2] This chapter is published in: MNRAS, 2006, 370, 1612 (Kaufmann et al. 2006a).

in the numerical models, for example the coarse mass and force resolution, are perhaps another major cause of the problem (Governato et al. 2004).

In this chapter we use new N-Body+SPH simulations where we achieve a resolution in the gas component of $730 M_\odot$, in order to follow the formation of a galactic disk via the cooling of gas within equilibrium dark matter haloes. Cosmological simulations suggest that the large disks of spiral galaxies form mainly from the smooth accretion of gas after the last major merger (Sommer-Larsen, Götz & Portinari 2003, Abadi et al. 2003, Governato et al. 2004). Therefore, although our simulations are not within the full cosmological framework, they are designed to follow the quiet gas accretion phase during the main epoch of disk formation. This allows us to resolve the cooling flow of gas at a very high resolution, which complements studies of disk formation within cosmological simulations.

The hierarchical formation of massive dark matter haloes, above a characteristic circular velocity of 120 km/s is expected to efficiently shock heat the gas to their virial temperatures throughout the virial region (Dekel & Birnboim 2004, McCarthy et al. 2003). Angular momentum of the gas and dark matter is generated early by tidal torques, allowing it to cool and form a rotationally supported disk (Crampin & Hoyle 1964). The process of gas cooling from the halo into the disk is difficult to study observationally and little evidence for gas accretion is observed in galaxies or cluster mass haloes. Cooling flow clusters are so named because of the observed decrease in the central temperature of the gas. In galactic haloes the gas temperature can be lower than 10^6 K and thus difficult to observe by current X-ray telescopes (Benson et al. 2000), but there is evidence for a hot ionised corona surrounding the Milky Way.

Recent measurements of OVI and OVII absorption in the UV and X-ray part of the spectrum (Sembach et al. 2003) lend support to the idea that a lumpy gaseous Galactic halo exists and that such emission comes from the interface between warm clouds and the hotter diffuse medium. Maller & Bullock (2004) suggested that the gas supply to galaxies is mostly in the form of discrete warm clouds. Small density and temperature fluctuations are enhanced by the cooling process resulting in a runaway instability and the formation of a fragmented distribution of cooled material, in the form of warm ($\sim 10^4$K) clouds, pressure-supported within the hot gaseous background. This model may explain the properties of high velocity clouds (HVCs) around the Milky Way (Blitz et al. 1999), for example their radial velocity distribution and angular sizes.

Recently, Fraternali et al. (2004) measured the rotation curve of extra-planar neutral gas around the large spiral galaxy NGC 891. This gas could be accreting material or gas falling back to the disk via a galactic fountain from star-formation. The thermal instability mentioned above results in cloud masses that are predicted to be $\sim 10^6 M_\odot$ which is an order of magnitude below the minimum mass resolved in the SPH calculation in current state-of-the art galaxy formation simulations (e.g. Governato et al. 2004). In this chapter we aim to have sufficient resolution to study the formation of a two-phase medium which will allow us to compare the kinematics of the gas with the observations of Fraternali et al.

The plan of this chapter is as follows: In Section 3.2 we present the modeling of our haloes, the treatment of the cooling and the numerical techniques. In Section 3.3 we compare the kinematics of the gas and the disk with the observational data from Fraternali et al. The properties of the cool clouds are studied in Section 3.4, including survival times, mass function and numerical convergence studies. We conclude and summarise in section 3.5.

3.3 Initial Conditions and Methods

We set up a spherical equilibrium halo with an NFW profile (Navarro, Frenk & White 1996) and structural parameters consistent with predictions of the standard ΛCDM model (Kazantzidis, Magorrian & Moore 2004). We include a fraction of the total halo mass, f_b, as a hot baryonic component with the same radial distribution and a temperature profile such that the gas is initially in hydrostatic equilibrium for an adiabatic equation of state (EOS) for the gas. Of course this kind of setup can not model galaxy formation in general (no substructure, no counter rotation etc.) but should reproduce the late phase accretion after the last major merger. To illustrate the initial conditions we plot the initial particle distribution and the density profiles in Figure 3.1. The shape for the initial density of gas and dark matter is the same whereas only the normalisation is different. The curves after 0.5 Gyr show that the hot halo evolves out of equilibrium when using cooling, the density of the dark matter after 0.5 Gyr is enhanced in the centre due to adiabatic contraction.

The dark matter haloes are constructed using a multi-mass technique such that the innermost region is very well resolved. For the M33 "standard" model (see below) we use $1,400,000$ particles distributed in the inner sphere of radius 20 kpc, then $600,000$ particles in the next shell to 100 kpc and the outer halo is resolved with $200,000$ particles. This minimises spurious heating of the gas particles due to collisions with dark matter particles (Steinmetz & White 1997) and enables us to resolve the dark matter cusp to ~ 100 parsecs. The reliability of these initial conditions are tested and reported in Zemp et al. (2006, in preparation).

The gas has a specific angular momentum distribution and spin parameter consistent with values found for dark matter haloes within cosmological N-body simulations. The initial angular momentum profile is a power law following $j \propto r^{1.0}$, similar to the value $j(r) \propto r^{\alpha}, \alpha = 1.1 \pm 0.3$ found by Bullock et al. (2001). We also ran simulations with different angular momentum distributions to confirm that this does not affect the conclusions in this chapter. The spin parameter is $\lambda = \frac{j_{gas}|E|^{0.5}}{GM^{1.5}}$, where j_{gas} is the average specific angular momentum of the gas, E is total energy of the halo and G is the gravitational constant. This definition matches the one commonly used under the assumption that there is no angular momentum transport between the spherical dark matter halo and the gas. We carried out additional simulations where we set up angular momentum profiles by merging two equilibrium spherical haloes with different impact parameters. Both sets of simulations gave similar results. The detailed description of the runs are presented in Kaufmann et al. 2006b.

We constructed dark plus gaseous halo models with parameters that are expected to produce disks similar to those of the Milky Way (MW model) and NGC 598 (M33 model). For the MW model the virial velocity $v_{vir} = 140$ km/s, virial radius $r_{vir} = 200$ kpc, virial mass $M_{vir} = 9.14 \times 10^{11} M_{\odot}$, halo concentration $c = 8$, spin parameter $\lambda = 0.038$ and the baryonic fraction is $f_b = 9\%$ and we resolve the gas halo with particles of $\sim 2 \times 10^5 M_{\odot}$. For the M33 model the parameters are: $M_{vir} = 5 \cdot 10^{11} M_{\odot}$, $r_{vir} = 167$ kpc, $v_{vir} = 115$ km/s, $c = 6.2$, $f_b = 6\%$ and spin parameter $\lambda = 0.105$. In the standard M33 model the hot gaseous halo is resolved with 2×10^6 particles of equal mass $\sim 2 \times 10^4 M_{\odot}$. To test further the effects of resolution, we performed simulations in which we use eight times as many SPH particles within the inner 30 kpc, the "refined_8" M33 simulation. We split each SPH particle into eight "child" particles (Bromm 2000, Kitsionas 2000, Escala et al. 2004). The new particles are randomly distributed according to the SPH smoothing kernel

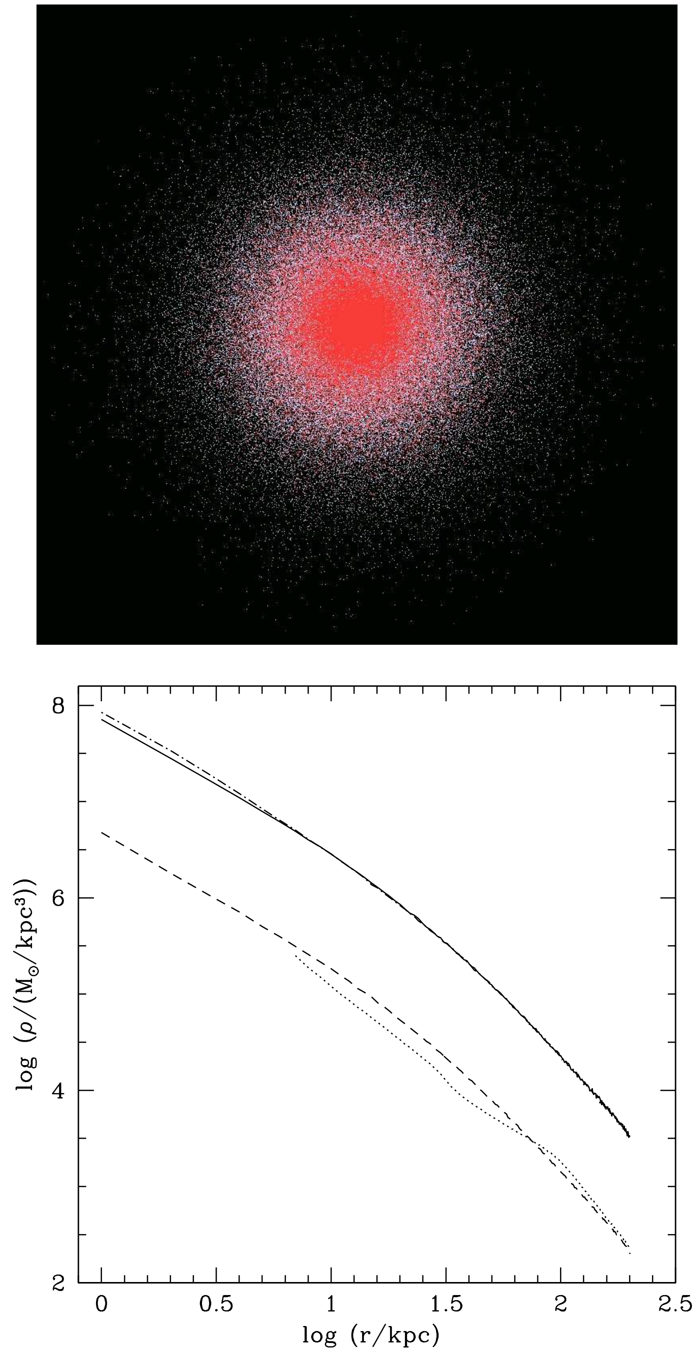

Figure 3.1: The upper panel shows the initial particle distribution (dark matter in white, gas in red, the box has a side length of 1200 kpc) and the lower the panel radial density profiles of gas and dark matter: the density of the dark matter initially is shown with a solid line whereas the dotted-dashed line shows it after 0.5 Gyr. The dashed line shows the initial gas density and the dotted line the density of the hot gas outside the disk region.

within a volume of size $\sim h_p^3$, where h_p is the smoothing length of the parent particle. The velocities of the child particles are equal to those of their parent particle and so is their temperature, while each child particle is assigned a mass equal to $1/N_{split}$ the mass of the parent particle. The new particles have a mass of $\sim 3000 M_{\odot}$. We used then the same method to create the "refined_32" M33 simulation, where each SPH particle within the inner 30 kpc is splitted into 32 particles having masses of $\sim 730 M_{\odot}$. An overview to the M33 simulations can be found in Table 3.1.

We use the high performance parallel Tree+SPH code GASOLINE (Wadsley, Stadel & Quinn 2004), which is an extension of the pure N-Body gravity code PKDGRAV developed by Stadel (2001). It uses an artificial viscosity which is the shear reduced version (Balsara 1995) of the standard Monaghan (1992) artificial viscosity. GASOLINE uses a spline kernel with compact support for the softening of the gravitational and SPH quantities. The energy equation is solved using the asymmetric formulation, which is shown to yield very similar results compared to the entropy conserving formulation but conserves energy better (Wadsley, Stadel & Quinn 2004). In a test problem with an expanding sphere and no gravity, the entropy conservation for each particle as measured by the temperature error has an RMS error of 3% for a factor of 10 change in density; however this is a very conservative estimate since in situations of astrophysical interest entropy conservation should be measured against the other contributors to changes in entropy, namely shocks and cooling, and these are expected to be dominant, especially in the case of a gravitational collapse. In all the runs we included Compton and radiative cooling using a standard cooling function for a fully ionised, primordial gas of helium and hydrogen. The radiative losses per step are limited to no more than 25% per dynamical step and the cooling can adapt the time steps to suit its needs. The density changes are quite slow – occurring on the dynamical time scale and typically less than 1-2 percent per step. Therefore the assumption of a constant density in one time-step contributes only a small error to the cooling rates, especially compared to missing coolants such as metals. Because of the lack of molecular cooling and metals the efficiency of our cooling function drops sharply below $10,000$ K. Moreover we used an artificial lower limit for the gas temperature ($15,000$ K or $30,000$ K), higher than the cut-off in the cooling function, to crudely model the effect of the UV background and stellar feedback (see e.g. Barnes 2002). This temperature floor is also required to avoid the onset of a violent gravitational instability and fragmentation of the gaseous layer after the disk begins to assemble.

For the identification of the clouds we use a friends of friends algorithm (FOF), using 32 particles (equal to the number of particles in the smoothing kernel) as the threshold. The linking length was chosen to be of order 0.3 the mean particle separation in the standard run, it was then lowered for higher resolution (according to the smaller mean particle separation) and we checked in the standard simulation that the number of clouds found with the FOF does depend only weakly on the exact choice of the linking length.

3.4 The assembly of the disk

Due to cooling the hot gas halo loses its hydrostatic equilibrium configuration quite quickly (see Figure 3.5). The inner disk rapidly forms from cooling gas from a nearly spherical region close to the centre (within ~ 10 kpc) of the halo. The accretion rate of cold gas slows down with time and the outer disk region forms from material which flows preferentially down the angular momentum axis. This leaves a "cylindrical" region of hotter and less dense gas above and below the disk plane as is evident in Figure 3.2. This non-spherical inflow of gas from the halo to the disk is not currently considered in semi-analytic models for disk formation.

As expected, the higher angular momentum M33 model produces a more extended disk than the MW model. Furthermore the morphology of the disks within the two models is very different. The higher baryon fraction and lower spin parameter of the MW model gives rise to a disk that dominates the mass distribution in the inner region. The MW model forms a bar in the very early stages and has the appearance of an Sb galaxy whereas the M33 model resembles a galaxy of type Sc-Sd, with a smoother more flocculent spiral pattern. Even though the M33 model does not undergo bar formation, the cooling gas forms a dense central nucleus which has a size of the order our length resolution of a few hundred parsecs. The global morphological evolution of both models depends on the mass and force resolution and is discussed in Kaufmann et al. (2006b). Here we present the analysis of the kinematics of the cooling gas.

3.4.1 Gas infall and extra planar gas

Fraternali et al. (2004) observed the rotation velocity of neutral gas as a function of scale height above the disk for the galaxy NGC 891 which has a luminosity and rotational speed similar to the Milky Way. The found extra planar neutral gas up to distances of 15 kpc above the plane and found a velocity gradient of about -15 km $\mathrm{s}^{-1}\mathrm{kpc}^{-1}$ in the vertical direction. The gas closest to the disk, at $z < 1.3$ kpc, appears to corotate with it but they argue that due to the limited angular resolution this may be the effect of beam-smearing. They considered a galactic fountain model in order to explain these observations, but that model failed to reproduce the amount of lagging. They argue that gas accretion may be important as well in these situations.

Here we present results from our MW simulation where we show that this velocity gradient arises naturally in the accretion phase of the gas as it falls onto the galactic disk. Figure 3.3 shows the rotational velocity of the gas as a function of height above the disk in our MW simulation. We plot the actual circular rotational speed of the gas averaged over the annulus at the given radii. (Note that this is slightly different to the observations which measure the projected rotational speed at a given radius.) The central velocity curve has a bump due to the bar formation and the excess of low angular momentum gas in the inner halo. The decrease in rotational velocity above the plane matches the observations quite well. This suggests that the observations of Fraternali et al. support the idea that disks form via the cooling flow of gas which is rotating faster closer to the disk by conservation of angular momentum.

In Figure 3.3 we plot the rotational speed of all the gas as a function of position above the disk plane, not just gas in the neutral phase such as measured by Fraternali et al. However, in a recent observation of NGC 891 by Heald et al. (2005) it has been found that the velocity gradients of the hot gas agree with the results for the neutral gas. As we then increase the resolution we find that the hot halo is thermally unstable and forms dense gas clouds which then accrete onto the disk. These clouds may cool down and become partially neutral (see section 4.2.1). We only achieve the resolution necessary to observe this two phase medium in our M33 model (see Figure 3.4 for the corresponding velocity plot) but such clouds would occur also in the MW model if we had sufficient

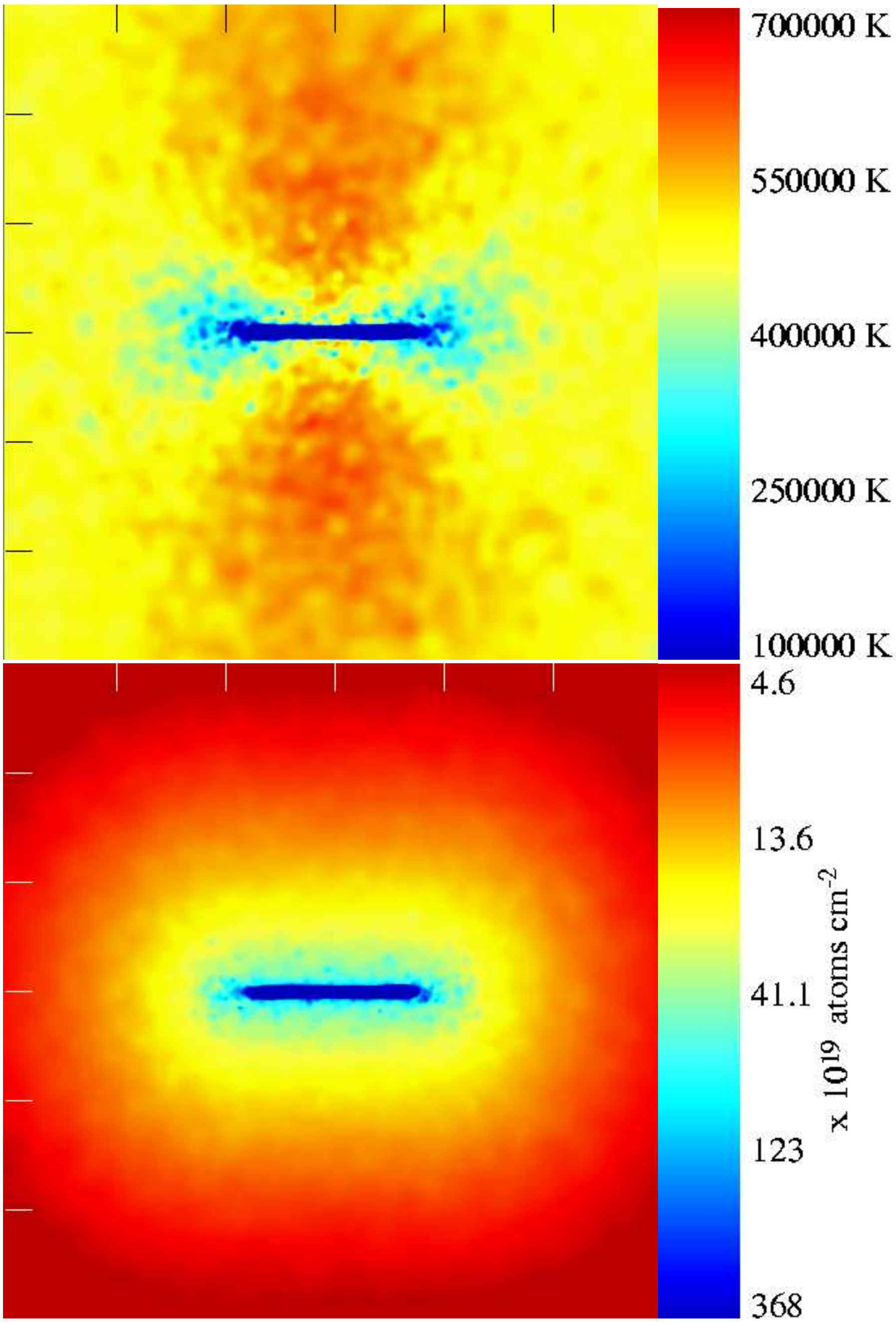

Figure 3.2: The two panels show color maps of projected temperature (upper map) and density (lower panel) after 2.1 Gyr of the standard M33 model (see text). The box has a side length of 60 kpc. The hotter and less dense gas above and below the disk is visible, see text for details.

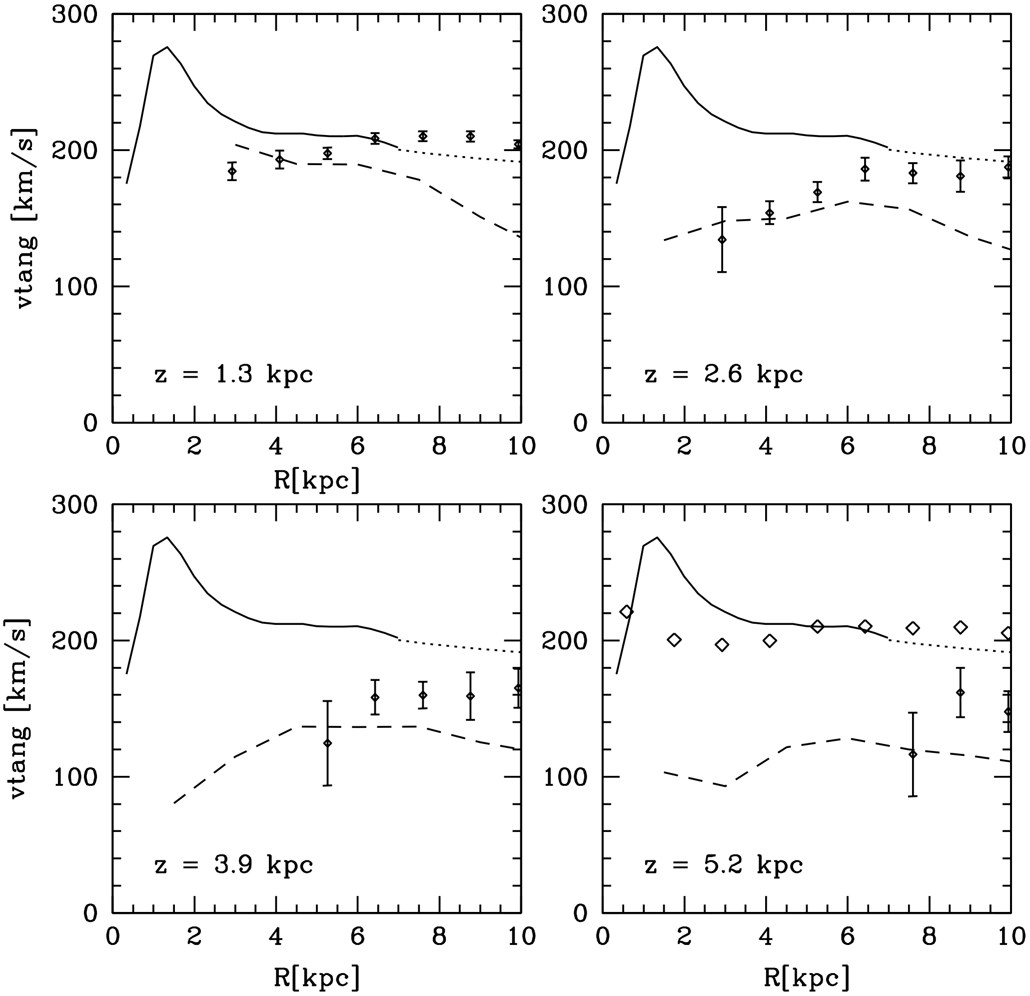

Figure 3.3: The solid lines show the physical rotational velocity of the gas in the disk plane of the MW model. The dashed lines in the different panels show the rotational speed at various distances above the galactic plane. The vertical velocity gradients in the model are $16, 21, 19$ and 17 km $s^{-1}kpc^{-1}$ respectively. The open symbols in the last panel show the observed rotational speed of NGC 891 in the disk plane and the points with error bars in the panels show the observations above the plane of the galaxy. The rotation curve in the disk of NGC 891 is scaled such that the flat part matches the rotation curve in the disk plane of our simulation; the rest of the data and also height z above the disk are then scaled with the same factor.

resolution. Unfortunately, due to the higher baryonic density in the centre of the MW model this simulation is much more demanding computationally since particles require shorter time steps. The cool clouds in the M33 rotate at comparable speed as all the gas, which justifies the measurement of the kinematics within all the gas. The determination of the velocity gradient from the cold clouds alone was only possible in the inner region, because there were too few clouds at higher z in the standard M33 model, but we get a comparable number as if we take all the gas in the plane (Figure 3.4). Figure 3.5 shows that the hot gas halo can not preserve pressure-support for an EOS with cooling. The infall of the hot gas is therefore expected.

The hydrodynamical forces due to diffuse hot corona on the infalling gas are substantial: the infall velocity in the M33 galaxy of the gas above the disk is approximately 10 km/s. This is much smaller than the pure free-fall velocity towards the disk, ~ 70 km/s, This radial infall velocity agrees well with that observed by Fraternali et al. (2002) of approximately 15 km/s for NGC 2403, a galaxy similar to M33. In Figure 3.6 we show the ratio between pressure (hydrodynamical) and gravitational accelerations perpendicular to the disk for some gas particles 2 kpc above the disk. The pressure forces can equilibrate the gravitational forces in average at the $\approx 60\%$ level, which results in this lowered infall velocity. The result for particles which are e.g. 20 kpc above the disk is similar.

3.5 Disk formation via accretion of a clumpy medium

Maller and Bullock (2004, hereafter MB04) proposed that disks form via the accretion of warm clouds that develop from thermal instabilities in the hot gaseous halo (see also Mo & Miralda-Escude 1996). This instability arises as small density fluctuations cool faster than most of the surrounding gas; cooling amplifies these density fluctuations further and the instability rapidly grows. According to MB04 this clumpy formation of disk galaxies would at the same time explain the existence of high velocity clouds and give rise to a characteristic upper limit on the masses of galaxies consistent with observations. Typical parameters for the clouds in a Milky Way-sized halo today would be a size of ~ 1 kpc and a characteristic cloud mass of $\sim 5 \times 10^6 M_\odot$. Several physical mechanisms, e.g. the Kelvin-Helmholtz instability and conduction, impose a lower mass limit on clouds that can survive (see below). These clouds have not been found in cosmological simulations of galaxy formation since even the highest resolution studies have a single SPH particle mass equal to the expected characteristic cloud mass (Governato et al. 2004; Sommer-Larsen et al. 2003).

3.5.1 Formation of pressure confined clouds

In the M33 model we can achieve a higher resolution since the lower density cold component requires less computational work. In the standard M33 model the force resolution is 100 pc or $\sim 0.06\%$ of the virial radius and the SPH particle mass is $2 \times 10^4 M_\odot$. These simulations produce a large population of warm ($T \sim 10^4 - 10^5$ K) high-density, pressure-confined clouds that are forming within the hot ($T \sim 10^6 K$) gaseous halo (see Figures 3.7 and 3.8). These clouds eventually cool down to the temperature floor in our cooling function and would contain substantial fractions of neutral hydrogen. We will discuss the behaviour below the temperature floor in section 3.5.2.3. These clouds are in pressure equilibrium with the halo gas - their gravitational binding energy is typically 50 times

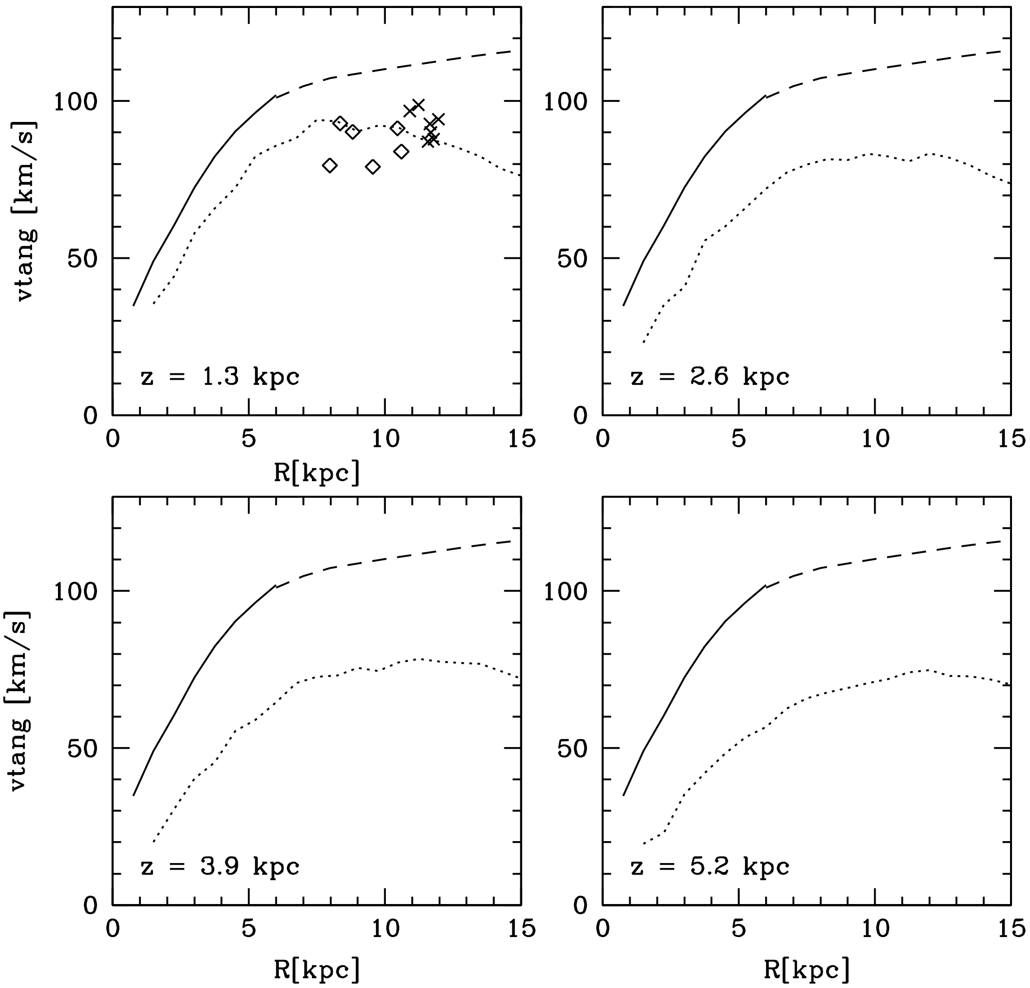

Figure 3.4: The solid lines show the physical rotational velocity of the gas in the disk plane of the M33 model after 2 Gyr (dashed lines show circular velocities). The dotted lines in the different panels show the rotational speed at various distances above the galactic plane of all the gas in the respective plane. The open symbols show the tangential velocities of the cold clouds near the disk, which are between $z = 1.3$ kpc and 2.4 kpc away from the galactic plane, and the crosses mark clouds which are at distances less than 1.3 kpc. The calculated velocity gradients (from all the gas) are $8, 8, 6$ and 6 km $\mathrm{s}^{-1}\mathrm{kpc}^{-1}$ respectively, whereas we get 6 km $\mathrm{s}^{-1}\mathrm{kpc}^{-1}$ for the velocity gradient derived from the clouds.

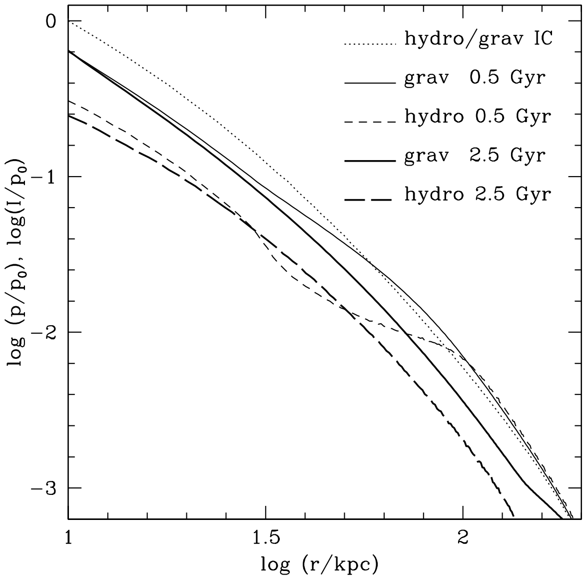

Figure 3.5: The time-evolution of the pressure in the hot gas halo and the gravitational attraction ($I \equiv \int_R^\infty G\rho_g(r)\frac{GM(r)}{r^2}\,dr$) is plotted versus radius (standard M33 run). Initially, gravity and pressure were balancing each other, at later times the gas halo has lost pressure support due to cooling.

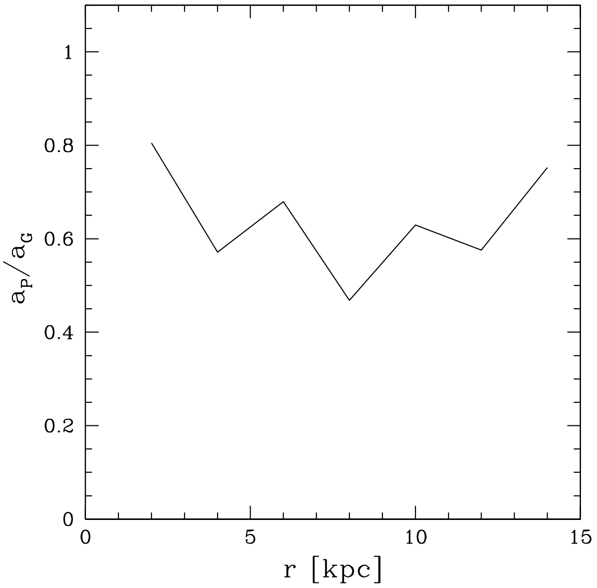

Figure 3.6: The ratio between hydrodynamical and gravitational acceleration in the z-direction (perpendicular to the disk) is plotted versus radius. For this measurement gas particles in a box were chosen, the box is 2 kpc above the disk center and has a height of 1 kpc; the model is 2 Gyr old. In average the hydrodynamical acceleration is $\approx 60\%$ of the gravitational acceleration

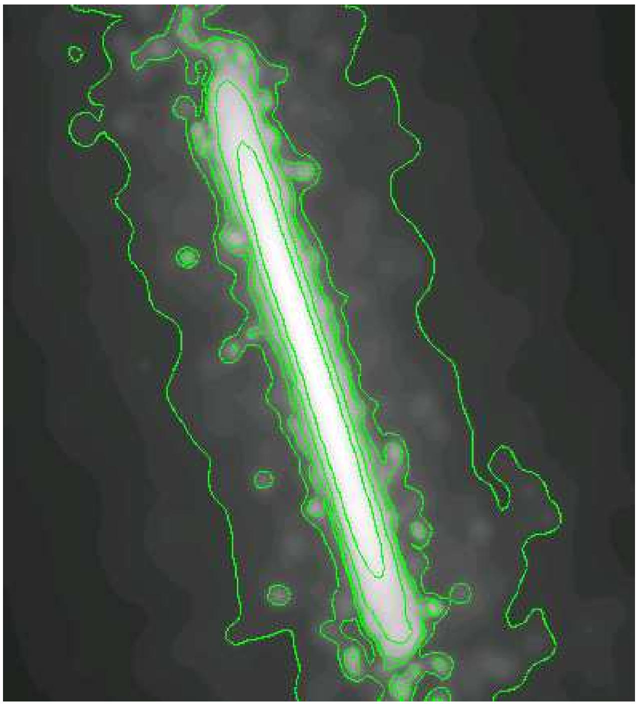

Figure 3.7: The projected gas density of the standard M33 model after 1.5 Gyr shows a clumpy/irregular outer contours similar to that observed in NGC 891. The outer contour shows a gas surface density of $\sim 10^{20}$ atoms/cm^{-2}.

smaller than the thermal energy, hence the clouds are not gravitationally bound. The clouds have radii of $0.1 - 0.6$ kpc and masses from 10^5 to a few $10^6 M_\odot$. As expected, a lower number of clouds is found for a higher number of particles in the SPH smoothing kernel, but at the standard resolution we still see a cloud smoothing over 64 neighbours (Table 1). The parameters of the different simulations and the properties of the clouds are shown in Table 1.

The thermal instability starts because of small density fluctuations present in the initial SPH particle distribution. These fluctuations rapidly grow, increasing in size and density until a pressure confined cold cloud forms. In reality these fluctuations might be driven by external perturbations, for example infall of cold gas and substructure or turbulence induced by supernova winds from disk stars or a galactic fountain. The temperature fluctuations are clearly visible throughout the gaseous halo in the left plot of Fig. 3.9. These cold pressure confined clouds are seen only within about 10 to 20 kpc from the disk. This may be an SPH resolution effect - further out in the halo the gas density is lower and the SPH smoothing length is much larger. Thus density and temperature fluctuations are suppressed by the smoothing.

One of the conditions for cloud formation is that the sound-crossing time, $\tau_\lambda \simeq \lambda_i/v_s$, across a perturbation of wavelength λ_i, should be less than the characteristic cooling time (MB04). If this condition is not satisfied the perturbation is erased because the local cooling time is too close to the mean cooling time and the whole region becomes isothermal. In our simulations we can resolve perturbations in the gas to $\sim 2h$, where h is the smoothing length in the SPH code. We tested this condition in regions around the disk

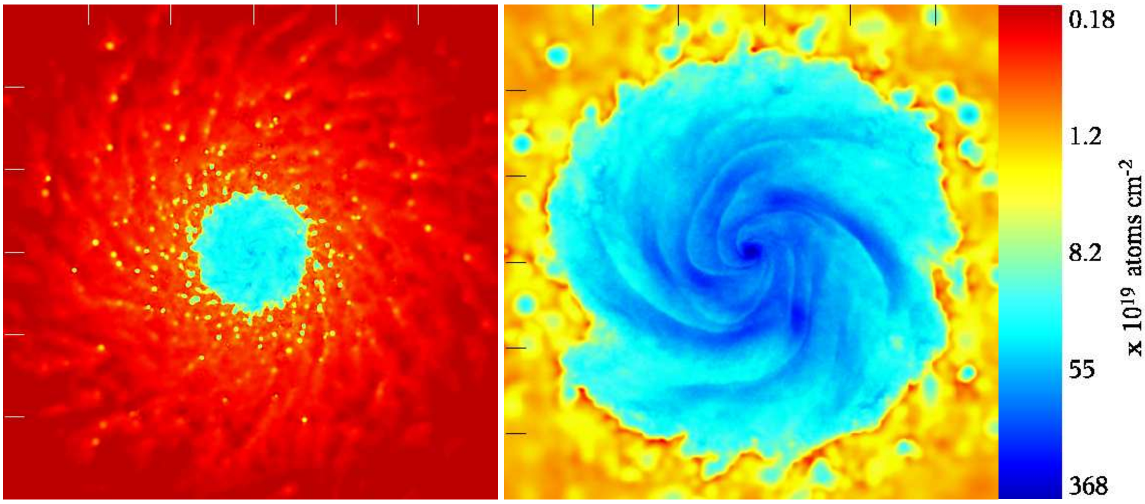

Figure 3.8: Density maps of gas in a slice through the centre of the M33 gas disk in boxes of length 40 kpc (left panel: refined_8 resolution simulation after 0.5 Gyr) and 20 kpc (right panel: standard resolution after 2.1 Gyr). The high-order spiral pattern closely resemble that of Sc/Sd galaxies.

(20 kpc from the centre) where no clouds formed and found that $\tau_\lambda > \tau_{cool} = \frac{E}{|\dot{E}|} = \frac{T}{|\dot{T}|}$ (here we took $\lambda_i \sim 2h$) even at quite low temperatures ($T \approx 30,000$ K). For regions where clouds form, the condition $\tau_\lambda < \tau_{cool}$ is fulfilled where the values of the smoothing length $h \approx 0.65$ kpc.

In order to assess the growth rates and resolution dependence of the instability we performed simple tests using SPH particles distributed randomly in a 10 kpc periodic cube with initial temperature ($T = 450,000$ K) and density ($n_H = 0.01\ cm^{-3}$) comparable to those from the central region of the halo models. We ran three simulations with particle masses 1, 1/10th and 1/100th times those in the full halo simulations. We found cold gas clouds forming above the 32 particle SPH smoothing kernel which grow linearly with time and mass (see Figure 3.10). The higher resolution simulations produce the smallest clouds since they have lower average Poisson fluctuations. After 0.8 Gyr the whole box thermalises as the medium surrounding the clouds has had time to cool down to roughly the same temperature of the clouds. At this point the clouds dissolve into the outer medium since they are not pressure confined any more and the instability saturates.

We can compare the growth rates to those in Burkert & Lin (2000), which derived a condition for exponential versus linear growth in a static, thermally unstable gas layer: the ratio of the initial cooling to sound-crossing time-scale K_j has to be larger than the critical value K_{crit}, where

$$K_j = \tau_{cool}(0) k_j \sqrt{R_g T_0(0)/\mu}, \tag{3.1}$$

$$K_{crit} = \left(\frac{\rho_a}{\rho_0}\right)^{(2\beta-3)\Gamma/(4-2\beta)}. \tag{3.2}$$

and where $\tau_{cool}(0), k_j, R_g, \mu, T_0(0), \Gamma$, and β are the characteristic cooling time scale at time 0, wavenumber, gas constant, initial temperature, mean molecular weight, adiabatic index, and the exponent of the power law of the cooling rate, respectively. ρ_a is the initial perturbation amplitude and ρ_0 the initial mean density. The paper by Katz et al. (1996) shows the cooling rate of a primordial composition gas (as is used in GASOLINE), for $3 \times 10^4 < T < 10^6$ a power law with $\beta = -1$ gives a rough approximation; with $\Gamma = 5/3$ we find $K_{crit} \approx 24.5$ for simulation with the 10% overdensity. For K_j we get ≈ 46.8 using $\tau_{cool}(0) = 0.04$ Gyr, $T_0(0) = 450,000$ K and taking two times the mean smoothing length as the smallest wavelength which is resolved ($\lambda_{min} = 0.16$). Therefore the calculated K_j is not a mean K_j but the maximal one, it's value is roughly two times bigger than the critical value, however the mass (and density) growth remain linear over several cooling times (Figure 3.11). An additional reason for this may be because around 10^5 K the real cooling curve decreases over several ten thousands of Kelvin and would therefore damp an instability.

The thermal instability generated in the cubes is purely of numerical origin since it is seeded by the initial Poisson fluctuations. A higher resolution setup simply starts with lower amplitude of the initial fluctuations, hence the different mass of the transient clouds formed. The following step is thus to impose a perturbation and study how the system responds when we increase the resolution. This way we can assess robustly the dependence on resolution since the initial perturbation is independent on resolution. We used the cubes with particle masses 1/10th and 1/100th times those in the full halo simulations. To wash out initial Poisson noise the cubes were evolved for 5 Gyr using an isothermal EOS (with the same temperatures and mean density as before). Then we placed a spherical overdensity at an arbitrary location within the box. We run three different models where the overdensity was on the 10%, 20% and 40% level, respectively, at both resolutions. We find that the mass of the clouds in this case, just before the whole box thermalises, differs roughly by the same factor as the initial overdensity, the growth rate is linear in time as in the previous cube tests, and the results in the two resolutions nearly converge (see Figure 3.11). In passing we note that the results at 0.4 Gyr probably overestimate slightly the cooled mass due to the overdensity, because in the next time-step the whole box has already thermalised. The fact that we found nearly convergent results has important implications for the collapse simulations that we discuss below. In fact the intermediate resolution test has particles masses comparable to the "refined_8" M33 simulation, which should thus have enough resolution to properly resolve the thermal instability for an initial amplitude of the fluctuations 10% or higher.

So far we had built-in or imposed perturbations as seeds for the thermal instability. We can ask if there is a reasonable way of producing perturbations of order 10% or larger, namely of the same magnitude of those existing in the initial conditions of the full simulations. One way these perturbations can be produced is by dark matter and baryonic substructure in galactic haloes. We carried out an additional test run using the hi-res periodic cube. We added a massive particle with characteristic size (i.e. gravitational softening) and mass comparable to the Magellanic Clouds. The particle moves through the box at a speed of ~ 200 km/s as expected for a dwarf galaxy satellite orbiting in the Milky Way halo. Starting with an isothermal EOS we saw that the particle rapidly triggered the formation of a trailing over-density well above 20% of the background density just behind. Evolved with cooling this over-density grew considerably faster than the fluctuations due to numerical noise, as expected from its larger amplitude. Clearly we have chosen a favourable case since most of the galactic satellites are lighter than the LMC and would drive weaker perturbations. In a CDM halo triggering of gas density fluctuations by substructure should indeed be dominated by the many dark satellites at least 100 times lighter than the LMC. Individually these would drive perturbations that are too small to grow significantly on a dynamical time. However perturbations presumably would not be isolated but would interact, possibly amplifying more rapidly than expected from the linear growth. This is already suggested by the fact that clouds in the full simulations grow faster than in the cube tests due to merging. The presence of a clumpy medium near the disk, which we invoked to explain the observations of Fraternali et al. in previous sections, would suggest that there must be a source of the perturbations acting near the disk, fairly isotropic and active even at the present epoch. Whilst satellite accretion of fly byes may have been frequent enough early in the galaxy formation process to be a major source of perturbations near the disk, other mechanisms are probably responsible for triggering the thermal instability today. Galactic fountains driving turbulence in the inner part of the hot gaseous corona might be one possibility. We will address the question on the physical origin of those perturbations in an upcoming paper.

There are important differences between all the cube tests performed and the full simulation. One that we just mentioned is that in the full simulations clouds can grow faster due to mergers with other nearby clouds (see Figure 3.10). Another one is that the perturbations are not growing out of a static gaseous background as in the cubes but within infalling hot gas. The static case was recently investigated in Baek et al. (2005) where a perturbation at the 20% level was used to produce clouds with masses of about $10^5 M_\odot$ using a grid code. In a similar spirit, Fall & Rees (1985) showed that an initial density perturbation of the order 10% of the average density is needed to produce clouds with masses comparable to those of globular clusters in an infalling medium. This is consistent with the fact that in the full simulations the initial perturbations are larger than 10%, so that one expects the thermal instability to be able to produce fairly massive clouds.

In order to test the effects of resolution directly in the full simulations we have run two simulations with particle splitting. First we carried out the refined_8 M33 simulation. Particles within the refined sphere of 30 kpc reach the disk in about 1.5 Gyr. By running the simulation only up to 1 Gyr we make sure that there is no contamination of heavier particles in the disk, which can lead to spurious results (Kitsionas 2000). The splitting scheme should preserve the amplitude of perturbations at large scales that were present in the original simulation, while noise at previously unresolved scales should trigger the formation of smaller clouds. After 0.5 Gyr (see Figure 3.8 and Table 3.1) there are about 700 resolved clouds with mean mass $1.8 \times 10^5 M_\odot$, up to 19 kpc from the centre. The most massive cloud has a mass of $1.1 \times 10^6 M_\odot$, which is comparable to the most massive cloud ($1.6 \times 10^6 M_\odot$) in the standard M33 simulation *at the same time*. We then performed an even higher resolution run by splitting the initial particle distribution by an additional factor of 4. In the refined_32 there were more than 4300 clouds having more than 32 particles due to the smaller perturbations. The large-scale perturbations were followed similarly in all these three simulations, resulting in a comparable mass distribution of the clouds at the high mass tail, see Figure 3.12. The satisfactory convergence at the scales resolved by all simulations is not a trivial result; it shows that the amplification of the perturbations is numerically robust even in complex simulations such as these in which the gas density does not change simply because the local cooling rate changes but also as a result of compressions and shocks driven by the gravitational collapse. In other words only the initial amplitude of the fluctuations is not self-consistently determined.

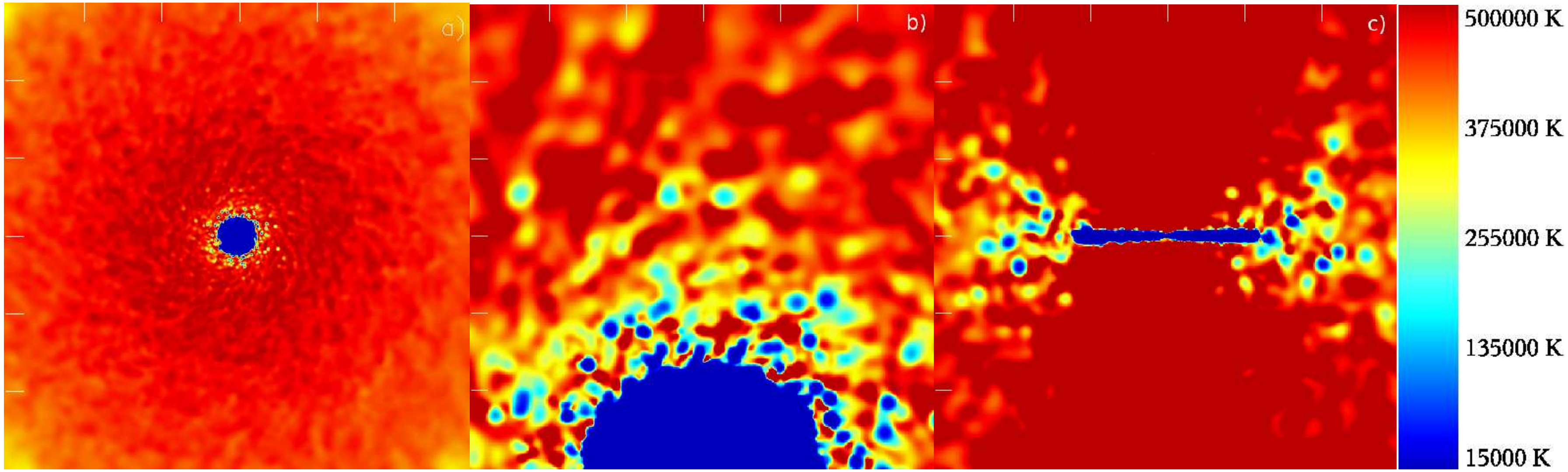

Figure 3.9: Temperature maps of the gas in slices through the centre of the standard M33 simulation after 2.1 Gyr. Panel a) and b) show 200 kpc and 32 kpc regions respectively. Panel c) shows a 40 kpc slice perpendicular to the disk plane.

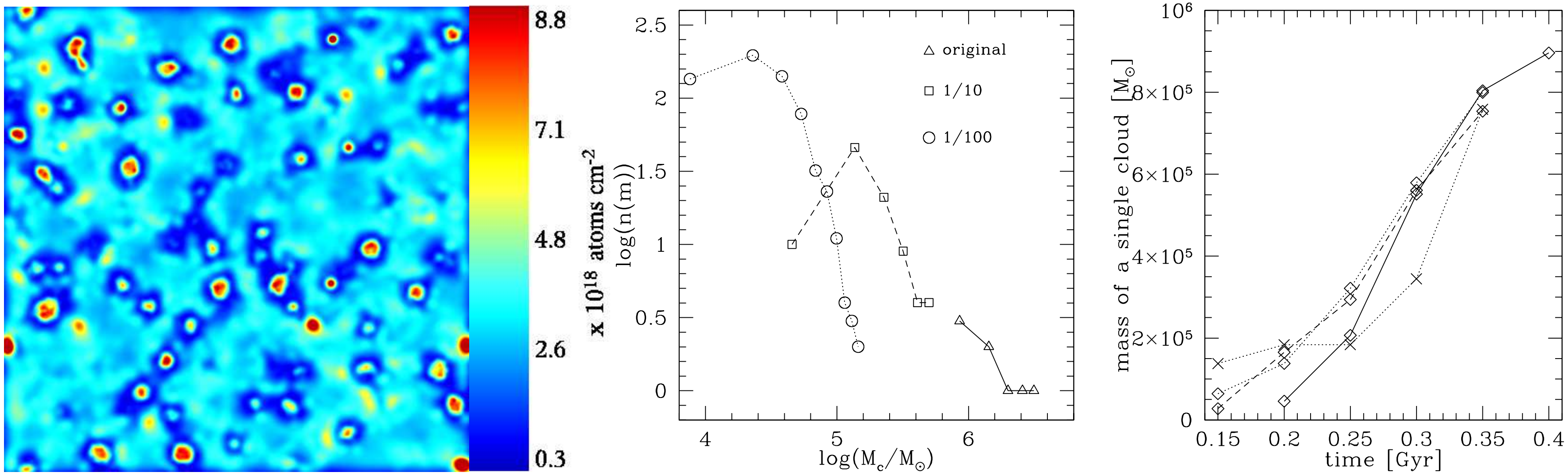

Figure 3.10: The left panel shows a color density map of a slice through the centre of the highest resolution cube simulation after 0.4 Gyr, where red indicates denser regions. The central panel shows the mass distribution of the clouds after 0.4 Gyr The right panel shows the mass growth rate of a single cloud: The cube simulations are plotted with open symbols where the solid lines show the original resolution, dashed line intermediate scaled by a factor 4 and dotted line is the highest resolution scaled by a factor of 40. A cloud from the standard M33 simulation is marked with crosses. In the latter case growth via merging begins after 0.25 Gyr.

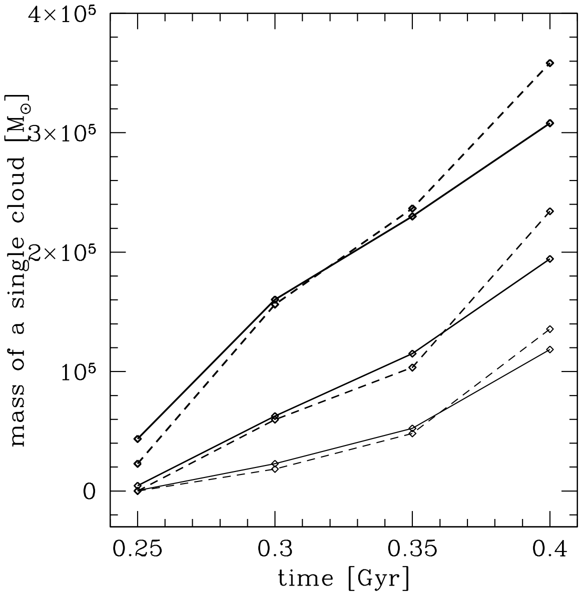

Figure 3.11: The mass growth rate of a single cloud in the box simulation with spherical overdensity is shown: The highest and intermediate resolution are plotted with solid and dashed lines, respectively. The thicker the lines the bigger was the initial overdensity (10%, 20% and 40%). The mass growth was close to linear and the results for the different resolutions nearly converge.

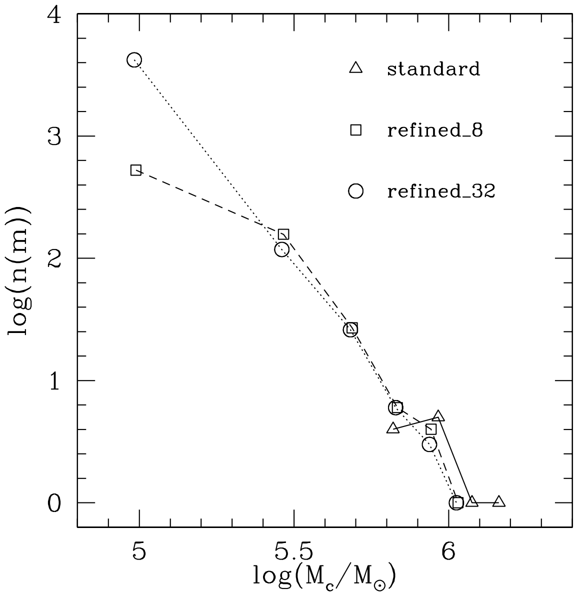

Figure 3.12: The mass distribution of clouds in the M33 simulation after 0.5 Gyr, where the dotted, dashed and solid curves show the refined_32, the refined_8 and standard resolution simulations (see text and Table 1), respectively.

# dark/gas particles	m_g $[M_\odot]$	$T_{cut-off}$ [Kelvin]	Time/Gyr	h_{min}	N_{SPH}	number of clouds	total mass in clouds $[M_\odot]$
$2.5 \times 10^5 / 1 \times 10^5$	4.6×10^5	30000	1.5	-	32	0	0
$1.1 \times 10^6 / 5 \times 10^5$	9.2×10^4	30000	1.5	-	32	2	9.01×10^6
$2.2 \times 10^6 / 2 \times 10^6$	2.3×10^4	30000	1.5	-	32	13	1.23×10^7
$2.2 \times 10^6 / 2 \times 10^6$	2.3×10^4	30000	1.5	-	64	1	2.32×10^6
$2.2 \times 10^6 / 2 \times 10^6$	2.3×10^4	15000	1.5	-	32	13	1.52×10^7
$2.2 \times 10^6 / 3.9 \times 10^6$	2.9×10^3	15000	0.5	-	32	410	7.4×10^7
$2.2 \times 10^6 / 1.0 \times 10^7$	7.3×10^2	15000	0.5	-	32	3662	2.3×10^8
$2.2 \times 10^6 / 2 \times 10^6$	2.3×10^4	15000	0.65	-	32	7	8.46×10^6
$2.2 \times 10^6 / 2 \times 10^6$	2.3×10^4	15000	0.65	20 pc	32	11	1.03×10^7
$2.2 \times 10^6 / 2 \times 10^6$	2.3×10^4	30000	1	-	32	36	4.2×10^7

Table 3.1: Simulation properties of the M33 models and cloud statistics for clouds identified with a friends of friends algorithm are shown. The minimum number of particles for objects to be identified with the FOF was set to be 32, in addition we used also 64 particles for the run with $N_{SPH} = 64$, which gave the same result. The standard, refined_8 and refined_32 simulations are shown, respectively, in the fifth, sixth and seventh row. Rows eight and nine show two equal simulations differing only in the use of a minimal smoothing length. The final row shows the simulation with the enhanced cooling rate. The mass quoted in the second column is referring to the mass of one gas particle initially near the centre.

3.5.2 Evolution and dissolution of the clouds

In the standard M33 run, a typical compact cloud has a mass of $\sim 1.1 \times 10^6 M_\odot$ and a temperature equal to the cut-off temperature in the cooling function ($T_{cloud} = 15000$ K), radius $R \sim 0.2$ kpc and lifetime of ~ 0.1 Gyr (from formation to entering the disk). We now investigate the mechanisms that could disrupt or modify the structure of cold clouds embedded in a hot medium.

3.5.2.1 Kelvin-Helmholtz Instability

As a cool, dense cloud moves through a hot, tenuous background, the interface between the two phases is subject to the growth of Kelvin-Helmholtz instabilities. At our resolution, SPH does not resolve such instabilities due to smoothing and the artificial viscosity which tends to blur any sharp interface between the inner and outer medium. In other words, the Reynolds number is always lower than the Reynolds number expected in turbulent flows where the Kelvin-Helmholtz instability can develop (see Mayer et al. 2005). For the case in which gravity is unimportant Murray et al. (1993) derive a characteristic growth time for the instability of

$$\tau_g \approx \frac{R_{cloud}(\rho_{cloud}/\rho_{bg})^{0.5}}{U}, \tag{3.3}$$

where U is the relative velocity and ρ_{bg} is the density of the background medium. The clouds are therefore expected to break up on time-scales comparable to τ_g. In their numerical experiments they actually found that the mass loss was still quite small over timescales twice as long as τ_g. In our simulations the density contrast is ≈ 100, the relative velocity U is ≈ 10 km/s and therefore we end up with $\tau_g \approx 0.2$ Gyr using 0.2 kpc for the radius of the cloud. Since such timescale is longer than the typical lifetime of the clouds we expect the effect of the Kelvin-Helmholtz instability to be negligible.

The radial infall velocities is of the order 10 km/s which is insufficient to perturb the cloud structure. As the halo gas density becomes lower we might expect clouds to infall faster. Observations of the radial motion of clouds could therefore be used to constrain the ambient halo density.

3.5.2.2 Conduction

In principle, conduction can prevent the growth of small clouds. MB04 suggest random magnetic fields reduce conduction by at least an order of magnitude (the reduction could be much stronger if the field is uniform or tangled) setting a minimum cloud mass of about $10^5 M_\odot$ for a galaxy with mass comparable to that in our M33 model. For the standard simulation presented here, the conduction limit thus lies below the resolution limit imposed by the SPH smoothing volume (and slightly above the resolution limit for the simulation with splitting in 32 particles. The number of small clouds is therefore expected to be lowered due to conduction). At very high resolution, conduction would provide a natural cut-off scale and allow detailed numerical convergence.

3.5.2.3 Cooling below 10^4 K?

Although we used a lower cut-off in the cooling function to prevent fragmentation it is interesting to investigate the fate of the clouds below that temperature. In order to do that we used a "standard" cooling function (e.g. Dalgarno & McCray 1972) to derive an estimate for the cooling timescale of the clouds below 10^4 K. We adopted the parameterization of Gerritsen & Icke (1997) for the temperature range of $\log T < 6.2$:

$$\Lambda = 10^{-21} n_H^2 [10^{-0.1-1.88(5.23-\log T)^4} + 10^{-a-b(4-\log T)^2}] \tag{3.4}$$

in ergs cm^{-3} s^{-1}, where a and b depend on the ionisation parameter $x = \frac{n_e}{n_H}$. The heating term for photoelectric heating of small grains and PAHs (as the largest contributor to the gas heating) is given as $\Gamma = 10^{-24} \epsilon G_0 n_H$ in ergs cm^{-3} s^{-1}, where ϵ is the heating efficiency and G_0 the incident far-ultraviolet field (Bakes & Tielens 1994). The FUV field originates from star formation in the disk; since we are resolving only clouds very close to the disk we can simply assume that they will be embedded in the same bath of ionising photons as the rest of the galaxy. With

$$\frac{du}{dt} = \frac{\Gamma - \Lambda}{\rho} \tag{3.5}$$

(Hernquist & Katz 1989) one can give an estimate of the cooling time for such systems neglecting pressure and velocity terms. A typical cloud in our simulation can cool down during its lifetime to several tens of Kelvin for ionisation parameters $x \geq 0.1$ in less than 1 Myr, for $x \leq 0.01$ an equilibrium is reached at several thousand Kelvin. The dynamical time-scale $t_{dyn} = \sqrt{\frac{3\pi}{16G\rho}} \approx 70$ Myr for such a cloud is of order of its lifetime. Therefore the clouds could collapse further for $x \geq 0.1$ (a value which should be reasonable for the solar neighbourhood, see Cox 1990). On the other hand MB04 find that the extragalactic ionising background should prevent the cooling of the clouds below $10^4 K$. Self-shielding effects will also be important to decide the ultimate fate of the clouds under the combined action of different heating and cooling mechanisms.

Had we included metals in the simulations the cooling rate would have been higher. We crudely explored the effect of metals by simply shifting the entire cooling curve up. We found, as expected, that more efficient cooling leads to a larger number of clouds for a given resolution; doubling the energy loss due to cooling (this modified cooling function is somewhere in between primordial gas and gas with solar metallicity) increased the mass and the number in clouds by a factor of order 2.7 whereas the mass per cloud and the spatial extent of the clouds remained comparable.

3.6 Conclusions

We studied the cooling flow of gas within equilibrium dark plus gaseous haloes. At high resolution the gas nearly conserves angular momentum and rotates faster as it moves towards the disk. Within $10-20$ kpc from the disk the gas fragments into cold gas clouds pressure confined by the ambient hot halo gas. The clumpy appearance of the gas matches HI observations of outer disks. These cold clouds have similar properties as predicted in analytic models such as that of MB04. However, one difference with MB04 is that the hot gas component is never in approximate hydrostatic equilibrium once it starts cooling and collapsing. This implies, for example, that the disk assembly will occur faster than predicted by a model such as MB04. The mass of galaxies with a given spin should also be different, presumably higher in our case since there is less pressure support against collapse. Unfortunately a direct comparison in terms of galaxy masses is not possible at this stage since the refined runs that have enough resolution to properly follow the clumpy disk formation have been run only for a very short timescale. The background gas cools and falls in towards the disk as it loses pressure support. Its radial infall velocity is comparable to that of the cold clouds. This explains why we do not see significant differences in the mass growth of the disk when we compare simulations which yield a very different degree of clumpiness of the accretion flow such as the standard and refined_32 simulations. In our models the amount of hot gas which is accreted directly to the disk is substantial, however, even after 5 Gyr, there is a residual hot gas halo, such that a large mass fraction of the baryons remain in the halo.

The gas does not accrete onto the disk via a spherically symmetric flow. Rather it flows down a cylindrical fashion along the angular momentum axis. This is different from that assumed in semi-analytic models for disk formation. The rotational velocity of the gas decreases above the disk plane with a similar velocity gradient as observed in the measurements for NGC 891 by Fraternali et al. (2004). This may be the first evidence for disk formation via radiative cooling of hot gas combined with conservation of angular momentum.

Our simulations show that the thermal instability, and thus the two-phase medium, requires a continuous heating source to be present in order to be maintained, and this is provided here by the gravitational collapse which continously brings in gas hotter than the gas that has already cooled down. When this heating term is not present, such as in all the cube tests, the instability is rapidly suppressed as the temperature becomes uniform due to the high cooling rate.

We believe that the clouds are stable against the various disruption mechanisms such as conduction and Kelvin-Helmholtz instabilities. The infall velocity of the gas is approximately 10 km/s. This is much smaller than the pure free-fall velocity towards the disk, $\sim$ 70 km/s, owing to the drag exerted by the diffuse hot corona. This velocity can thus be used to measure the ambient hot gas density above the disk plane. This radial infall velocity agrees well with that observed by Fraternali et al. (2002) of approximately 15 km/s for NGC 2403, a galaxy similar to M33.

In the refined_32 simulation the sky coverage factor of the clouds is approximately 25%. This is quite similar to the sky coverage factor of high column density High Velocity Clouds (HVCs) (Richter 2006). The Number of cold clouds in our (refined_32) simulation is also similar to those estimated by Putman et al. (2006). However we caution against over-interpreting these intriguing results. In our model several physical ingredients that might have an impact on cloud formation, such as gas metallicity, and survival (such as conduction) are still missing, and the initial perturbations are still not determined self-consistently in the mode. It is interesting that cosmological simulations are now beginning to resolve similar structures (Governato et al. 2006, Sommer-Larsen 2006) and that the origin of the perturbations in some of these simulations seems to be dense cold gaseous streams accreted in the process of galaxy formation (Sommer-Larsen 2006). If cold accretion is responsible for the cloud formation it would have the benefit of being a very general mechanism, although it would occur preferentially in the early stages of their formation for systems as large as the Milky Way today (Keres et al. 2006).

The growth rate of the cloud masses is approximately linear with time, therefore large initial fluctuations in temperature or density are required. It is likely that the Poisson fluctuations due to discreteness, which are at the 10% level, are coincidentally close to the amplitude of fluctuations required to form $10^6 M_\odot$ clouds within a Gyr. In addition to perturbations of cosmological origin for the clouds to be connected with HVCs one needs mechanisms that are efficient at any epoch, such as triggering by halo substructure. This includes not only the direct perturbation of sub-haloes moving in the primary halo but also cold gas streams stripped from the baryonic component of the satellites (Mayer et al. 2005). Finally, in order to generate the HI clouds in the extra planar gas around disks one needs also local sources of fluctuations such as infalling cold gas or turbulence induced by gravitational perturbations or supernova winds from star formation in the disk. A lot remains to be done to study the role of these different triggering mechanisms which might be simultaneously at play and generate various populations of clouds.

Acknowledgments

We would like to thank Stelios Kazantzidis for providing a code to generate isolated dark matter haloes and Filippo Fraternali for the rotation curve data for NGC 891. We acknowledge useful and stimulating discussions with Filippo Fraternali, Renzo Sancisi, Frank van den Bosch, Kenneth Sembach, Leo Blitz, Tom Quinn, Fabrizio Brighenti and Fabio Governato. We are grateful to the anonymous referee for his remarks and stimulating comments that considerably improved the paper. The numerical simulations were performed on the zBox (http://krone.physik.unizh.ch/∼stadel/zBox) supercomputer at the University of Zürich.

Chapter 4

Tilting and warping during galaxy formation

4.1 Abstract

The formation of disk galaxies with S- and L-shaped warps is followed using self-consistent N-Body/SPH simulations. Long-lasting symmetric warps are forming due to accretion of gas which has misaligned angular momentum. Variable, asymmetric warps are observed in simulations where a satellite halo consisting of gas and dark matter falls in. Those warps are forming due to a combination of accretion of gas with misaligned angular momentum and tidal forces from the infalling satellite. For a primary to satellite mass ratio of 10:1 a close passage is needed to excite warps.

4.2 Introduction

Disk galaxies owe their existence to angular momentum. During formation and also later in their evolution, angular momentum is not, however, accreted symmetrically or even with fixed orientation. As a consequence, disks can change their orientation, often times differentially, i.e. they develop warps. The disks in many spiral galaxies are not flat and their outer parts often show warping of material away from the galactic midplane (e.g. Sancisi 1976, García-Ruiz et al. 2002). Warps are mostly seen in in the atomic hydrogen gas (H I) in the outer parts of a galactic disk (e.g. Sancisi 1976) and can be either S-shaped (integral-shaped), U-shaped or L-shaped warps (García-Ruiz et al. 2002, Levine et al. 2006). Warps are seen in a significant fraction of the spiral disks, mechanisms which try to explain warps should therefore produce warps which are either long-lived or repeated frequently. There are different attempts in literature to explain these warps, e.g. by bending instabilities (Revaz & Pfenninger 2004), inclined disk formation in oblate dark haloes (Dubinski & Kuijken 1995), cosmic infall (Jiang & Binney 1999; Huang & Carlberg 1997), tidal excitation (Weinberg & Blitz 2006) or misaligned angular momenta (Debattista & Sellwood 1999). Saha & Jog (2005) showed, how the first two bending modes in the disk can produce asymmetric warps.

Briggs (1990) characterised the behaviour of warped H I disks of 12 galaxies as (1) coplanar inside R_{25}, and warped beyond, with a straight line of nodes (LON) inside the Holmberg radius R_{Ho}, (2) changing near R_{Ho}, (3) into a LON on a leading spiral (as seen from the inner disk) outside R_{Ho}.

One of the favoured explanation for galactic warps is that they are driven by torques applied by the outer dark halo on the inner galaxy because the outer and inner parts of the halo are misaligned either in density or in their angular momentum (Binney, Jiang & Dutta 1998; Debattista & Sellwood 1999). Such misalignment would be a natural consequence of the accretion of material that has angular momentum whose axis is inclined with respect to the symmetry axis of the inner galaxy. Standard cosmological models predict that galaxies should be accreting material, and that the direction of the net angular-momentum vector of the material that is currently being accreted should be changing (Quinn & Binney 1992). Sanchez-Salcedo (2006) found that accretion of a flow with no net angular momentum cannot be the main and only cause of warps. We will take this into account by modeling the infall of matter which has angular momentum.

In the spirit of cosmic infall (i.e. accretion of material with different angular momenta) we report here on how radially segregated angular momenta affect the forming gas disk. This is independent of the mode of accretion of the material with different angular momentum. We will present models where the inner halo accretes new material via spherically symmetric infall from the outer halo and a model where the accretion is due to an infalling massive satellite galaxy. For the smooth infall we show that the growing disk tilts towards the total angular momentum vector of the system. This evolution is quite general; even when the gas remains hot for some significant fraction of a Hubble time, it still retains a memory of its radial segregation and the forming disk still tilts. However it does so more gently and less differentially and a smaller warp forms. We then show that flybys produce asymmetric warps which are probably the first ones seen and analysed in an N-Body/SPH simulation. The presence of these warps is dependent on the mass of the infalling satellite, we find that the satellite has to have a significant fraction of mass of the parental halo or a relatively close passage from the disk to cause the disk to warp. For example, we do not expect the Magellanic Clouds to affect the Galactic disk.

We will present two self-consistent SPH simulations models A and B (described in the next section) which follow the formation and warping of a galaxy with mass comparable to the Local Group spiral galaxy M33. These simulations model the formation of a galactic disk via the cooling of gas inside equilibrium dark matter haloes. The structural parameters of the model are motivated by the results of cosmological simulations and are designed to follow the quiet gas accretion phase during the main epoch of disk formation, which allows us to resolve the baryonic galaxy much better. In model A we follow the warping of the galactic disk inside a gas and dark matter halo where at later times the infalling gas has different angular momentum than the gas from which the disk has formed initially. Model B - a simulation in which we follows merger-events - is closer to a cosmological situation. In both models either symmetric (model A) or both symmetric and asymmetric warps (model B) were observed.

The outline of the chapter is as follows: In section 4.2 we present the initial conditions, numerical techniques and some details on how the warps have been analysed. In section 4.3 we discuss the results of the model which has smooth gas accretion whereas we report in section 4.4 on the models with infalling satellites. We summarise and conclude in section 4.5.

4.3 Numerical methods

4.3.1 Initial Conditions

Our initial conditions comprise an equilibrium NFW galaxy-sized halo with an embedded spinning gaseous mass distribution in hydrostatic equilibrium, similar as described in more detail in Kaufmann et al. (2006b). The parameters of our models are comparable to that expected for the nearby spiral galaxy M33 (Corbelli 2003, details are described below).

The halo models are built as in Kazantzidis, Magorrian & Moore (2004), and hence they include a self-consistent description of the velocity distribution function. Model A consists of a spherical dark matter halo and an embedded equilibrium gaseous halo. Our initial halo has a circular velocity at the virial radius, v_{vir}, which, for an assumed cosmology (hereafter $\Omega_0 = 0.3, \lambda = 0.7, H_0 = 70$ kms^{-1} Mpc^{-1}) automatically determines the virial mass, M_{vir}, and virial radius, R_{vir}, of the halo (Mo, Mao & White 1998). We choose $v_{vir} = 115$ km/s, which corresponds to $r_{vir} = 167$ kpc and therefore $M_{vir} = 5 \times 10^{11} M_{\odot}$. Haloes have NFW density profiles (Navarro, Frenk & White 1996) with halo concentration c and different spin parameters. The concentration is defined as $c = \frac{r_{vir}}{r_c} = 6.2$, where r_c is the halo scale radius.

The gaseous halo is constructed in the same way and contributes in mass 6% of the total mass to the system. The temperature structure (in the range of $\sim 10^6 K$) of the gaseous halo is calculated by solving the equation for the hydrostatic balance of an ideal gas inside a dark matter halo. The hot gas starts with a non-vanishing specific angular momentum distribution: velocities were given to the gas particles such that they were initially on circular orbits and that the initial specific angular momentum profile is well fitted by a power law following $j(r) \propto r^{1.0}$. The dark matter halo starts with no angular momentum. (Bullock et al. 2001 proposed a power law with $j(r) \propto r^{\alpha}, \alpha = 1.1 \pm 0.3$.) We used a spin parameter $\lambda = 0.1$, and calculated $\lambda = \frac{j_{gas}|E|^{0.5}}{GM^{1.5}}$, where j_{gas} is the average specific angular momentum of the gas, G is the gravitational constant, E and M are the total energy and mass of the halo, respectively. This definition matches the one commonly used (e.g. Mo, Mao & White 1998) under the assumption that there is no angular momentum transport between the spherical dark matter halo and the gas. The angular momentum vector was chosen to be parallel to the z-axis. All the gas particles further than 30 kpc away from the centre were rotated by 45 degrees around the x-axis, i.e., the angular momentum vector of the outer gas particles and the z-axis include an angle of 45 degrees whereas the spacial spherical symmetry was conserved. For this configuration the resulting specific angular momentum vectors of the gas are $\mathbf{j}(r < 30$ kpc$) = (1, -1, 566)$ and $\mathbf{j}(r < 167$ kpc$) = (4, -1625, 1747)$ in kpc km/s. We used $250,000$ dark and $100,000$ gas particles. The mass of the dark and gas particles are therefore $\approx 2 \times 10^6 M_{\odot}$ and $\approx 4 \times 10^5 M_{\odot}$, respectively. These initial conditions are intended to model a dark matter halo which has gas accreted from different "sources" and at different times (e.g. via cooling flows along filaments) and the gas has therefore different angular momentum. For most runs we use a softening $\epsilon = 0.25$ kpc, however, we re-simulated some of the models A with $\epsilon = 0.1$ kpc to check for resolution effects, see next section.

Model Ac was then evolved for 10 Gyr using an equation of state (EOS) with cooling (for details on the cooling see below). A second model (called "Aad") was first evolved with an adiabatic EOS for 3 Gyr and then for another 5 Gyr with cooling. In the early universe when cooling is inefficient, model Aad is expected to be closer to reality whereas model Ac will be more realistic for later times.

Model B, the merger simulation, was constructed similarly. First, we build three gas plus dark matter haloes as described above, but with half of the mass and no angular momentum (and therefore no rotation of the outer particles). Two haloes are then separated by twice their virial radius and one is given a transverse velocity of 50 km/s in order to obtain the same spin parameter as model A. Each of the species in each halo were represented with $100,000$ particles. The mass of the dark and gas particles are therefore $\approx 3 \times 10^6 M_\odot$ and $\approx 2 \times 10^5 M_\odot$, respectively, which should limit numerical angular momentum losses as reported in Kaufmann et al. (2006b). The model was then evolved for 20 Gyr with an adiabatic equation of state for the gas and softening 0.25 kpc. The amount of angular momentum of the gas and the masses inside the virial radius was comparable to the IC of model A, the shape of the angular momentum profile was slightly different, see Figure 4.1, the angular momentum vector was parallel to the z-axis and the dark halo was not spherical but oblate. Then the model was evolved another 2 Gyr with cooling and a disk started to form, similar as reported in Kaufmann et al. (2006b). After this 2 Gyr the third halo was added, resulting in a $2:1$ merger, again in a distance of two times the virial radius with a transverse velocity of 50 km/s. The third halo was placed such that the angular momentum vector of the third halo (with respect to the center of the disk) include an angle of 45 degrees with the z-axis. For this configuration the resulting specific angular momentum vectors of the gas (measured with respect to the centre of the disk) are $\mathbf{j}(r < 30 \text{ kpc}) = (7, -7, 648)$ and $\mathbf{j}(r < 350 \text{ kpc}) = (3, -1934, 3607)$ in kpc km/s. Then the model was further evolved with cooling. In addition to this model B we checked the dependence on the mass of the infalling satellite halo. We use analogous models but with lowered mass for the third halo, such that a $5:1$ and a $10:1$ merger resulted, named B5 and B10, respectively. To compare with the infall of a dark satellite we used the model "Bdark", where the infalling halo had the same properties as in model B, but contains no baryons.

We use the parallel TreeSPH code GASOLINE, which is described in Wadsley, Stadel & Quinn (2004). The code is an extension to the N-Body gravity code PKDGRAV developed by Stadel (2001). It uses an artificial viscosity which is the shear reduced version (Balsara 1995) of the standard Monaghan (1992) artificial viscosity. GASOLINE solves the energy equation using the asymmetric form and conserves entropy closely. It uses the standard spline form kernel with compact support for the softening of the gravitational and SPH quantities. The code includes radiative cooling for a primordial mixture of helium and (atomic) hydrogen. Because of the lack of molecular cooling and metals, the efficiency of our cooling functions drops rapidly below 10,000 K. We did not include any heating source such as the cosmic UV background or feedback from supernovae and we enforce a lower limit for the temperature that the gas can reach via radiative cooling to $\mathrm{T}= 20,000$ K to prevent heavy gravitational instabilities. This can be seen as a crude way to mimic the effect of the missing heating sources (see also Barnes 2002).

4.3.2 Briggs diagrams

Briggs (1990) introduced a polar coordinates diagram (hereafter Briggs diagram) for analysing warps. We use a modified version of these to study our systems. Our Briggs diagrams decompose a system into a series of concentric rings. For each of these rings, the direction of the angular momentum vector is represented by the two-dimensional cylin-

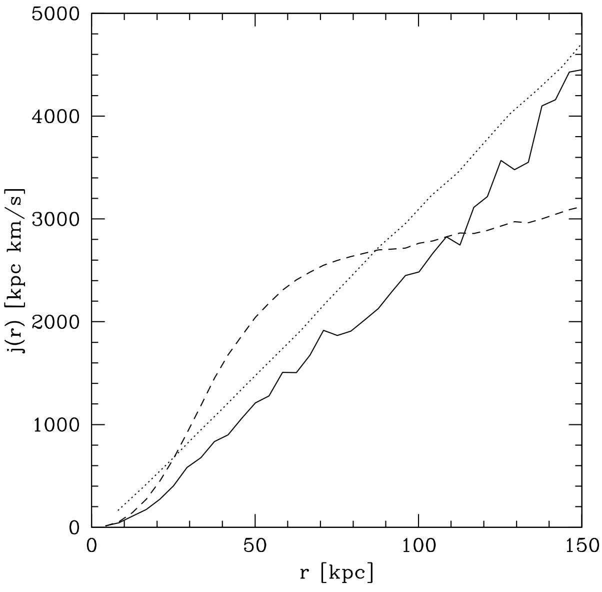

Figure 4.1: The specific angular momentum profile after the first merger (model B): dark matter (solid line) and gas (dashed line). The dotted lines show the specific angular momentum profile of the gas from the spherical model A.

drical polar coordinates. The tilt of the angular momentum vector from some fiducial z-axis, θ, is plotted as the radial coordinate while the angle from some fiducial x-axis, ϕ, is plotted as the polar cylindrical coordinate. Briggs diagrams are useful for showing the evolution of a tilting disk provided that the x, y and z axes with respect to which the angles θ and ϕ are defined are kept fixed. In Figure 4.2 we present an illustrative example of a Briggs diagram for a toy model galaxy consisting of two rings.

In our experiments we always set the z-axis to be the direction of the angular momentum for the inner gas (runs Aad and Ac). The x and y-axes are arbitrary but held fixed.

4.4 Warps by smooth accretion of gas with different angular momentum

In model Ac a flat disk perpendicular to the angular momentum vector of the inner sphere started to form during the first phase of cooling, after about 2.5 Gyr - the time where particles from the outer halo reach the disk region - the warp of Model A started to become prominent, see Figure 4.3. Before this time the inner disk consists only of particles from this inner sphere whereas at later times the (integral sign) warp consists of some of the central particles but mostly particles from the outer shell, see Figure 4.4. As time proceeds, particles continue to cool onto the disk from the outer halo and the disk is tilted differentially, leading to the warp. After 3 Gyr more than 10% of the disk consists of particles of the outer halo. We analyzed this warp using the methods described in Briggs 1990, see Figure 4.5, and find, that it is in good agreement with observations, i.e., that the galaxy is coplanar inside some radius with a straight lines of nodes (LON) and change

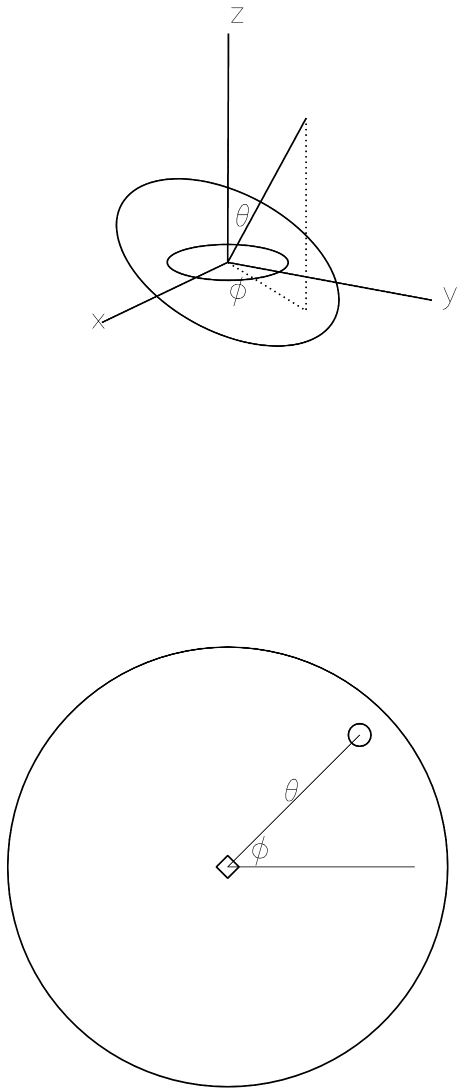

Figure 4.2: An example of a Briggs diagram. In top we show the physical system, which consists of only two rings, the inner one in the $x - y$ plane and a tilted outer one with spherical polar angles θ (measured from the z-axis) and ϕ (measured in the $x - y$ plane from the x axis). In the bottom panel we plot the corresponding Briggs diagram with the diamond corresponding to the point for the inner ring and the open circle corresponding to the outer ring.

further out into a LON on a leading spiral (Briggs rules).

This strong warp survives a few Gyr whereas the inner disk does not bend, see Figure 4.3. After 7 Gyr the warp has significantly weakened and at the end (10 Gyr), when the reorientation of the disk has settled a warp of about 5 degrees remains. Then, the disk is perpendicular to the the specific angular momentum vector of all the gas, i.e., with an angle of ~ 45 degrees to the z-axis, see Figure 4.6 for the time-evolution of the direction of the angular momentum vector of the disk. We checked then the influence of the softening by re-simulating model A from 5 Gyr with better force resolution, i.e. we lowered the softening by factor 2.5. There were no major differences in the warp.

The adiabatic evolution in the first 3 Gyr in model Aad leads to a smooth transition of the inclination angle of the angular momentum vector from 0 in the inner part to 45 degrees in the outer part (also after 10 Gyr of adiabatic evolution a single direction of the angular momentum vector has not established yet, as one might expect), whereas the IC for model Ac had a sharp transition at $r = 30$ kpc, see Figure 4.6. Using this adiabatically relaxed system as an initial condition for the cooling phase a slight warp results after 1 Gyr of cooling (then, the disk is still quite small), after that, the warp fades away quite quickly and the disk starts to tilt similar as in model Ac described above, see Figure 4.7.

At the sharp boundary at $r = 30$ kpc between the two different spinning haloes the development of a Kelvin-Helmholtz-instability (KH) is expected. Even at the high resolution adopted here SPH is hardly capable of resolving KH-instabilities mostly because the artificial viscosity and the fact that densities are smoothed in SPH both contribute to smoothing and suppressing instabilities. We tested the influence of the KH-instabilities by running a shearing box test with gasoline and the AMR code Enzo (Bryan & Norman 1997). The periodic box was 50 kpc a side with gas having density and temperature ($\rho \approx 10{-}3\ \mathrm{cm}^{-3}$ and $T \approx 836,000$ K) as at the $r = 30$ kpc boundary of the full simulation. The upper half of the box has the same velocity as the velocity-difference (≈ 37 km/s) at the boundary, whereas the lower part was at rest. Only with a high-resolution run using Enzo, the KH-instabilities was followed. However, in all of the Enzo runs, two layers with different velocities remain over several Gyr. We argue that our full simulations (although not resolving the KH-instabilities correctly) do not underestimate the mixing. If the mixing would be underestimated, more prominent warps would be expected.

Warm disks are less prone to warping, probably because a warm disk cannot support bending modes with a wavelength shorter than the average epicycle diameter (see Debattista & Sellwood 1999). We found for the Toomre parameter (Toomre 1964) of those models $Q > 1$ (see Figure 4.8) before and after warp-formation, which is not excessively cold. Note for comparison, that for a thick gas disk the limit for stability against axisymmetric perturbations is lowered from 1 to ≈ 0.6 (Romeo 1994).

In the right plot of Figure 4.6 we show how model B (using an adiabatic equation of state all the time) can produce an initial condition resembling model Ac. This simulation showed a comparable memory of its initial spin configuration similar as model Aad: although more violent processes took place due to the merger-event it took another 5 Gyr until a single angular momentum vector has developed.

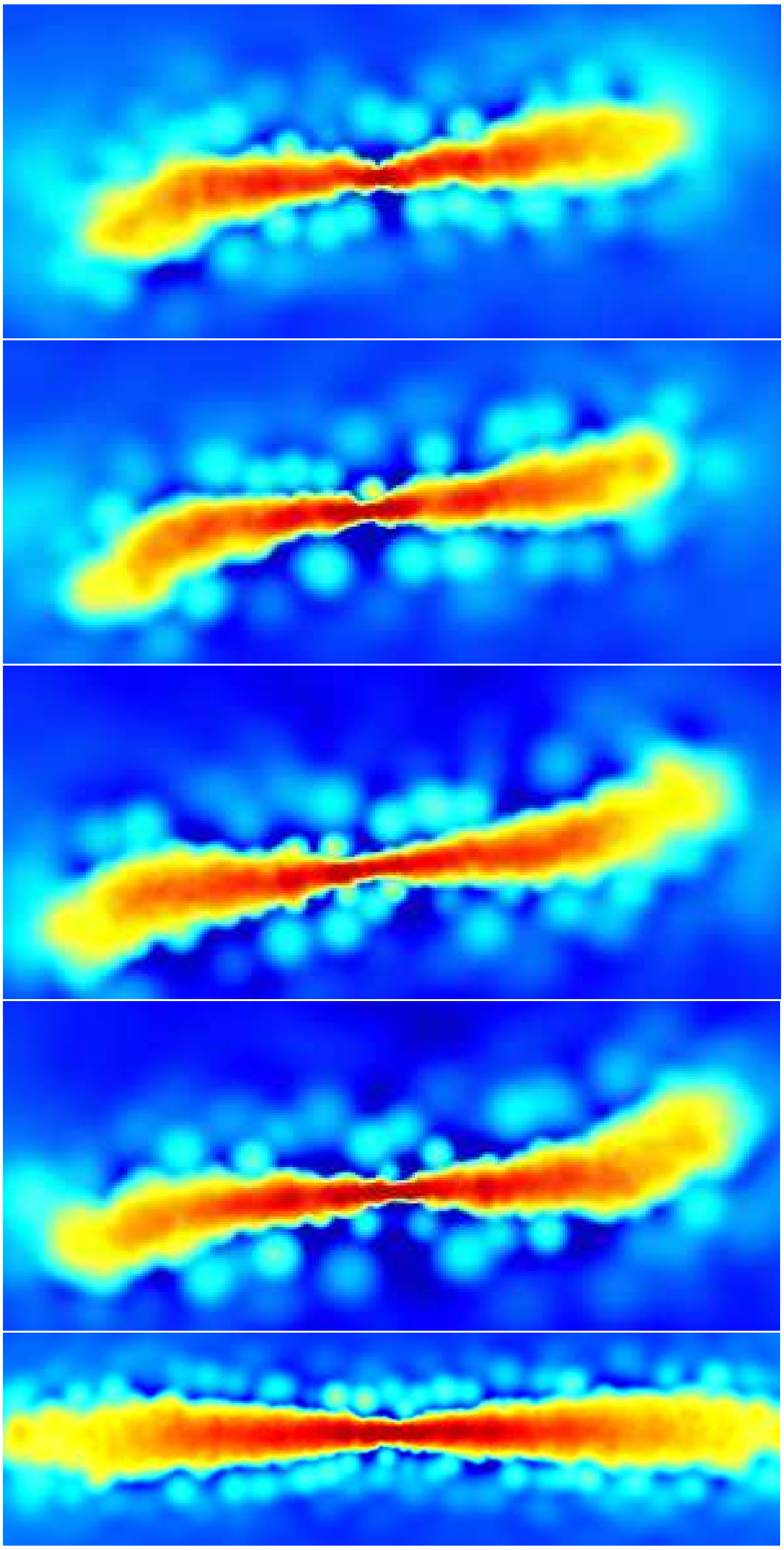

Figure 4.3: Density maps of gas in a slice through the centre of Model A. From top to bottom: 2.5, 3, 4.5, 5 Gyr of evolution. The last panel is the corresponding control "M33" run after 4.5 Gyr, where the angular momentum vector of all the gas was aligned initially (Kaufmann et al. 2006a). The length of each box is 24 kpc.

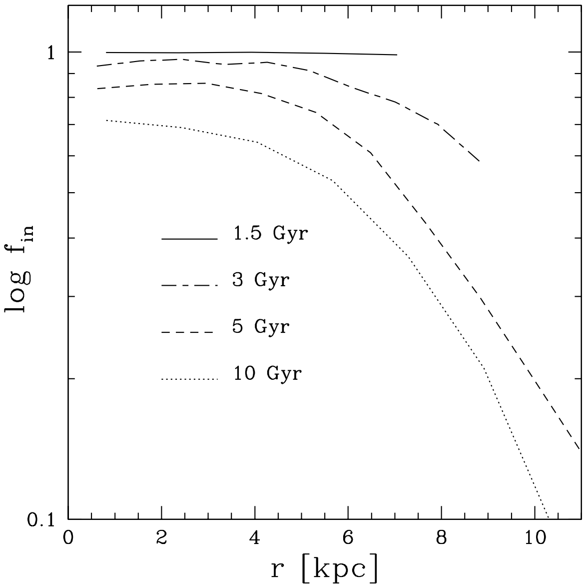

Figure 4.4: The fraction of gas originating from the inner sphere of the disk is plotted versus radius at different times. Initially the disk forms only from gas of the inner sphere. Later, more gas has accreted from the outer shell, which then makes up the largest part of the outer disk.

4.5 Generating warps by intergalactic accretion flows via mergers

What is lacking in model A is the observation of asymmetric warps. Model B on the other hand, where the infall of matter is due to an infalling halo, showed asymmetric warps. In the centre of the third halo a cold blob of gas starts to form (this halo has no internal angular momentum and therefore a disk does not form, the mass of the cold blob after 4 Gyr is of order 40% of the disk mass) and while approaching the disk, the blob orbits one time around the disk. While approaching, the third halo, which is carrying angular momentum to the initial halo, produces asymmetric torques (Figure 4.9) on the disk. Those torques give rise to an oscillating and often asymmetric warp. 3 Gyr after the start of the infall of the third halo the blob has passed near the disk (minimal distance of the blob to the disk $\sim$ 20 kpc) and the warp has developed for the first time an asymmetric L-shape, changes its shape back to an S-shaped warp later and the L-shape becomes prominent again after 4 Gyr, see Figure 4.11. Tidal forces due to the quite massive blob influence the disk as well, but are hard to separate in that situation. The Fourier decomposition of the phase of particles in the disk plane and of their vertical positions (Sparke & Sellwood 1987) shows that the dish-shaped $m = 0$ mode dominates the excitations for radii bigger than 6 kpc. But also the integral-sign-shaped $m = 1$ and (less important) saddle-shaped $m = 2$ mode contribute considerably (see Figure 4.10). At that time the disk consists of less than 1% of gas particles of the third halo. The description of an asymmetric warp is not possible using Briggs diagrams as before, because the calculation of the specific angular momentum vector is averaging over the concentric rings around the centre. Instead we

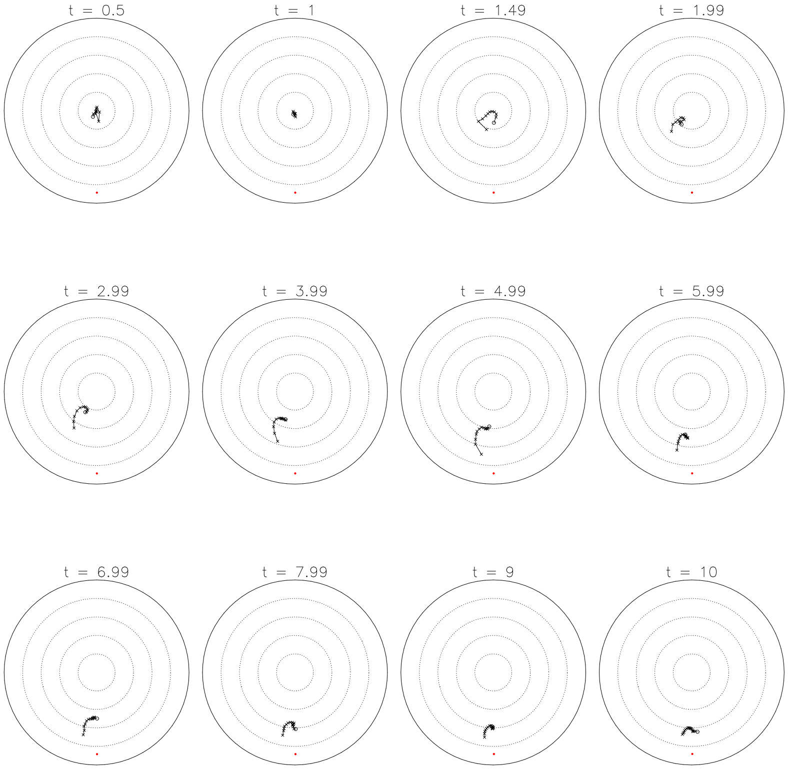

Figure 4.5: A series of Briggs diagrams for model Ac is plotted versus time (from 0 to 10 Gyr). The leading spiral (relative to the sense of rotation of the disk) is as observed galaxies. The red dot indicates the direction of the total angular momentum vector of the gas. The dotted circles are at 10 degrees separation and the outer solid circle is at 50 degrees. Rotation of the disk is counter-clockwise, so the spiral line-of-nodes which develops is leading.

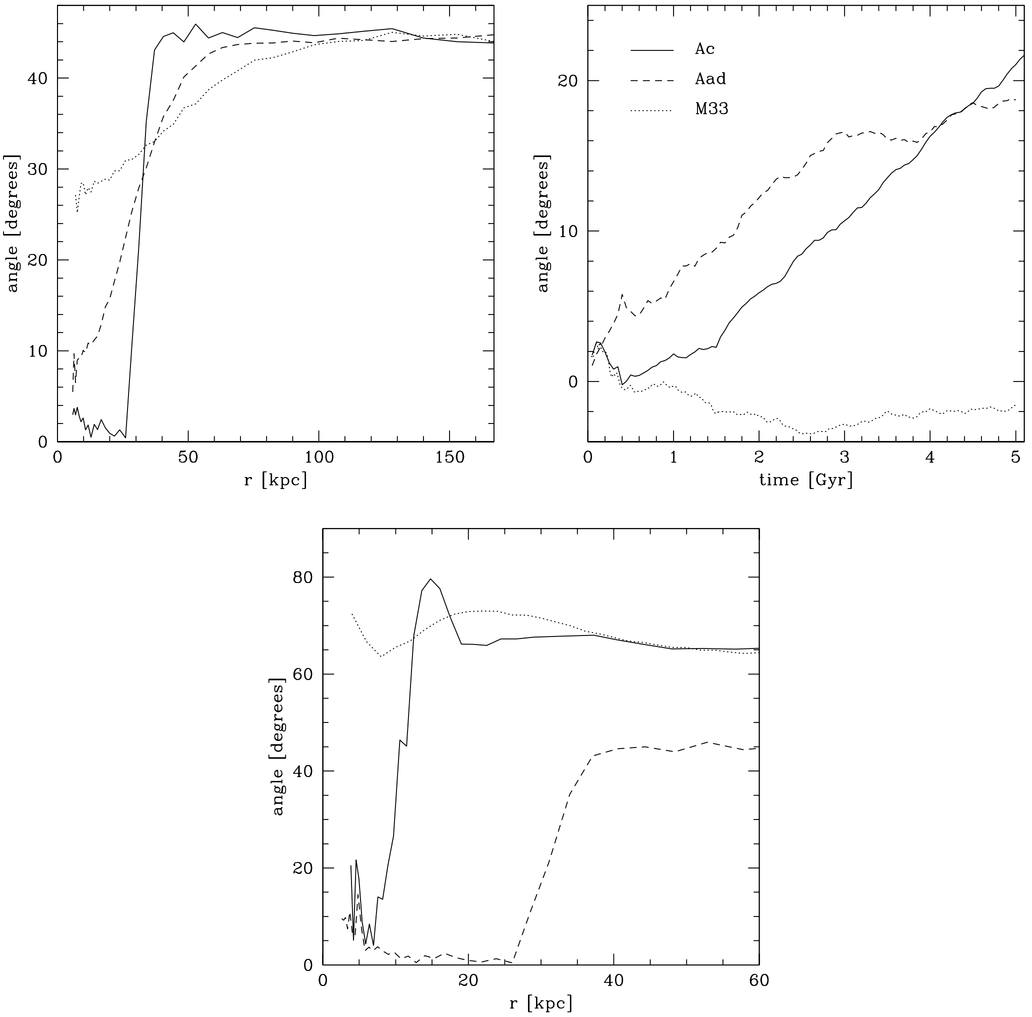

Figure 4.6: Left panel: The angle between the angular momentum vector of the gas and the z-axis is plotted versus radius, model Ac (solid) and Aad (dashed). These angular distributions are the initial conditions for the cooling phase in the two different models. The dotted line shows model Aad after 9 Gyr of adiabatic evolution. Right panel: The time evolution of the angle between the angular momentum vector of the cold gas disk and the z-axis is plotted, model Ac (solid) and Aad (dashed). The collapse of material of the inner sphere ($r < 30$ kpc) in model Ac leads to an angular momentum vector which is parallel to the z-axis in the first two Gyr (as expected). We plot as comparison the "M33" run from Kaufmann et al. (2006a), where the angular momentum vector of all the gas was initially aligned. Lower panel: As in the upper left plot, the angle between the angular momentum vector of the gas at a given radius and the z-axis is plotted versus radius. Model B, but using an adiabatic equation of state all the time, is plotted after 5 Gyr after including the third halo (solid lines) and after 10 Gyr (dotted lines), and as comparison the IC of model Ac (dashed). This merger model motivates the initial angular momentum distribution in model Ac and gives also the timescale in which an angular momentum vector with a single direction can develop.

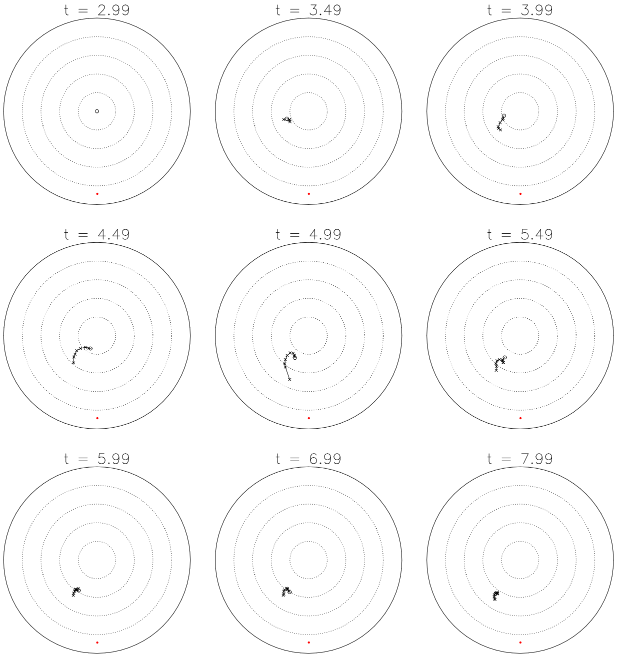

Figure 4.7: A series of Briggs diagrams for model Aad (which has been adiabatically relaxed for the first 3 Gyr) is plotted versus time (from 0 to 5 Gyr; note, that the times quoted in the plot refer to the start of the simulation, the cooling phase starts after 3 Gyr). The warp is smaller than in model Ac .

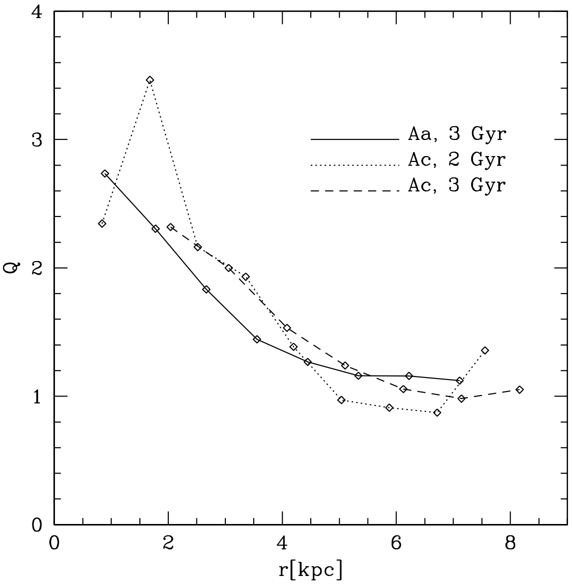

Figure 4.8: Plot of Toomre parameter Q for models Ac (before and after warp formation) and Aad. The Toomre parameter stayed above 1 for both models. The times quoted in the plot refer to the start of the cooling phase.

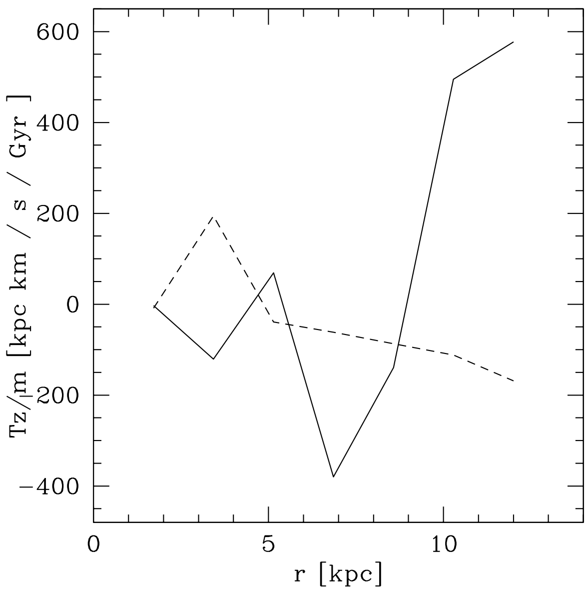

Figure 4.9: Plot of the torques on the disk in model B versus radius after 4 Gyr. The torques are calculated with respect to the center of mass of the inner disk. The torques on the disk-side closer to the infalling halo is plotted with solid lines, whereas torques on the far side are plotted with dashed lines.

use in Figure 4.12 a measurement of the mean height above the centre of mass of the disk plotted versus ϕ, the polar cylindrical coordinate. This is done for different concentric rings around the centre. For a symmetric warp a sine curve like shape is expected whereas we find a clearly asymmetric behaviour for the outer rings. The maximum deflection of the warp closer to the satellite is ≈ 1 kpc above the midplane at a distance of ≈ 12 kpc from the centre of the disk. This value is close to the one actually measured for the Milky Way (Burton 1992).

After 4.2 Gyr the very dense blob of third halo starts to penetrate the disk which warps one side of the disk even stronger in the first place, but the re-infall of the blob disturbs then the disk shape considerably, leading to the destruction of the regular disk shape in less than 0.1 Gyr.

The models using less massive satellites, B5 and B10, carry less angular momentum to the system and excite weaker warps later. Their satellites are spiraling in on different orbits and therefore on a longer timescale compared to model B. After 5 Gyr model B5 led to symmetric U- and S-shaped warps, see Figure 4.13, whereas for model B10 6 Gyr were needed to warp the disk slightly (S-shaped warp). Asymmetric warps are observed in model B10 as well: a close passage (minimal distance of the blob to the disk ~ 3 kpc) of the infalling halo is exiting a structure looking like a lopsided warp 6.5 Gyr after the start of the infall. The face-on view in Figure 4.13 reveals that the warp seen edge-on is due to an spiral-arm, which has been bended by tidal forces of the infalling satellite. Due to the significantly shallower potential in the B10 model, the gas of the infalling satellite looses its spherical symmetry inside the dark halo. Some gas gets stripped and cools in lumps faster than the average gas.

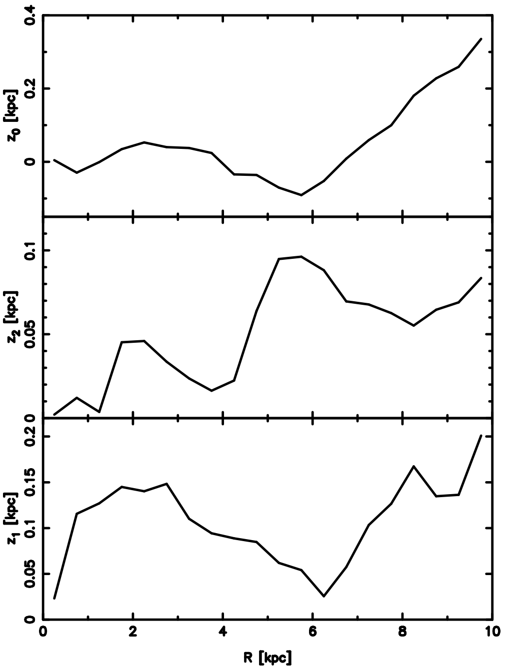

Figure 4.10: Plot of the lowest vertical harmonics of the disk in model B versus radius after 4 Gyr. For radii bigger than 6 kpc the $m = 0$ mode dominates the signal.

In short, in the B and B5 models oscillating warps are observed over a timescale of more than one Gyr; in the B10 model, however, a close passage of the central blob is needed to excite a warp-like looking structure for a shorter time. In all the B models the disk is tilting away from its initial alignment due to the infall of the satellite, the tilting angle for e.g. the B model is of order 30 degrees. In observations it has been found that the presence of lopsidedness seems to be related to the presence of nearby companions (García-Ruiz et al. 2002).

The infall of the dark satellite , the Bdark model, excites only a weak warp, the tilting of the disk remains comparable to its parental model B. The reason for this difference is, that with model B we follow the infall of dwarf galaxy (modeled by the blob, which is barely not influenced by tidal forces), whereas the (low-concentrated) dark satellite is easily deformed and also stripped by tides. Although the two satellites have the same mass, the structure of those two systems and therefore their impact on the disk is different.

4.6 Summary and Discussion

We present self-consistent models for the formation of galactic disks where we followed their warping due to gas and dark matter infall using SPH simulations. The scenario uses infalling gas with different angular momentum compared to the disk at its beginnings. This gas can cause either long-lived warps due to accretion of the gas from the outer halo to the disk (model A) or variable and also asymmetric warps (model B) due to torques and tidal forces from the infalling halo on the disk. Tidal excitation (as in Weinberg & Blitz 2006) is also linked to the infall of this satellite in model B, but is hard to disentangle. However, the B10 model was not able to excite a structure looking like a lopsided warp until the

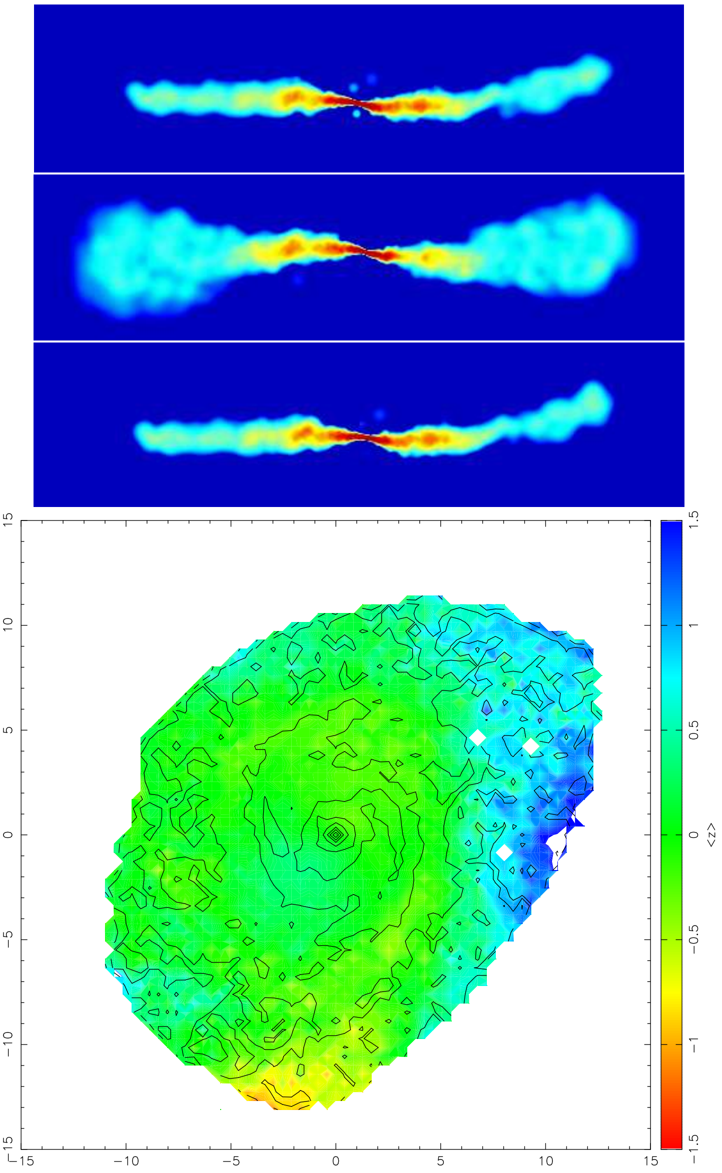

Figure 4.11: Edge-on density maps of gas in a slice through the centre of Model B. From top to bottom: model B after 3, 3.5 and 4 Gyr after adding the third halo (box length 30 kpc). The warp of model B is oscillating. The last panel shows the disk face-on, again after 4 Gyr. The elevation above the mid-plane is shown color-coded (numbers are given in kpc).

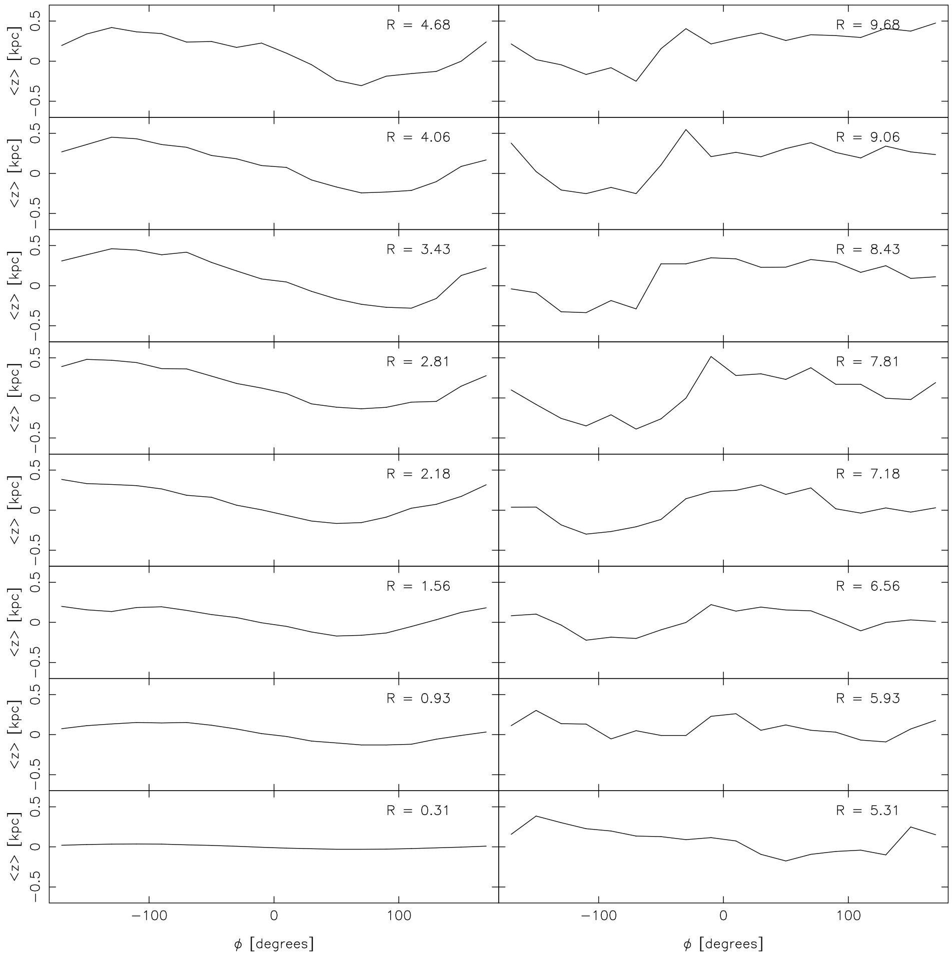

Figure 4.12: Measurement of the mean height above the centre of mass of the disk plotted versus ϕ, the polar cylindrical coordinate. The disk is decomposed into a series of concentric rings whose radii are indicated in the individual panels. The plot is showing Model B 4 Gyr after adding the third halo, the asymmetry becomes distinctive for $R > 7.5$ kpc.

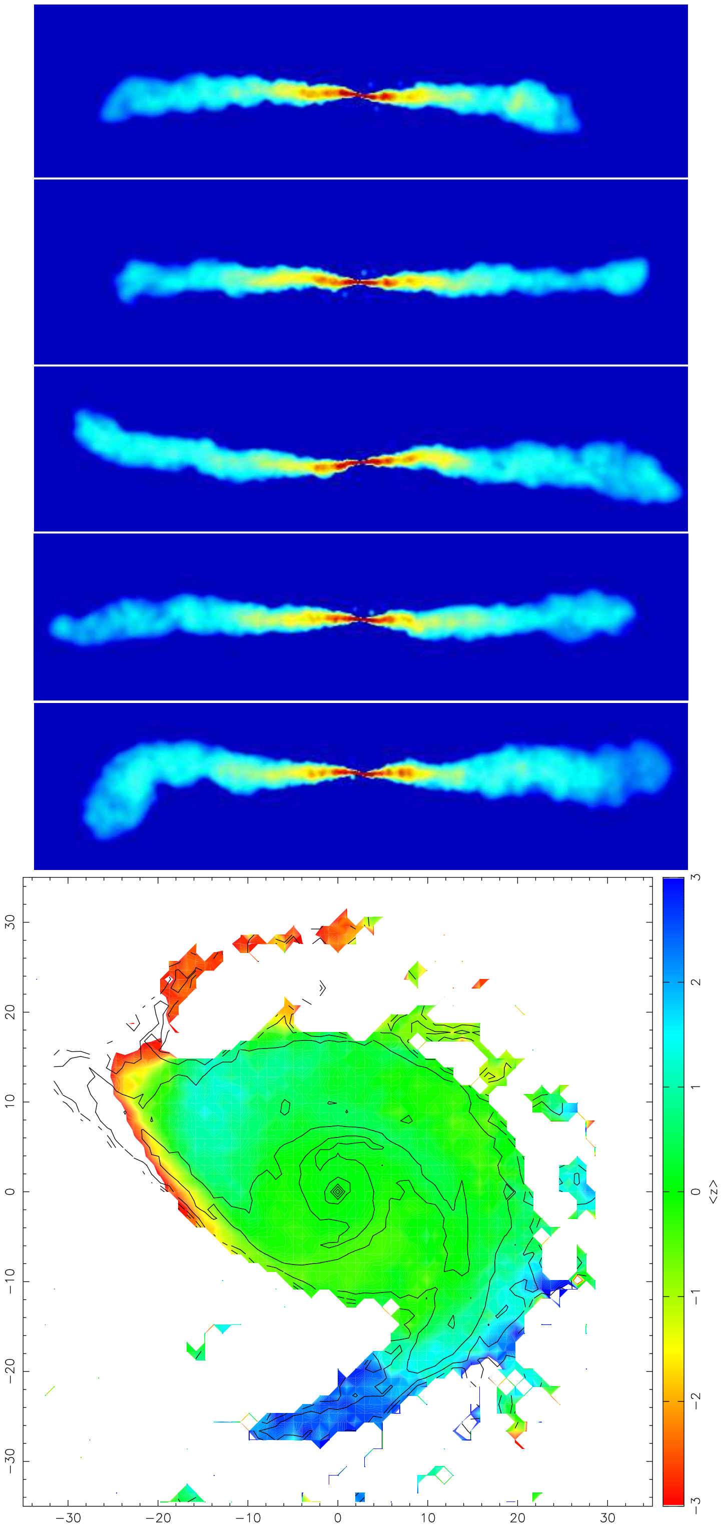

Figure 4.13: Edge-on density maps of gas in a slice through the centre of the gas disk of Model B (box length 45 kpc). From top to bottom: B5 with a U-shaped warp and B10 without warp after 4 Gyr after adding the third halo, then B5 after 5.1 and B10 after 5 Gyr both with S-shaped warps. The last edge-on panel shows B10 after 6.5 Gyr with an asymmetric warp whereas the bottom panel shows the B10 disk face-on at the same time. The elevation above the mid-plane is shown color-coded (numbers are given in kpc).

infalling halo passed by the disk in its vicinity (much closer than e.g. the Large Magellanic Cloud to the Milky Way). Cosmic infall is expected to produce more naturally tilted rings, an $m = 1$ feature and the vertical $m = 2$ mode requires several inflow directions (Weinberg & Katz 2006). We found exactly this behaviour in model A, where S-shaped warps are excited for constant infall directions, and the varying inflow directions of model B led to $m = 2$ modes and lopsided warps. A pure dark satellite tilts but does not warp the disk considerably, based on those results we expect that realistic dark satellites (i.e. with circular velocities of order 50 km/s or less) do not warp a large disk at all, but are tidally disrupted.

Whereas the initial set-up for model A is somehow artificial (but can motivated by the adiabatic evolution of model B in addition to gas-inflow along filaments), run B is modeling an late phase of an cosmological simulation. The interaction of the disk with a companion does nicely explain the appearance of asymmetric warps and those are the first asymmetric warps seen and analysed in a SPH-simulation. Isolated galaxies with asymmetric warps would still be unexplained. However, recently there were found some companions for galaxies which had been thought to be classical examples for isolated galaxies (e.g. NGC 5907, Shang et al. 1998) and the picture of isolated galaxies must probably be revised. We found that the the 10:1 merger warps the disk only over a small fraction of the Hubble time. Given the quite small fraction of bigger satellites alternative ways to warp disks (e.g. Dubinski & Kuiken 1995) may therefore play its role as well.

In the future it should be possible to simulate galaxies in cosmological simulation with such high precision that also warp-formation can be studied directly. Until then, these simulations do suggest several linked mechanisms how infalling gas can generate warps of galaxies.

Acknowledgments

We would like to thank Stelios Kazantzidis for providing a code to generate isolated dark matter haloes. We acknowledge useful and stimulating discussions with Yves Revaz and Lucio Mayer. The numerical simulations were performed on the zBox2 (http://krone.physik.unizh.ch/∼dpotter/zbox2) supercomputer at the University of Zürich.

Chapter 5

Constraining the spin of the hot halo of the Milky Way

5.1 Abstract

We use gravitational/hydro-dynamical simulations of the formation of the Magellanic Stream (MS) and its interaction with the hot gas halo of the Milky Way to constrain the spin of the hot halo of the Galaxy. We model the gaseous halo of the Milky Way using different spin-parameters. As the Large Magellanic Cloud spirals inward towards the Galaxy, it suffers hydrodynamical stripping and the MS forms. The curvature of the MS depends strongly on the spin parameter of the hot gaseous halo. The model with $\lambda = 0.05$ produced a stronger deflection deflection than observed in the data, constraining the spin of the present-day hot halo to be smaller than 0.05. This indicates that the Milky Way is a spiral galaxy with a spin close to the average.

5.2 Introduction

Within the current paradigm of galaxy formation realistic rotationally supported disks as the Milky Way can form if the gas retains the angular momentum gained from tidal torques as it cools within a cold dark matter (CDM) halo (White & Rees 1978; Mo, Mao & White 1998). The presence of an extended hot halo surrounding the Milky Way and in hydrostatic equilibrium within the dark matter potential is expected by current models of hierarchical structure formation (White & Frenk 1991, Maller & Bullock 2004). This gaseous halo, left over from the initial collapse, would be continuously fueled by accretion of satellite galaxies over time. Recent observational results have confirmed the existence of a distribution of hot ($T < 10^6$ K) gas well beyond the Galactic disk, with a radius larger than 70 kpc in order to explain some ionisation features discovered in the Magellanic Stream (MS) (Sembach et al. 2003; Putman et al. 2003). Dynamical and thermical arguments can then constrain the density of the halo in a range between 10^{-5} and 10^{-4} cm^{-3} at the Large Magellanic Cloud (LMC) distance from the Galactic Center. The MS is a trailing filament of neutral hydrogen that originates from the Magellanic Clouds and stretches over $\sim$ 100 degrees in the Southern Sky and is the most prominent signature of an interaction between the Clouds and the Milky Way (MW). Two primary scenarios have been postulated to explain the origin of the MS: (i) ram pressure stripping of LMC and the Small Magellanic Cloud (SMC) gas due to the motion of the Clouds trough the tenuous coronal gas in the Galactic halo (Moore & Davis 1994; Mastropietro et al. 2005) and (ii) tidal disruption of the SMC (e.g. Murai & Fujimoto 1980; Connors et al. 2005). The clouds in the MS are subjected along their orbits to the ram pressure generated by the distribution of hot gas and the Magellanic System itself seems to be the result of a complex interaction that involves both hydrodynamical and tidal processes (Mastropietro et al. 2005). Recently, ram pressure stripping has also been proposed to explain tails of gas behind spiral galaxies moving through the intra-cluster medium. Those simulations have used adaptive mesh refinement techniques (Roediger et al. 2006).

In this chapter we do not focus on the actual mechanisms which removed gas from the Magellanic Clouds but we concentrate on the influence of the hot halo onto the clouds of the MS. The aim of this work is to constrain the spin of this hot halo using the MS as a tracer: a spinning hot halo should drag the material which is left well behind the LMC and the stream should be curved. We use several models of a Milky Way halo where the hot gas is spinning differently and measure the amount of deflection this spinning hot gas produces on the MS. Therewith we can constrain the spin of the hot halo.

The outline of the chapter is as follows. In section 5.2 we describe the modeling of our initial conditions, and the code which has been used. In section 5.3 we present the results of the simulations where the MS forms and interacts with the Galactic halo. We then discuss the deflection of a well-resolved cloud due to the hot halo and its dependence on its over-density (section 5.4). We summarise and conclude in section 5.5.

5.3 Initial Conditions

Our initial conditions comprise an isolated equilibrium NFW halo (Navarro et al. 1996; Kazantzidis et al. 2004) with an embedded spinning gaseous mass distribution. The parameters of our models are Milky Way like, i.e., we choose $v_{vir} = 140$ km/s, which corresponds to $r_{vir} = 200$ kpc and therefore and $M_{vir} = 9.14 \times 10^{11} M_{\odot}$ for the dark matter halo. The gaseous halo is constructed in the same way and contributes 9% of the total mass to the system. The temperature structure (in the range of $\sim 10^6 K$) of the gaseous halo is calculated by solving the equation for the hydrostatic balance of an ideal gas inside a dark matter halo, details are given in Kaufmann et al. 2006b, where we use these models to simulate the formation of a (realistic) Milky Way like galaxy using gas cooling. The hot gas starts with a specific angular momentum distribution motivated by the results of cosmological simulations; the initial angular momentum profile is well fit by a power law following $j \propto r^{1.0}$, whereas the dark matter halo has no angular momentum for simplicity. Bullock et al. (2001) proposed a power law with $j(r) \propto r^{\alpha}, \alpha = 1.1 \pm 0.3$. We used a wide range of values for the spin parameter λ , the latter being defined as $\lambda = \frac{j_{gas}|E|^{0.5}}{GM^{1.5}}$, where j_{gas} is the average specific angular momentum of the gas, G is the gravitational constant, E and M are the total energy and mass of the halo, respectively. This definition matches the one commonly used (e.g. Mo, Mao & White 1998) under the assumption that there is no angular momentum transport between the spherical dark matter halo and the gas. The only difference in the various models we run is the value of the spin parameter, models S1, S2, S3 and S4 have a spin of 0.01, 0.03, 0.05 and 0.085, respectively. The initial angular momentum vector is parallel to the z-axis of the system.

The mass of dark matter particles is $1.66 \times 10^5 M_{\odot}$ in the inner part of the halo, we used a halo with variable particle masses, with the resolution increasing towards the center of the system. These shell models comprise: $600,000$ particles distributed in the inner sphere with 20 kpc radius, $300,000$ particles in the next shell out to 100 kpc, while the rest of the halo (out to the virial radius) is sampled with only $100,000$ particles (see Zemp et al. 2006, in preparation). The gas halo is sampled with $500,000$ particles having masses of $2 \times 10^5 M_\odot$. To model the LMC we added to all of these models a dark matter halo with with a peak circular velocity of $v_c = 50$ km/s, where a gas sphere with radius of 10 kpc, temperature of $T = 30,000$ K and density $\rho \approx 0.1\ n_p\ cm^{-3}$ was added. This additional halo is located at (70/0/0) (numbers are given in kpc), where the origin of the coordinate-system coincide with the center of the host halo (and also with the expected Galactic Center of the MW). The LMC halo gets an initial velocity of 168 km/s in the z-direction which corresponds to the circular velocity at this radius. The initial rotation orbit of the LMC is therefore perpendicular to the rotation of the gas in the hot halo. For a non-spinning halo the LMC is expected to orbit around the center in the x-z-plane. The gas of the LMC is represented with $48,000$ particles. We do not include a realistic disk for the LMC because the only aim of it is to provide a stream of stripped gas. The density of the hot gas in the host halo is $\rho \approx 3 \times 10^{-4}$ cm^{-3} at a distance of 70 kpc of the Galactic center, which is over-estimating a bit the observational limits. To test the dependence of the model on the gas-density we run model S4 as well with a three times lowered initial gas-density (named S4lg) by lowering the mass of each gas-particle by a factor 3.

In an additional set of test simulations we added instead a single cloud at the same position as the LMC to the Milky Way S4 halo. The cloud is initially in pressure equilibrium with the hot halo, its radius was 4 kpc and it was ten times denser than the host halo at that position (i.e., $\rho_c \approx 0.003\ n_p\ cm^{-3}$, $T_c = 117,000$ K). The cloud has initially the same velocity as the LMC (model CvelS4) or was at rest (model CS4). To check the dependence on density we run corresponding cloud models inside the lowered gas-density halo S4lg: C10velS4lg and and C30velS4lg, where the clouds were ten and thirty times denser than the host halo, respectively. Note, that the cloud in the C30velS4lg model has the same density as in CvelS4. Adopting e.g. the values of Putman et al. (2003) for the column density for the third cloud region MS III ($N_{H\,I} = 2.5 \times 10^{19}\ cm^{-2}$), distance of $R = 55$ kpc and assuming a diameter corresponding to 10 degrees, we get for the cloud density $\rho_c \approx 8 \times 10^{-4}$ cm^{-3}. Those numbers are well modeled with the cloud simulation C10velS4.

To evolve the models we use the parallel TreeSPH code GASOLINE, which is described in Wadsley, Stadel & Quinn (2004). The code is an extension to the pure N-Body gravity code PKDGRAV developed by Stadel (2001). GASOLINE can handle dark matter, gas and stars. It employs an artificial viscosity which is the shear reduced version (Balsara 1995) of the standard Monaghan (1992) artificial viscosity. GASOLINE solves the energy equation using the asymmetric form and conserves entropy closely. It uses the standard spline form kernel with compact support for the softening of the gravitational and SPH quantities.

5.4 Stream simulations

The models S1 to S4 and S4lg were evolved with an adiabatic equation of state (EOS), some of the gas is stripped quite quickly from the LMC halo and has formed after roughly

2 Gyr a stream resembling closely the observed stream, see Figure 5.1 and 5.2. Within 2 Gyr the LMC looses roughly 10% of its gas to the stream and the LMC itself reaches a position very comparable to observed one. The simulated stream is much longer than the observed one, it reaches more than 400 kpc of length, following very roughly a great circle around the Galactic center. The stream is slightly wider than the observed one, similar as found in Roediger et al. (2006). Those authors propose that the inclusion of mechanisms such as thermal conduction and physical viscosity (both missing in their and our simulations) would narrow the stream.

For the S4lg model, the absolute amount of stripped gas, $\sim 1.9 \times 10^8 M_\odot$ in the observed region, agrees quite well with the values measured by Putman et al. 2003 ($\sim 2 \times 10^8 M_\odot$). 45 degrees or equivalent 40 kpc behind the LMC the overdensity of the stream compared to the halo is of order 5, farther at 300 kpc it has dropped down to 2. Those values are roughly comparable with the values found in observations and used for the C10velS4lg cloud simulation. For the the S1 to S4 simulations the absolute amount of stripped was bigger. However, we are neither particularly interested in the shape of the LMC nor the mass of the stream but in its curvature. The gas in the stream is deflected from the orbit of the LMC due to the spinning hot gas halo. As expected, bigger spin leads to a bigger deflection, see Figure 5.3. The spinning halo can deflect the stream in plus and minus y-direction depending on the respective position of the stream. This is visible in Figure 5.3, where particles close to the LMC are deflected in the other direction than those which were stripped at earlier times. The deflection of the data (center of MS II, MS III and MS IV, Putman et al. 2003) is calculated assuming a distance of 50 kpc from the Sun and a best fit great circle through the Bridge between LMC and SMC and MS I. The error-bars account for the uncertainty in the distance (a range from 20 to 80 kpc is covered), the error in the fit of the great circle has not yet been quantified. We argue that the projections presented in Figure 5.1 are more valuable until there are better constraints on the distances. The deflection for the model S4lg with lower gas-density remained comparable as in model S4, see Figure 5.3. The uncertainties in density in the outer halo seems not to affect the results too much. Comparing the deflection with the shape of the observed Magellanic stream (which has nearly no curvature), one can constrain the spin parameter of the halo to smaller than in model S3, i.e., $\lambda < 0.05$ (Figure 5.1).

Due to resolution limits the stream does not consist only of well resolved cloud as it is observed but also single particles are forming the stream. While the gas in the stream is deflected by the halo, the stream particles get heated by the halo particles. One might be worried that resolved warm clouds in pressure equilibrium with the hot halo would respond differently to the spin of the halo than the measurements presented here, where especially the gas stream stripped at the beginning consists of single particles. To test this we used the different clouds models: If a single warm cloud is dragged by the hot halo in a similar fashion as the particles in the stream, the results presented above should be trustworthy.

5.5 Cloud simulations

We evolved the cloud models with an adiabatic EOS to investigate the influence of the hot halo to a warm cloud in pressure equilibrium. For the models with a cloud-overdensity of ten, it turned out, that the cloud was dragged quite efficient from the hot halo. Within

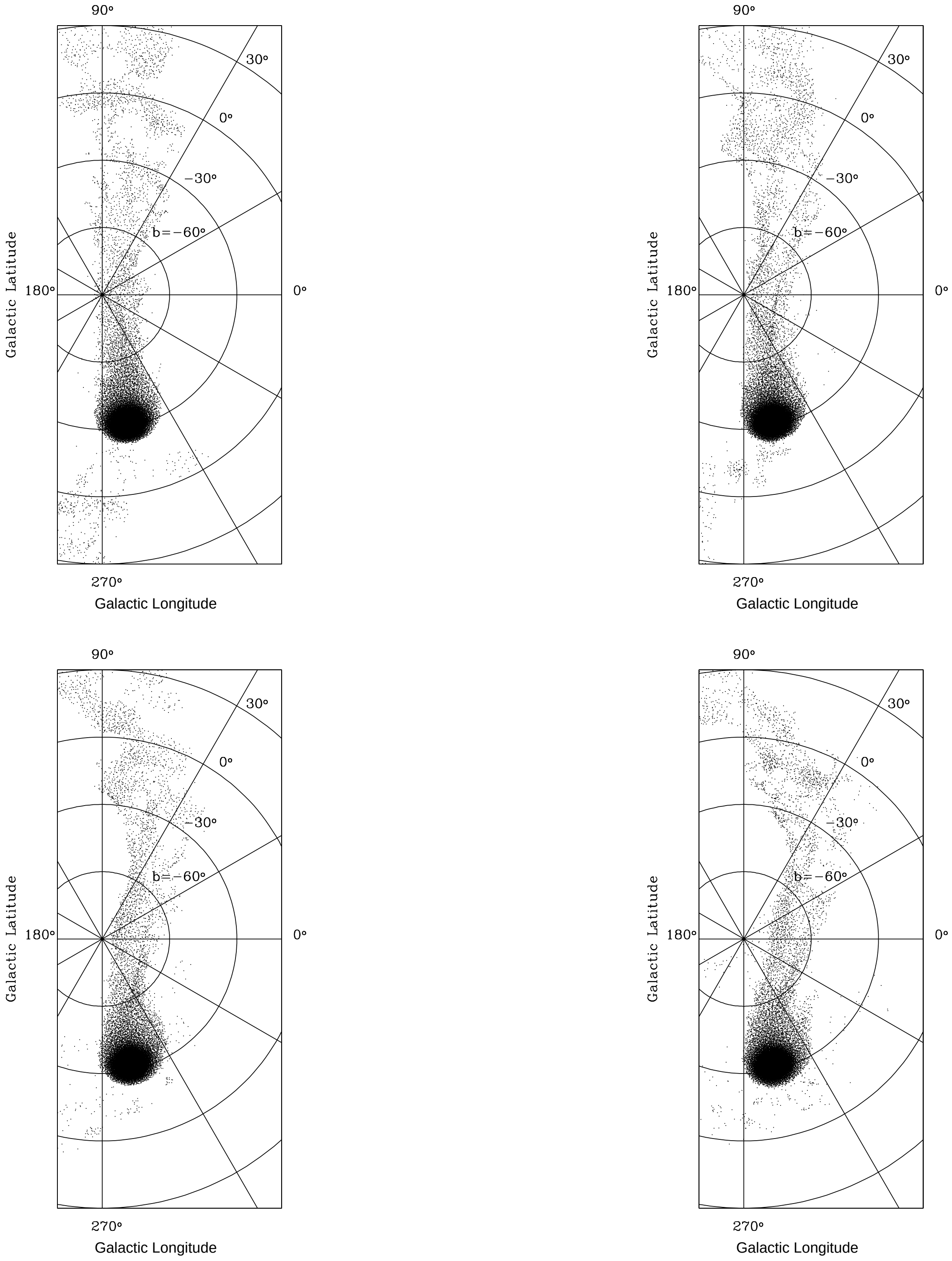

Figure 5.1: Polar projection of the simulated Magellanic Stream in Galactic coordinates, from top left to bottom right: model S1, S2, S3 and S4 are plotted. The dependence of the deflection on the spin parameter is apparent.

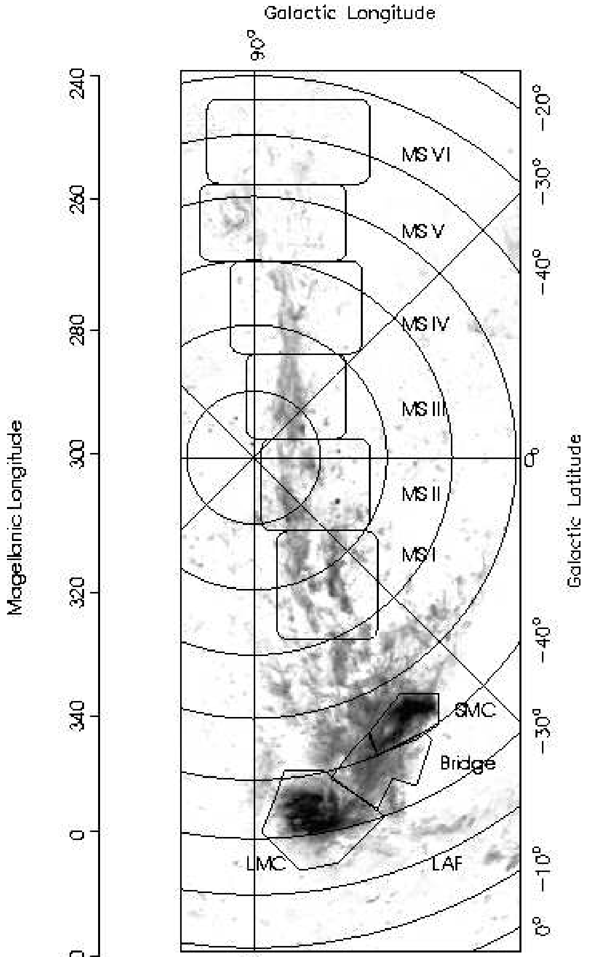

Figure 5.2: The observed Magellanic Stream (Putman et al. 2003) in the same projection as in Figure 5.1. The observed deflection is smaller than in model S3.

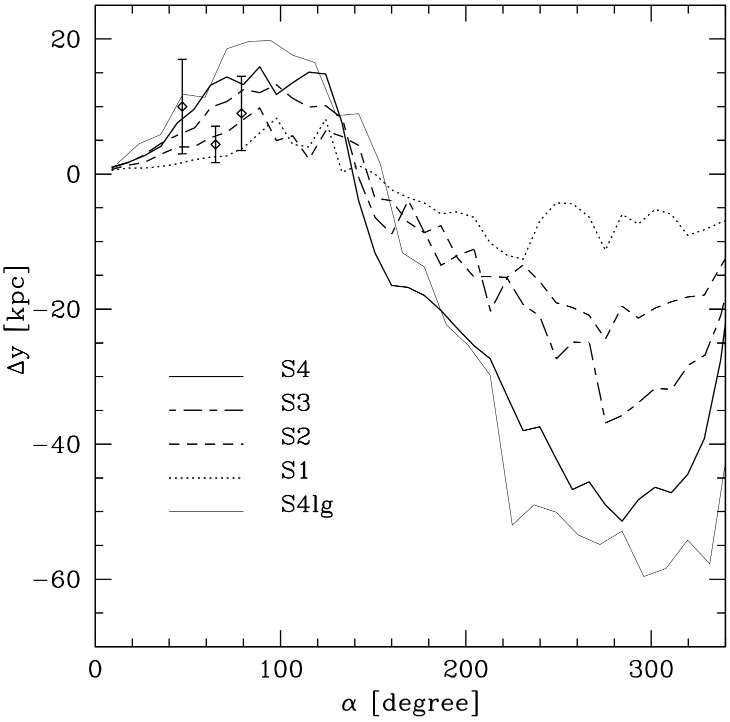

Figure 5.3: The median of the deflection in y-direction (deviation from the initial great circle) of the stream is plotted versus the angle α between $\mathbf{r}_{LMC}$ and $\mathbf{r}$ of the respective bin. The bigger this angle the earlier this gas was stripped. This measurement was done after 2.25 Gyr of evolution. The points with error bars are data from Putman et al. (2003), see text for details.

0.4 Gyr the cloud reaches a velocity due to the drag of $v_y > 30$ km/s and gets deflected up to ≈ 20 kpc (Figure 5.4). The over-densities in the stream simulations did not exceed that value. The C30velS4lg model showed qualitatively the same behaviour, however, due to the bigger overdensity it took its cloud slightly longer to reach a velocity of $v_y > 30$ km/s and it got therefore less deflected. This is expected, because acceleration due to the ram pressure in that situation is proportional to the ratio of the densities cloud - halo. Later the cloud enters the other side of the spinning halo and gets decelerated, due to the compression it gets hotter as well. The clouds stays pressure confined more than one Gyr, later, ram pressure stripping starts to remove some gas from the cloud. The results do only depend weakly on the initial velocities, see Figure 5.4. The respond to the halo is qualitatively comparable to the stream simulation S4. One might be worried that clouds with very high over-densities would be less deflected than the stream clouds presented in the last section. However, the region which is of interest for our study, namely the part of the stream far away from the LMC, seems to consist of low-density gas-filaments (Putman et al. 2003) and the models presented here should apply.

5.6 Summary and Discussion

We have carried out gravitational/hydro-dynamical simulations of the formation of the MS and its interaction with the hot gas halo of the Milky Way. As the LMC spirals inward towards the Galaxy, it suffers hydrodynamical stripping and the MS forms from stripped material. The curvature of the MS depends strongly on the spin parameter of the hot gaseous halo. The model with $\lambda = 0.05$ produced a slightly stronger deflection than observed in the data whereas the models with spin $\lambda = 0.03$ and lower are compatible with the measurements. This constrains the spin of the present-day hot halo to be smaller than 0.05. However, gas accreted early on (i.e. earlier than before 2 Gyr) might have had different spin. We found for the S4lg model roughly the same amount of gas in the stream as in observations and we have shown, that the model S4lg and S4 deflect the clouds in the same fashion. Well-resolved cloud show the deflection due to the rotating halo in a similar manner (cloud simulations, section 4). The amount of deflection depends as expected on the ratio between densities of the cloud and the host halo.

One might suggest that an EOS with cooling would be more appropriate for studies as presented above. However, it has been argued, that for such kind of models an adiabatic EOS as we used is closer to reality than a EOS with cooling, unless the multiphase interstellar medium is modeled properly (Mastropietro et al. 2005). For that, the inclusion of e.g. supernovae feedback would be necessary. If the real clouds would be much denser objects than those we followed in our simulations, we expect a smaller degree of deflection. In that case the spin of the hot halo could be higher. The spin parameter λ is a global measurement of the angular momentum content of a halo, haloes with various angular momentum profiles can have the same spin parameter. For our set of simulations we used an angular momentum distribution motivated by cosmological simulations, but our results for the spin parameter may change if the angular momentum profile of the hot halo of the Galaxy deviates considerably from $j(r) \propto r^{\alpha}, \alpha \approx 1$ in the region of the orbit of the LMC.

Tonini et al. (2006) found a mean of $\lambda \approx 0.03$ for spiral galaxies. If the Milky Way has formed via accretion of gas from a halo matching our assumptions, then this excludes the Milky Way being a spiral galaxy with untypical high spin.

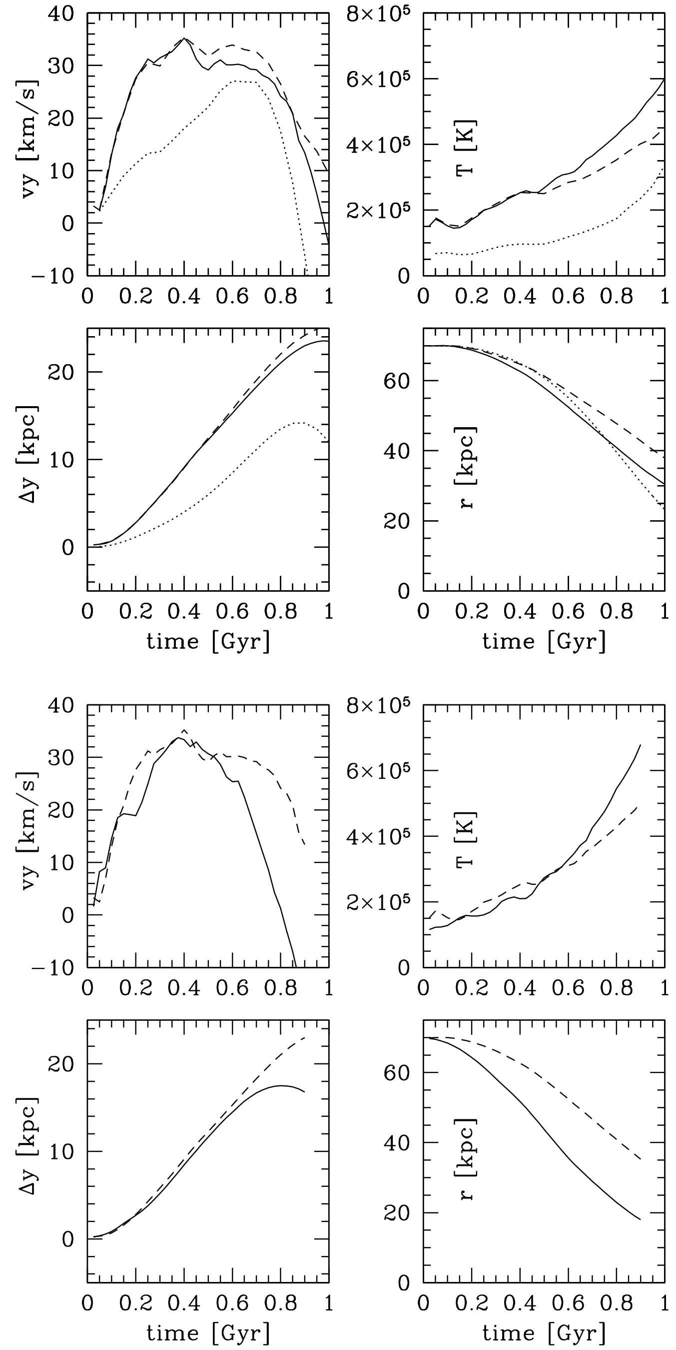

Figure 5.4: The time-evolution of v_y, Temperature, deflection Δy and distance from the center for the cloud simulations is plotted. The spinning hot halo is deflecting the clouds from their orbits. Upper plot: The cloud models comparing different densities: CvelS4 (solid lines), C30velS4lg (dotted lines) and C10velS4lg (dashed lines). Lower plot: comparing different initial velocities: CS4 (solid lines), CvelS4 (dashed lines). The decreasing radii in the two lower left panels are due to the gravitational forces (without initial velocity the cloud falls in more or less radially).

Acknowledgments

We would like to thank Mary Putman for making the data of the Magellanic Stream available and Stelios Kazantzidis for providing a code to generate isolated dark matter haloes. We acknowledge useful and stimulating discussions with Lucio Mayer. The numerical simulations were performed on the zBox (http://krone.physik.unizh.ch/∼stadel/zBox) and zBox2 (http://krone.physik.unizh.ch/∼dpotter/zbox2) supercomputer at the University of Zürich.

Chapter 6

Concluding remarks and outlook

In this thesis, I have studied a number of related aspects occurring in the theory of galaxy formation in a universe dominated by cold dark matter. This framework - the ΛCDM model - is the current standard cosmological model, which has been remarkably successful in explaining most of the properties in the universe. Its predictions agrees with many observations of both the nearby universe and of the early universe as seen in the cosmic microwave background. An important paradigm of that model is the concept of hierarchical galaxy formation: galaxies form bottom-up, with small galaxies being born first. A hierarchy of merging processes then leads to the build-up of more massive galaxies. Mergers of galaxies are believed to be frequent in that model, the massive elliptical galaxies are formed in that framework by mergers of large disk galaxies as e.g. the Milky Way and the Andromeda Galaxy.

Although the ΛCDM model has been very successful at large scales, on non-linear scales as galaxy formation several outstanding issues remain unresolved. One of the important open questions is, how the formation of disk galaxies can be explained. The failure of cosmological numerical simulations to form disk galaxies looking closely as observed ones (i.e. with scale lengths of reasonable size, without a bulge and a surface density profile well fit by an exponential over several scale lengths) has raised the question, if there is a fundamental problem in the CDM paradigm. The failure has been attributed to missing physics, resolution, or to the nature of the dark matter. In addition, the internal structure of galaxies is still barely resolved in cosmological simulations; this and the high intrinsic complexity of cosmological simulations render the task of identifying numerical artifacts extremely hard.

Addressing theses questions requires much better resolution than is achievable in current cosmological simulations. We have therefore decided to investigate the formation and evolution by performing high-resolution simulations of isolated systems. The model we adopt assumes initially spherically symmetric haloes, made of baryonic and dark matter. From that starting assumption we perform self-consistent simulations, where for all interaction between gas and dark matter is accounted.

In chapter 2 we employ such models to investigate how various numerical effects can compromise the outcome of simulations of galaxy formation. We find, that the disk morphology and radial profiles depend sensitively on force and mass resolution. We discover significant numerical angular momentum loss at resolutions used in current cosmological simulations, primarily due to spurious hydrodynamical torques transferring angular momentum to the hot phase. At higher resolution, gravitational torques dominate. With millions of gas particles we are left with physical angular momentum transport due to spiral patterns and bars and a residual loss of 10–20%. This resolution will be hard to reach for cosmological simulations, and we expect numerical effects to be important in cosmological simulations for quite a long time.

In chapter 3 we discuss another result, which depends sensitively on resolution. We used again an isolated halo model to follow the formation of a galaxy similar to the Local Group spiral M33 with unprecented resolution, mass-scales of order a few hundred solar masses in the gas component were resolved for the first time. Thermal instabilities result in the formation of numerous warm clouds that are pressure confined by the hot ambient halo gas. The rotational velocity of the infalling cold gas decreases as a function of height above the disk is very similar to measurements of the extra-planar gas recently observed around the spiral galaxy NGC 891.

We have shown in chapter 2 and 3 that changing results in cosmological simulations are expected, as soon as comparable resolution as in our simulations is reached: Gas is anticipated to accrete to the galaxies as warm clouds as well as directly from the hot halo (and along filaments via cold accretion, see Kereš et al. 2005). If numerical angular momentum loss can be limited, then the scale length of disks will become bigger and the bulge to disk ratio smaller. There are already first hints for developments in that direction in cosmological simulations (Governato et al. 2006, Sommer-Larsen 2006).

We then investigated the role of accreting gas having different angular momentum compared to the initial disk in chapter 4. We used simulations, where infalling satellite galaxies accrete to the host halo, to show how gas can excite S-, U- and even lopsided warps. Those lopsided warps were the first seen in SPH simulations. Interestingly, a low-concentrated dark satellite with the same orbital parameters as for the two-component system did not produce asymmetric warps as are frequently observed. This excludes the infall of such dark satellites as the primary reason for warped galaxies.

More specifically, we focused in chapter 5 on our Galaxy with one of its infalling satellites, the Large Magellanic Cloud (LMC). Ram pressure stripping removes gas from the satellite while it is spiraling in towards the Galaxy and the Magellanic Stream forms behind the LMC. The stream is deflected by the hot gaseous halo of the Milky Way, depending on the spin of the latter. Using a series of simulations with different spinning gaseous haloes we constrained the spin parameter of the hot halo of the Milky Way to be < 0.05. This indicates that the Milky Way is a spiral galaxy with a spin close to the average.

These investigation into some of the key physical processes that are assumed to be at the core of disk galaxy formation have opened up new interests and directions, for example:

1. The role of multiphase gas cooling model should be investigated in more detail: What is the (physical) origin of the perturbations in the gas halo which start the thermal instability? Can infalling substructure, cold accretion, residual fluctuations of mergers or the galactic fountain provide those? Can the kinematics of the high-velocity gas clouds known to exist in the vicinity of the Milky Way galaxy be explained within these models?

2. The complete simulation of a large spiral galaxy as the Milky Way need robust, resolution independent star-formation and feedback recipes. Our control experiments, spanning a wide range of resolutions allow us to investigate different recipes in detail.

I have implemented a simple star-formation scheme that follows the observed Kennicutt surface H I density criteria. This produces quite nicely the low star-formation rate observed in galaxies like the Milky Way. Very high resolution models including star-formation are particularly important in order to compare with the kinematical and abundance data that will be observed by GAIA. Furthermore, it will allow us to test the effectiveness of Galactic reconstruction via the envisaged large chemical tagging projects that will attempt to uncover the birthplaces and families of the stars in the Milky Way. It reminds us that processes and events at high redshift are responsible for many current observations of the Milky Way. By interpreting local observations within the context of the Cold Dark Matter paradigm, a connection is made with the distant Universe.

3. Although controlled experiments allow us to isolate numerical and physical processes during galaxy formation, it is ultimately desired to form disk galaxies directly using cosmological simulations. Furthermore, it is the goal of computational astrophysics to create not just a single disk galaxy, but to witness the formation of the Hubble sequence directly and to study the formation of groups and clusters of galaxies where we can resolve the morphologies and star-formation histories to dwarf galaxy scales.

At present, there is no alternative theory that comes even close to the ΛCDM model successes, although alternative models as “MOdified Newtonian Dynamics” (MOND) (Bekenstein & Milgrom 1984) have gained some attention recently. We have shown, that the difficulties of former cosmological simulations to build disk galaxies in a ΛCDM universe are clearly linked to insufficient numerical resolution of those simulations. This might be overcome in the future and disk formation might not constitute anymore a problem for CDM. One is tempted to start thinking of a ‘standard model’ for cosmic structure formation.

However, galaxy formation is still far from being ‘solved’, and it is too early to consider hierarchical models as being proven. While the general picture of hierarchical galaxy formation seems to work, this picture is still very crude in many respects. For example, the details of star formation in galaxies or the chemical enrichment of the interstellar and intergalactic media are only poorly understood. At a more fundamental level, one of the most puzzling questions of cosmology: What is the physical nature of the dark matter? This question is also of particular interest for particle physics. One of the most popular candidate for a DM particle is the neutralino from super-symmetric (SUSY) scenarios. Experiments at the LHC at CERN will search for indirect evidence of these particles.

Besides new data from such experiments, there is a huge amount of new astronomical and cosmological observations expected (e.g. new WMAP results, GAIA or LISA) in the next few years. Theoretical models that try to keep up and explain the observations will likely have to include more details on the physical processes. On the other hand computational resources are becoming more powerful than ever. It appears that in future numerical astrophysics will become even more outstanding.

Bibliography

Abadi, M. G., Navarro, J. F., Steinmetz, M., & Eke, V. R. 2003, ApJ, 597, 21

Aarseth, S., Lecar, M. 1975, ARAA, 13, 1

Balsara, D. S. 1995, Journal of Computational Physics, 121, 357

Barnes, J. E., 2002, MNRAS, 333, 481

Bate, M. R., & Burkert, A., 1997, MNRAS, 288, 1060

Bekenstein J. D., Milgrom M., 1984, ApJ, 286, 7

Bennett, C. L., et al. 2003, ApJS, 148, 1

Binney, J., & Tremaine, S., 1987, Galactic Dynamics, Princeton University Press

Binney, J., Jiang, I.-G., Dutta, S., 1998, MNRAS, 297, 1237

Birnboim, Y., & Dekel, A. 2003, MNRAS, 345, 349

Blumenthal G. R., Faber S. M., Primack J. R., Rees M. J., 1984, Nature, 311, 517

Briggs, F. H. 1990, ApJ, 352, 15

Bryan, G., & Norman, M. 1997, in *Computational Astrophysics*, Proc. 12th Kingston Conference, Halifax, Oct. 1996, ed. D. Clarke & M. West (PASP), p. 363

Bullock, J. S., Kolatt, T. S., Sigad, Y., Somerville, R. S., Kravtsov, A. V., Klypin, A. A., Primack, J. R., & Dekel, A., 2001a, MNRAS, 321, 559

Bullock, J. S., Dekel, A., Kolatt, T. S., Kravtsov, A. V., Klypin, A. A., Porciani, C., & Primack, J. R., 2001b, ApJ, 555, 240

Burkert, A., & Lin, D. N. C. 2000, ApJ, 537, 270

Burton, W. B. 1992, in The Galactic Interstellar Medium, ed. D. Pfenniger, & P. Bartholdi (Springer-Verlag, Berlin), 126

Carollo, C. M., 1999, ApJ, 523, 566

Carollo, C. M., Stiavelli, M., & Mack, J., 1998, AJ, 116, 68

Connors, T. W., Kawata, D., Gibson, B. K., 2005, astro-ph/0508390

Corbelli, E., 2003, MNRAS, 342, 199

Couchman, H. M. P., Thomas, P. A., Pearce, F. R. 1995, ApJ, 452, 797

Courteau S. , 1997, AJ, 114, 240

Cox, D. P., 1990, ASSL Vol. 161: The Interstellar Medium in Galaxies, 181

Crampin, D. J., & Hoyle, F. 1964, ApJ, 140, 99

Dalgarno, A., & McCray, R. A. 1972, ARAA, 10, 375

Debattista, V. P., & Sellwood, J. A., 1999, ApJL, 513, L107

Debattista, V.P., Mayer, L., Marcella, C., Moore, B., Wadsley, J., Quinn, T., 2005, astro-ph/0509310

Dekel, A., & Birnboim, Y. 2004, AIP Conf. Proc. 743: The New Cosmology: Conference on Strings and Cosmology, 743, 162

D'Onghia, E., Burkert, A., Murante, G., Khochfar, S., 2006, astro-ph/0602005

Dubinski, J., & Kuijken, K., 1995, ApJ, 442, 492

Efstathiou, G., Lake, G., & Negroponte, J. 1982, MNRAS, 199, 1069

Efstathiou, G., Davis, M., Frenk, C.S., White, S.D.M. 1985, ApJS, 57, 241

Eddington, A. S., 1916, MNRAS, 76, 572

Escala, A., Larson, R. B., Coppi, P. S., & Mardones, D., 2004, ApJ, 607, 765

Evrard, A. E., 1988, MNRAS, 235, 911

Fall S. M., & Efstathiou G., 1980, MNRAS, 193, 189

Fall, S. M., & Rees, M. J., 1985, ApJ, 298, 18

Fraternali F., Oosterloo T., Sancisi R., Swater R., astro-ph/0410375

Fraternali, F., van Moorsel, G., Sancisi, R., & Oosterloo, T. 2002, AJ, 123, 3124

Gerritsen, J. P. E., Icke, V. 1997, A&A, 325, 972

Font, A. S., Navarro, J. F., Stadel, J., & Quinn, T. 2001, ApJL, 563, L1

García-Ruiz, I., Sancisi, R., & Kuijken, K., 2002, A&A, 394, 769

Ghigna, S., Moore, B., Governato, F., Lake, G., Quinn, T., & Stadel, J., 2000, ApJ, 544, 616

Gingold, R.A., & Monaghan, J.J., 1977, MNRAS, 181, 375

Giovanelli, R., Haynes, M. P., Herter, T., Vogt, N. P., da Costa, L. N., Freudling, W., Salzer, J. J., & Wegner, G., 1997, AJ, 113, 53

Governato, F., Mayer, L., Wadsley, J., Gardner, J., Willman, Beth, Hayashi, E., Quinn, T., Stadel, J., Lake, G., 2004, ApJ, 607, 688

Governato, F., Willman, B., Mayer, L., Brooks, A., Stinson, G., Valenzuela, O., Wadsley, J., Quinn, T., 2006, MNRAS submitted

Hernquist, L., 1993, ApJS, 86, 389

Heald, G.H., Rand, R.J., Benjamin,R.A., Bershady, M.A., 2005, astro-ph/0508559

Hernquist, L., & Katz, N., 1989, ApJS, 70, 419

Huang, S., & Carlberg, R. G., 1997, ApJ, 480, 503

Hut, P. & Makino, J. 1999, Science, 283, 501

Jiang, I.-G., & Binney, J., 1999, MNRAS, 303, L7

Katz, N., 1992, ApJ, 391, 502

Katz, N., Weinberg, D. H., & Hernquist, L. 1996, ApJS, 105, 19

Kaufmann, T., Mayer, L., Wadsley, J., Stadel, J., Moore, B., 2006a, MNRAS, 370, 1612

Kaufmann, T., Mayer, L., Wadsley, J., Stadel, J., Moore, B., 2006b, astro-ph/0601115

Kazantzidis, S., Magorrian, J., & Moore, B., 2004, ApJ, 601, 37

Kazantzidis, S., Kravtsov, A. V., Zentner, A. R., Allgood, B., Nagai, D., & Moore, B., 2004b, ApJL, 611, L73

Kitsionas, S., & Whitworth, A. P., 2002, MNRAS, 330, 129

Kitsionas, S., 2000, Ph.D. Thesis, U. Wales

Koch, P., 2003, PhD Thesis, U. Zürich

Kereš, D., Katz, N., Weinberg, D. H., & Davé, R. 2005, MNRAS, 363, 2

Kuijken, K., & Dubinski, J. 1994, MNRAS, 269, 13

Levine, E.S., Blitz, L., Heiles, C., 2006, ApJ accepted, astro-ph/0601697

Lucy, L., 1977, ApJ, 82, 1013

Lynden-Bell, D., 1962, MNRAS, 124, 1

Maller, A. H., Bullock, J. S., 2004, MNRAS, 355, 694

Marri, S., & White, S. D. M., 2003, MNRAS, 345, 561

Mastropietro, C., Moore, B., Mayer, L., Wadsley, J., & Stadel, J., 2005, MNRAS, 363, 509

Mayer, L., 2004, Proceedings of Science, Conference "Baryons in Dark Matter Haloes", paper #037

Mayer L., Wadsley J., 2004, MNRAS, 347, 277

Mayer L., Mastropietro C., Wadsley J., Stadel J., Moore B., astro-ph/0504277

McCarthy, I. G., Babul, A., Katz, N., & Balogh, M. L. 2003, ApJL, 587, L75

McKee, C. F., & Ostriker, J. P., 1977, ApJ, 218, 148

Mo, H. J., & Miralda-Escude, J., 1996, ApJ, 469, 589

Mo, H., Mao S., White S., 1998, MNRAS, 295, 319

Monaghan, J. J., 1992, ARAA, 30, 543

Moore, B., & Davis, M., 1994, MNRAS, 270, 209

Moore, B., Kazantzidis, S., Diemand, J., & Stadel, J. 2004, MNRAS, 354, 522

Murai, T., & Fujimoto, M., 1980, PASJ, 32, 581

Murray, S. D., White, S. D. M., Blondin, J. M., Lin, D. N. C., 1993, ApJ, 407, 588

Navarro, J. F., & Benz, W., 1991, ApJ, 380, 320

Navarro, J. F., Frenk, C. S., & White, S. D. M. 1995, MNRAS, 275, 56

Navarro, J. F., Frenk, C. S., & White, S. D. M., 1996, ApJ, 462, 563

Navarro, J. F., & Steinmetz, M. 1997, ApJ, 478, 13

Navarro, J. F., Steinmetz, M. 2000, ApJ, 538, 477

Okamoto, T., Jenkins, A., Eke, V. R., Quilis, V., & Frenk, C. S. 2003, MNRAS, 345, 429

Osipkov, L. P., 1979, Soviet Astron. Lett., 5, 42

Peacock, J.A., 1999, Cosmological Physics, Cambridge University Press

Pearce, F.R., Jenkins, A., Frenk, C.S., White, S.D.M., Thomas, P.A., Couchman, H.M.P., Peacock, J.A., Efstathiou, G., 2001, MNRAS, 326, 649

Peebles, P. J. E., 1969, ApJ, 155, 393

Plummer, H. C., 1911, MNRAS, 71, 460

Power, C., Navarro, J. F., Jenkins, A., Frenk, C. S., White, S. D. M., Springel, V., Stadel, J., & Quinn, T., 2003, MNRAS, 338, 14

Putman, M. E., et al., 2002, AJ, 123, 873

Putman, M. E., Staveley-Smith, L., Freeman, K. C., Gibson, B. K., & Barnes, D. G. 2003, ApJ, 586, 170

Putman, M. E., 2006, ApJ accepted, astro-ph/0603650

Quinn, T., & Binney, J., 1992, MNRAS, 255, 729

Regan, M. W., & Vogel, S. N., 1994, ApJ, 434, 536

Revaz, Y., & Pfenniger, D., 2004, A&A, 425, 67

Richter, P., 2006, astro-ph/0602343

Robertson, B., Yoshida, N., Springel, V., & Hernquist, L. 2004, ApJ, 606, 32

Roediger, E., Brueggen, M., Hoeft, M., 2006, astro-ph/0603565

Romeo, A. B., 1994, A&A, 286, 799

Saha, K., Jog, C.J., 2005, astro-ph/0510804

Sanchez-Salcedo, F. J., 2006, MNRAS, 365, 555

Sancisi, R. 1976, A&A, 53,159

Sembach, K.R. et al., 2003, ApJS, 146, 165

Shang, Z., et al., 1998, ApJL, 504, L23

Sommer-Larsen, J., Gelato, S., & Vedel, H., 1999, ApJ, 519, 501

Sommer-Larsen, J., Götz, M., & Portinari, L., 2003, ApJ, 596, 47

Sommer-Larsen, J., 2006, ApJL submitted

Sparke, L. S., & Sellwood, J. A., 1987, MNRAS, 225, 653

Springel, V., Yoshida, N., White, S.D.M. 2001, New A., 6, 79

Springel, V. & Hernquist, L. 2002, MNRAS, 333, 649

Springel, V., 1999, PhD Thesis, Ludwig-Maximilians-Universität München

Stadel J., 2001, PhD Thesis, U. Washington

Steinmetz, M. 1996, MNRAS, 278, 1005

Steinmetz, M., & White, S. D. M. 1997, MNRAS, 288, 545

Thacker, R. J., & Couchman, H. M. P., 2000, ApJ, 545, 728

Thacker, R. J., Tittley, E. R., Pearce, F. R., Couchman, H. M. P., & Thomas, P. A., 2000, MNRAS, 319, 619

Toomre, A. 1964, ApJ, 139, 1217

Tonini, C., Lapi, A., Shankar, F., & Salucci, P., 2006, ApJL, 638, L13

Van den Bosch F., 2001, MNRAS, 327, 1334

Wadsley J., Stadel J., Quinn T., 2004, NewA, 9, 137

Weinberg, M.D., Blitz, L., 2006, astro-ph/0601694

White, S. D. M., & Rees, M. J., 1978, MNRAS, 183, 341

White, S. D. M., 1984, ApJ, 286, 38

White, S. D. M., & Frenk, C. S., 1991, ApJ, 379, 52

White, S. D. M., 1994, astro-ph/9410043

Acknowledgments

Many people have supported me during this work. First of all I want to thank Ben Moore for giving me the opportunity to write this thesis, for his exhaustless amount of ideas, his continuous support and for permitting me to get in touch with a lot of interesting people. In the same breath my thank goes to Lucio Mayer, with whom I worked most of the time. I benefited a lot from his guidance during my studies, his encouragement and support. But also the numerous discussion about "politics" in the scientific world were most helpful. Of course this work would not have been possible without all the programs and ideas Joachim Stadel has contributed. I also enjoyed very much working together and exchanging ideas with Jürg Diemand, Chiara Mastropietro, Stelios Kazantzidis, Andrea Macciò, Steen Hansen, Victor Debattista, Aaron Dutton, Frank van den Bosch, Norbert Straumann, Philippe Jetzer, Doug Potter, Oscar Agertz, Simone Weinmann, Marcel Zemp and last but not least Tobias Goerdt. Other people have also contributed to some of the projects presented in this work, their input is acknowledged at the end of the corresponding chapters.

I had various enjoyable moments with the people at the Institute for Theoretical Physics: Skiing days, Fondue & bowling events, Doppelkopf sessions (Andreas Kaiser and Christoph Meier should be mentioned) and the legendary Helsinki nights, thanks a lot. A special thanks goes to Tobi Huber, Uma and Daniel Maître for being my 36K36-mates during long and sometimes dark hours struggling amongst others with LMC.

I would like to thank Daniel Wyler and Diethard Klatte from the University of Zürich for financial and other support during the completion of this thesis.

Dieter Basler sparked my interest in cosmology already years ago and Stefan Jörissen showed continuous interest in my work and encouraged me, thanks a lot.

Finally, I am very grateful to my family and all my friends, in particular my parents Dorette and Ernst, for their patience, interest in my work and unconditional support during my entire studies.

CURRICULUM VITAE

Personal data

Name : KAUFMANN
First name : Tobias
Date of birth : March 11, 1975
Place of origin: Gränichen AG
Nationality : Swiss

Education

10/2002-05/2006: PhD in Theoretical Physics, University of Zürich, Switzerland
PhD thesis: SPH/N-body Simulations of Galaxy Formation
Thesis supervisor: Professor Ben Moore

04/1999-01/2003 Master of Advanced Studies in Secondary and Higher Education, University of Zürich, Switzerland

10/1995-02/2002: Diploma in Theoretical Physics, University of Zürich, Switzerland
Diploma thesis: On a Crucial Sign Difference in Brane World Models
Thesis supervisor: Professor Norbert Straumann

08/1991-06/1995: Matura Typus C, Alte Kantonsschule Aarau, Switzerland

Teaching experience

10/2004-10/2005: Teaching assistant for analysis at the Institute for Theoretical Physics at the University of Zürich for mathematics and physics majors

10/2002-09/2004: Teaching assistant for analysis and linear algebra at the Institute for Operations Research at the University of Zürich for undergraduate students: coordination and conception of exercises and examinations.

1996-2000: several positions as a high-school teacher

Languages

German: Native language

English: fluent

French: good

RESEARCH STATUS

Publications:

1.) Kaufmann, T., Mayer, L., Wadsley, J., Stadel, J., & Moore, B.
Cooling flows within galactic haloes:
the kinematics and properties of infalling multi-phase gas
MNRAS, 370 (2006), 1612, astro-ph/0507296

2.) Kaufmann, T., Mayer, L., Wadsley, J., Stadel, J., & Moore, B.
Angular momentum transport and disk morphology
in SPH simulations of galaxy formation
submitted to MNRAS, astro-ph/0601115

In preparation:

1.) Kaufmann, T., Debattista, V., Stadel, J., Wadsley, J., Potter, D., & Moore, B.
Tilting and warping during galaxy formation
to be submitted to MNRAS

2.) Kaufmann, T., Mastropietro, C., Stadel, J., Wadsley, J., Potter, D., & Moore, B.
Constraining the spin of the hot halo of the Milky Way
to be submitted to MNRAS

Conference proceedings:

1.) Kaufmann, T., Mayer, L., Wadsley, J., Stadel, J., & Moore, B.
High resolution SPH simulations of disk formation in CDM haloes;
resolution tests
in: *Proceedings of the Conference "Baryons in Dark Matter Haloes"*
Novigrad, Croatia, 2004, eds. R.-J. Dettmar, U. Klein & P. Salucci